HYDROELASTIC RESPONSE OF MARINE STRUCTURES TO IMPACT-INDUCED VIBRATIONS

by

Nabanita Datta

A dissertation submitted in partial fulfillment
of the requirements for the degree of
Doctor of Philosophy
(Naval Architecture and Marine Engineering)
in The University of Michigan
2010

Doctoral Committee:

Professor Armin W. Troesch, Chair
Professor Robert F. Beck
Professor Nickolas Vlahopoulos
Associate Professor Bogdan Epureanu

To my parents, Pita and Mata

ACKNOWLEDGEMENTS

I would take this opportunity to extend my deepest gratitude to my professors, friends and family for their constant support.

My greatest strength in making this dissertation a reality has been my doctoral adviser, Prof. Armin W. Troesch. I am grateful to him for his help in laying the foundation of my future research. I thank the esteemed members of my dissertation committee, Prof. Robert F. Beck, Prof. Nickolas Vlahopoulos, and Assoc. Prof. Bogdan Epureanu.

I am grateful to members of the faculty of the Department of Naval Architecture and Marine Engineering, University of Michigan, namely, Prof. Michael M. Bernitsas, Assoc. Prof. Dale G. Karr, and Assoc. Prof. Yin Lu Young. I am also grateful to research scientists Dr. Kevin Maki and Dr. Okey Nwogu, and post-doctoral researchers Laura Alford and Ajith Kumar Raghavan.

I would like to thank my friends Christopher Hart, Weiwei Yu, Mark Neeland, Shrutivandana Sharma, Saurabh Gupta, Yogita Pai, Sonal Joshi, Jivesh Govil, and Shashi Bhushan Singh.

In my homeland *Bharatvarsha* (India), I would like to thank the faculty members of *Mahasagar Abhiyantriki Evam Nausthapatya Vibhag* (Department of Ocean Engineering and Naval Architecture), *Bharatiya Praudyogiki Samsthan* (Indian Institute of Technology), Kharagpur, especially, Prof.S.C.Misra, Prof.D.Sen, Prof.O.P.Sha, Prof.N.R.Mandal and Assoc. Prof.T.Sahoo.

I thank my parents, my sister and my brother-in-law for their constant love and support in all my endeavors in life.

This work was partially supported by the Office of Naval Research (ONR) grant titled *Design Tools for the Sea-Base connector Transformable Craft (T-Craft) Prototype Demonstrator*, Award Number N00014-07-1-0856, under the direction of Kelly Cooper, ONR grant Award Number N00014-06-1-0474 under the administration of Dr. Patrick Purtell, and the Department of Naval Architecture and Marine Engineering, University of Michigan.

PREFACE

Hydroelastic behaviorial analysis of marine structures (ocean-going and offshore) has been becoming increasingly important as an area of research in naval architecture. As marine vessels become larger and their structure becomes lighter, the elastic behavior gains prominence, leading to adverse effects like hull bottom damage, fatigue stresses due to prolonged hull whipping, and local failures. The larger the structure, the more is its flexural behavior. Offshore oil exploration utilizes VLCC (Very Large Crude Carriers) and ULCC (Ultra Large Crude Carriers) for transportation and storage. Such vessels require a hydroelastically sound design. As the increasing world population leads to the scarcity of inhabitable land, (flexible) floating cities and airports are not far from becoming a reality. Arctic and Antarctic exploration provides another area of hydroelastic application, where ice-breaking (a few hundred km^2 in area) is a major challenge.

The estimation of the global flexural strength notwithstanding, isolated hydroelastic analysis is necessary to incorporate local strength in regions of the craft; e.g. the bow, wetdeck, stern, and bow flare. Slamming is a common phenomenon in planing crafts : sudden decreases in the dynamic lift of the hull causes the craft to impact against the wall of water below its bow. Slamming damage may be local structural failures or fatigue due to the weakly damped, persistent global whipping induced by the impact. Slamming is also a common phenomenon in the sea environment, where, depending on the frequency of encounter of the vessel with the wave field, the forefoot emerges once every few wave encounters, followed by an inevitable slam. The relative bow motion, which is a superposition of the heave, pitch and the wave (in magnitude and phase), indicates the probability of slam for a given sea state.

CONTENTS

LIST OF FIGURES

FIGURE

Chapter 1

Chapter 2

Chapter 3

Chapter 4

Chapter 5

Appendix 2

LIST OF TABLES

TABLE

Chapter 2

Chapter 3

Chapter 4

Chapter 5

LIST OF APPENDICES

APPENDIX

NOMENCLATURE

Independent variables

x	Coordinate along X.	y	Coordinate along Y.	z	Coordinate along Z.
t	Time-coordinate.	x'	Non-D length $\frac{x}{L}$.	y'	Non-D width $\frac{y}{B}$.
t'	Non-D time $\omega_1 t$.	$\mathbf{n}$	Unit normal vector.		

Geometric Properties

L	Length.	B	Width.	h	Thickness.
α	Aspect Ratio.	m	Mass per unit area.	g	Gravity.

Material Properties

E	Modulus of elasticity.	ν	Poisson's Ratio.	ρ_s	Density of steel.
ρ_w	Density of water.	D	Plate stiffness.	ζ	Damping Ratio.

Modal Analysis

Φ_j	j^{th} Plate modeshape.	$\phi_j(x)$	j^{th} Beam modeshape.
$q_j(t)$	j^{th} Generalized coordinates.	M	Generalized Mass.
K	Generalized Stiffness.	C	Generalized Damping.
C_{cr}	Modal Critical Damping.	gf	Generalized Forcing.
j	Number of modes along X.	l	Number of modes along Y.
k	Number of plate modes.	$G(x,y)$	Product of beam modes.
$F(t)$	Time-dependent function.	A_{jl}^k	Amp. of G_{jl} of the k^{th} mode.
H_{jl}	Amp. of G_{jl} in Static analysis.	A1	Beam modeshape constants.

Results

$Z1_{st}$	Max. possible z_{st}.	$Z2_{st}$	Max. z_{st} at each t.
$Z3_{st}$	Max. z_{st} at each x.	DLF	Dynamic Loading Factor.
RMC	Relative Modal Contribution.		

Transient Forcing

V	Vertical impact velocity.	c	Speed of the moving load.
β	Deadrise angle.	$d(t)$	Impact jet head.
$\dot{d}(t)$	Impact jet head velocity.	X	Stretching variable.
ξ	Stretching parameter.	T_{sp}	Splash time.
τ	Non-D Splash time.	P_{impact}	Impact pressure.
$P_{radiation}$	Radiation pressure.		

Beam Vibration

m(x)	Mass per unit length.	F(x,t)	Transient force.
I	Second moment of inertia.	$\omega_{j,dry}$	j^{th} Frequency of beam.
T_j	j^{th} period of the beam.	γ_j	j^{th} wave number of beam.
Z(x,t)	Total dynamic deflection.	$Z_{st}(x,t)$	Total static deflection.

Plate Vibration

Z(x,y,t)	Dynamic deflection.	τ_{CC}	τ normalized by γ_1 of CC beam.
$Z_{st}(x,y,t)$	Static deflection.	τ_{SS}	τ normalized by γ_1 of SS beam.

Wet Vibration

$\Psi(x,y,t)$	Velocity potential.	$\omega_{wet,j}$	j^{th} Wet natural frequency.
$\eta(x,t)$	Free surface profile.	$\phi_j^*(x,y,z)$	j^{th} Velocity potential per $\dot{q}_j(t)$.
∇	Fluid volume.	S	Surface of the fluid volume.
P	Field point.	Q	Source point.
G_{PQ}	3-D Green's function.	ϵ	Infinitisimal area around Q.
σ	Source strength density.	σ_k	k^{th} source strength density.
ξ	x-coordinate of Q.	η	y-coordinate of Q.
ς	z-coordinate of Q.	r	Distance between P and Q.

ABSTRACT

HYDROELASTIC RESPONSE OF MARINE STRUCTURES TO IMPACT-INDUCED VIBRATIONS

by

Nabanita Datta

Chair : Armin W. Troesch

This research deals with the numerical analysis of the hydroelastic behavior of marine vessels under hydrodynamic impact loads, which causes potentially detrimental local flexural vibrations in the vessel. The objective is to provide the *dynamic response spectra* for transient water-structure dynamics subject to typical impact loads and time scales, using one-way coupling between the fluid and the structure. The hydrodynamic pressure is assumed to be applied on the rigid plate, and then the plate is modelled to respond elastically. The structural vibrations are assumed not to influence the hydrodynamic pressure field.

The changing wetted surface is the prime complexity of the problem. The sweeping load sets the plate into small amplitude vibrations, exciting all its natural frequencies (fundamental and overtones). The *time-scales* of the problem are : (a) the duration of the forcing when sweeping across the plate, and (b) the natural period of the structure. Assuming small deflections of the structure, normal mode summation is used to calculate the vibratory response. The total deflection is assumed to be a series summation of the modal deflections. When the amplitude of the vibrations is small, the dynamic stresses are directly proportional to the flexural displacement.

Two configurations of the moving load, i.e. (i) uniform stretching load and (ii) impact load, are applied. The coupled system of modal governing differential equation is non-dimensionalized in space and time, and the Dynamic Loading Factor (DLF) of the loading is numerically evaluated by the fourth-order Runge-Kutta method. The corresponding static deflections are calculated by Galerkin's method. The ratio of the maximum dynamic deflection to the maximum static deflection is the DLF. This analysis provides recommendations to the structural designer, who typically relies on static analysis. The modal participation spectra relative to the dominant fundamental mode for various impact speeds is used to establish modal truncation guidelines.

The variation of the response with respect to space and time, and with respect to various parameters like the aspect ratio, damping ratio, boundary conditions, and deadrise angles has been studied. The change in natural frequencies of the structure due to these parameters, and immersion, has also been evaluated.

CHAPTER I

INTRODUCTION

1.1 Problem Definition.

The subject of flexible fluid-structure interaction has been gaining prominence in academic research and practical applications in the last few decades. The prediction of the magnitude and distribution of hydrodynamic impact pressures is a useful criterion for the structural design of high-speed vessels. The study of global and local dynamic elastic behavior of marine vessels and structures forms the basis of marine hydroelasticity. Non-conventional high-speed crafts built of lighter materials like aluminum, GRP, FRP, non-metallic composites, etc. require hydroelastic analysis as an important component of the basic design spiral. The estimation of the global flexural strength notwithstanding, isolated hydroelastic analysis is necessary to incorporate local strength in regions like the bow, wetdeck, stern, and bow flare.

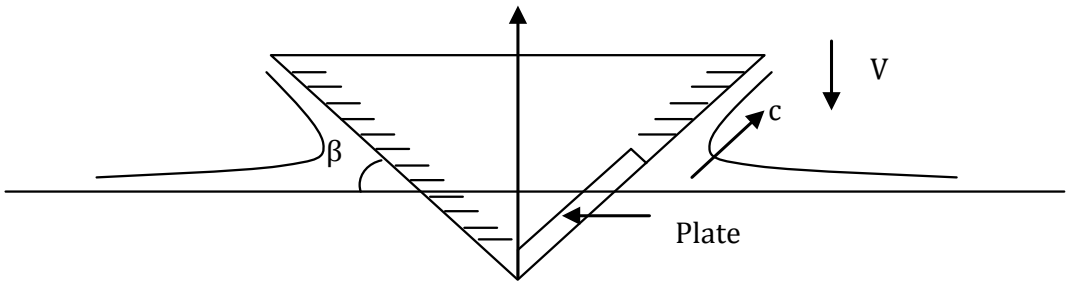

Figure 1.1: Two-dimensional slamming model.

Slamming or impact is a common phenomenon, where in severe seas, the vessel hull emerges once every few wave encounters, followed by a probable slam (Fig.1.1). The detrimental effects of impact-induced vibrations are several; namely, transient local high-frequency vibrations, global whipping, fatigue, and permanent plastic deformations of the bow and bottom platings due to the very high localized slamming pressures.

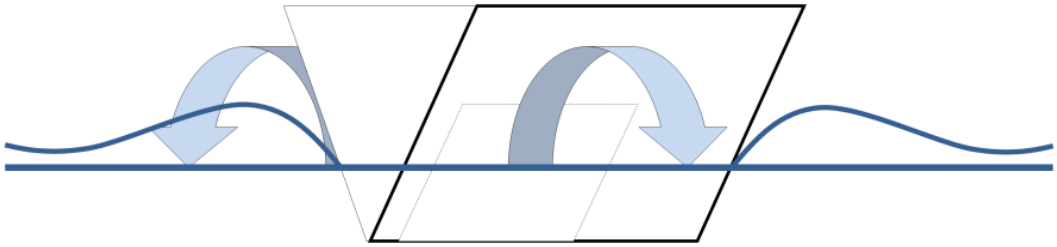

Figure 1.2: Three-dimensional wetting.

Slam-induced impact pressures have been investigated widely, first pioneered by Von-Karman in 1929, improved upon by Wagner in 1932. Accurate estimation of the peak impact pressure for various slam velocities and deadrise angles resulted from decades of intensive research, both analytical and experimental. Relatively less investigated is the area of *dynamic elastic response* of the structure subjected to such loads. For some applications, the dynamic system can be modelled as a distributed force sweeping across the length of the plate at a certain velocity, and the plate being set into vibratory motion (Fig.1.2), damped by material friction or radiation damping. The surrounding fluid is also set into motion, thereby increasing the effective system inertia. The restoring forces are the flexural rigidity of the structure and the changes in buoyancy (especially in global-scale hull vibrations). The interaction of inertial, elastic and hydrodynamic forces generates the hydroelastic response.

This response involves the wet vibrations of the bow, keel, and the wetdeck. The natural frequency of vibration of elastic structures is considerably reduced in water as compared to in air. The structure is subjected to intense moving hydrodynamic pressures (Fig.1.3), which sets it into high frequency, weakly damped, submerged vibrations. Water inertia offsets the stiffness of the plate, possibly predisposing it to greater dynamic response. Thus, vibration analysis becomes mandatory for efficient structural design of such susceptible marine structures under vulnerable environmental conditions.

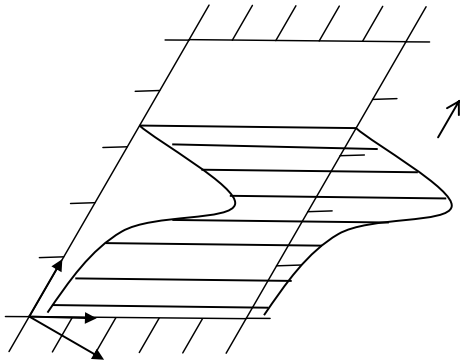

Figure 1.3: Three-dimensional Impact Pressure.

1.1.1 Motivation

1. *Structural design: plate scantlings.*

The study of the hydroelastic response of marine structures, to hydrodynamic impact loads, establishes several critical structural design criteria.

2. *Frequency domain analysis.*

The response of the structure to transient loading involves all the natural frequencies of vibration. The study of the deflection in the frequency domain leads to useful insights into resonance, susceptible frequencies and modeshapes, and how the structure behaves as a band-pass filter to the hydrodynamic load. (Ships are low-pass filters to the sea wave loads).

3. *Response generalization with respect to all the parameters.*

Structural parameters like deadrise angle, plate boundary conditions, aspect ratio, and damping ratio, all influence the time-scales of the phenomenon. To assist in the interpretation of the results, the response can be generalized with respect to all the parameters to generate a self-similar response characteristic for a range of impact speeds and material properties.

1.1.2 Research Questions

1. *What is maximum dynamic response*?

The maximum stress is proportional to the maximum strain within the limits of small deflections and pure bending. The *magnitude* of the maximum stress would dictate the plate scantlings of the hull. The structural designer typically conducts the static analysis of the plate under an equivalent *area load*. The dynamic overshoot of the stress magnitude needs to be taken into account as a compulsory *safety factor* for design.

2. *What are the spatial and temporal distributions of the response*?

Given the framing and the geometry of the hull, the *location* of the maximum response will depend on the boundary conditions and the aspect ratio of the plate. The *instant* of the maximum load and the *duration* of the high stresses depend on impact speeds, natural frequencies of the plate, and structural damping.

3. *What are the time scales of the phenomenon*?

An impact load excites all the natural frequencies of the structure to different extents. The *impact load's* duration, configuration, and orientation influences the degree of participation of each frequency. *Added mass*, and to a lesser extent, *damping* decrease the frequency of vibration. Different plate boundary conditions and aspect ratios also change the natural frequency. A combination of all these parameters define whether a plate is *soft* or *stiff* relative to impact loading.

4. *How does the response vary with deadrise angle*?

The deadrise angle is a very important design parameter of a high-speed vessel. It influences (a) the maximum impact pressure, (b) the wetting speed, and (c) the instant in time when the maximum deflection occurs.

5. *How does the response vary with plate boundary conditions and aspect ratios*?

These parameters collectively *soften* or *stiffen* the plate, thereby compressing the composite time-scale to the dynamic zone or a quasi-static zone of the response.

6. *Which are the susceptible plate natural frequencies*?

If the time-scale of the impact coincided with one of the natural frequencies of the plate, it leads to possible resonant behavior and, subsequently, fatigue.

7. *Which are the susceptible plate modeshapes*?

As an extension of the above, the modeshapes associated with resonant frequencies are susceptible to fatigue. Also, the modeshapes which align themselves with the spatial configuration of the moving load are excited the most, and hence, the most vulnerable.

8. *What is the effect of immersion on the dynamic response*?

Wetting reduces the natural frequency of the structure, stretching the time-scale.

1.2 Literature Review.

This work investigates a wide range of issues related to the vibration of flexible marine structures in water. The literature review generally examines *hydroelasticity*, i.e. the vibration of elastic structures in water. The hydrodynamic force of the fluid causes the structural vibrations. The nature of the force can be of different kinds, e.g. regular wave loads, irregular sea loads, or random impact loads. The choice of the force here is restricted to hydrodynamic impact loads. Thus the literature associated with ship *slamming* and *impact* is investigated. **The primary aim of this dissertation is the assessment of the response of the structure to such loads**. Since the impact is a transient load, it was necessary to study the effect of *moving loads* on structures. First, the structure is idealistically modelled as a *beam*, and the response of beams to the moving loads is studied. Structural *damping* is also incorporated. The modelling complexity is increased where the structure is made more realistic, being modelled as a *plate* (Fig.1.4). The free vibration of plates in air is thoroughly investigated, followed by forced vibration of the same. After the dry analysis, the plate is assumed to vibrate in water, taking into account *fluid-structure interaction* effects. Finally, vari-

ous *aspect ratios* have been used to replicate the actual bottom plates of marine vessels.

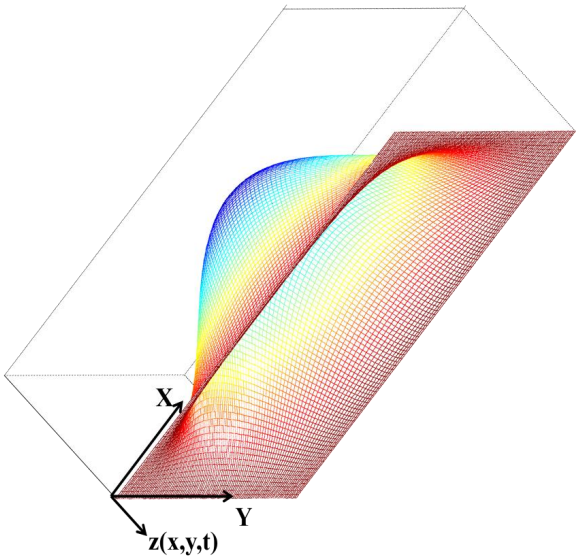

Figure 1.4: Fundamental CCCC plate modeshape.

1.2.1 Hydroelasticity.

All kinds of sea-going vessels and offshore structures suffer wave-induced or impact-induced vibrations to greater or lesser extents. The study of global hydroelasticity of marine structures has been going on for a past few decades.

Pioneering work on hydroelasicity has been done by Bishop and Price [1], beginning with the modal dry and wet analyses of the elastic responses of vessels in rough seaways due to hydrostatic and wave loads, followed by local transient impulsive loading anlaysis in regular and irregular seas. Xia et al [2] studied the global hydroelastic response of a containership to impact loading in a seaway, using time-domain strip theory with modal analysis. They compared the numerical and experimental analyses. Kyoung et al [3] investigated the hydroelastic response of VLFS, coupling the Boundary Element Method (BEM) with the Finite Element Method(FEM). They included a complicated

sea bottom condition and free surface. Senjanovic et al [4] analyzed the vibrations of ship girders, using the 1D FEM method to model several modes of vertical and torsional vibrations. Senjanovic et al [5] further looked into frequency-domain global ship hydroelasticity of a flexible barge, subject to a JONSWAP spectrum. They used modal analysis for the structure, and BEM for the fluid with a free surface.

1.2.2 Slamming and Impact.

A subset of hydroelasticity is the study of *local* elastic response of marine structures, especially due to impact loads. The impulsive pressure moving across the structure sets it into high-frequency vibrations. To investigate it, it first becomes necessary to evaluate the pressure magnitude, duration, and configuration, as a function of space and time.

Cointe [6] studied the slamming pressure on a solid due to an impact with a fluid surface. He divided the fluid into the outer and inner domains, overlapping the respective pressure to generate a *closed-form pressure distribution* over the jet-head, thereby avoiding the singularity in pressure found in the Wagner model of impact pressure. Howison et al [7] extended Cointe's model by using three domains in the fluid, formulating the outer pressure and the stretching inner pressure. The peak pressure, the keel pressure and the distribution has been formulated for small deadrise angles, using the independent variables of jet head, jet head velocity and jet thickness.

Henke [8] studied the elastic response of hull platings to typical hydrodynamic impulse loadings, generating the dynamic stresses as a function of space and time. Faltinsen [9] used modal analysis to study the similar response of a stiffened rectangular plate, taking advantage of Wagner's model to evaluate the added mass associated with the vibration. **However, he used only the first two modeshapes, and predicted a 13%-15% dynamic overshoot above the static deflection of the structure.** Lu et al [10] used a coupled structural-hydroelastic equation to model the water entry onto

a structure during impact. Khabakhpasheva and Korobkin [11] used the simple Wagner model to study the elastic response of a beam, under both dry and wet conditions, comparing them with the static response. **They predicted a 50% overshoot above the static deflection, using a very idealized model of a beam.** Peseux et al [12] used the impact pressure model similar to Cointe, and compared it to experimental investigations. Korobkin et al [13] used FEM to couple the structure with the fluid, to calculate the hydroelastic response and the added masses for different discretizations. Stenius et al [14] modelled the impact pressure with FEA, and studied the issues related to the *numerical analysis*. Kim et al [15] extended the impact pressure analysis to a hull with hard chines. Constantinescu et al [16] furthered the impact pressure evaluation over deformable surfaces with free surface effects.

The background for the transient impact pressure model being established, this literature review now proceeds to the study of the response of structures to the moving load.

1.2.3 Moving Loads.

Thomson [17] studied the transient vibration of single Degree-of-Freedom (DOF) systems, generating the *response spectra* (Dynamic Load Factor vs. non-dimensional impulse duration) for shock excitations. The arbitrary forcing needs numerical time-integration to generate the response.

Law and Chan [18] studied the vibratory response of beams to moving point forces as a function of *time*. Lee [19] did a similar analysis for beams, but evaluated the deflection as a function of *space*. Yau et al [20] extended the above to *bridge* vibration, subject to moving vehicles. Savin [21] used repeated moving loads on beams with various boundary conditions, and studied the *dynamic amplification factors* (DAF) of the vibration. Dugush and Eisenberger [22] used non-uniform continuous beams, and numerically evaluated the mid-span deflections by modal analysis. Lu and Chan [23] identified the

moving force by Fourier transformations for the displacement and velocity. Pesterev et al [24] evaluated the global Dynamic Loading Factor (DLF) of simply-supported (SS) and clamped-clamped (CC) beams over a wide range of moving speeds. Yagiz and Sakman [25] modelled the bridge as a plate, with the vehicle as a smaller plate moving over it, and used normal mode expansion to establish the dynamic deflection of the mid-point as a function of time.

The *speed* at which the forcing moves across the structure is the single most important parameter dictating the normalized response. The natural frequency of vibration of the structure is the other parameter influencing the elastic deflections.

1.2.4 Beam Vibration.

To study the response to moving impact hydrodynamic loads, the simplest structure is first chosen, which is a beam. The pressure and the response are assumed to be 2-dimensional, which is an initial *idealization* to lay the foundation for this work.

Yamaki and Mori [26] studied the non-linear vibration of clamped beams in the frequency-domain, using modal analysis. Ward [27] numerically studied the dynamic response of simply-supported beams to uniform stretching loads, and compared them to experimental results. Pan and Hansen [28] studied the effect of boundary conditions on beam vibration, taking into account eight different boundary conditions. Howard [29] analytically formulated the modal (generalized masses) of beams and plates. Wang and Cheng [30] studied the free vibration of beams with modal analysis.

1.2.5 Structural Damping.

Every structure has inherent damping, which reduces the maximum vibratory deflection and the *dynamic amplification* at resonance condition allowing for smaller scantlings in the design of the structure. Thus damping needs to be incorporated into the analysis.

Wilson and Man [31,32] formulated modal damping of multi-degree-of-freedom systems by defining the critical damping as a function of modal mass and modal stiffness. Bulatovic[33] studied critical damping of such systems similarly. Mahmoodi et al [34] used a different damping model for continuous systems to analyze the non-linear modeshapes of beams.

1.2.6 Plate Vibration.

The idealized beam is next extended to the more realistic plate, exposed to an impact load, resulting in high-frequency vibrations and dynamic stresses. First, the free vibration of the plate is studied to establish the natural frequencies, followed by the forced vibration analysis.

Young [35] analyzed the free vibration of plates by the *Ritz method*, with various boundary conditions. Saha et al [37] studied the higher-order large-amplitude vibrations of plates for different boundary conditions. Wang et al [38] perfected the modeshape functions of plates with different boundary conditions. Saha et al [39] returned with the non-linear plate vibrations, generating the modeshape contours. Zhang et al [40] furthered the study to wet free vibration analysis, using *Energy FEA* to evaluate the plate bending and energies associated. Yeh et al [41] delved into the numerical aspects of free vibration analysis of plates. Korobkin and Khabakhpasheva [42] used *3-D compressible jet impact* to study the deflection of elastic panels as a function of space and time, inclusive of the added masses. Yu et al [43] studied the numerical convergence of the frequencies of square plates with various boundary conditions. Chen et al [44] generated the modeshapes of rectangular plates experimentally, comparing them with the results from FEA.

The above literature has studied the structural response when most of the structure is still dry, and the hydrodynamic load can be assumed to act on a *dry* plate, producing

the maximum response at an early stage of the transient loading. The fluid inertia surrounding the plate is hitherto ignored.

1.2.8 Fluid-Structure Interaction.

When the maximum vibratory response occurs later in the impact sequence, the *radiation pressure* of the water vibrating along with the plate cannot be ignored. Historically, the free wet vibration of the plate has been analyzed to evaluate reduction in the natural frequencies and the associated added masses. The boundary value problem with varying complexities is defined in the literature below.

Lamb [45] studied the vibration of elastic circular plates in contact with water, using an energy method. Chertock [46] studied the flexural response of submerged solid, modelling the added mass as a *proportional solid*. Meyerhoff [47] calculated the added masses of rectangular plates, using dipole distribution strength as an series expansion. He calculated the added masses associated with each modeshape, and studied their convergence with modal truncation. Joseph et al [49] studied the decrease in natural frequencies of plates in fluids, given various plate densities, fluid densities and composite orientations. Wu et al [50] numerically evaluated the modal exciting forces, added mass and damping of an elastic floating plate, including the free surface of the fluid. Modal analysis has been used to solve both the diffraction and the radiation problems.

Kwak [51] studied the decrease in natural frequencies of rectangular plates with water on one side (with and without free surface), with different boundary conditions and aspect ratios. Faltinsen [52] studied the detailed response of beams to slamming pressures, evaluating the *wet natural frequencies* and the *modal added masses*. Chang and Liu [53] calculated the wet natural frequencies of floating plates, using an energy method, while Cheung and Zhou [54] did the same for bottom plates, for different volumes of surrounding fluid on one side. Yadykin et al [55] calculated the added mass

of cantilever plates, formulating the *added mass coefficient*. Hashemi et al [56] analyzed the vibration of vertical rectangular Mindlin plates in contact with varying depths of water on one side.

This concludes the literature review to study the wet vibration of square plates, subject to transient impact hydrodynamic loads.

1.2.9 Aspect ratio.

As an additional parameter of the plate, the aspect ratio is also included in this work. It changes the natural frequency of the plate. This is of practical importance, given the *framing* of the hull, which can be longitudinal or transverse.

Liew et al [57] calculated the natural frequencies of rectangular plates with various boundary conditions and aspect ratios, using an energy method. Harik et al [58] did the same using the analytical strip method, followed by modal analysis. Sakata et al [59] continued with the calculation of higher-order frequencies of orthotropic plates. Low et al [60] compared the Rayleigh-Ritz frequencies to experimental results. Zhu et al [61] studied the vibration of stiffened rectangular plates subject to moving point loads. Huang et al [62] studied the influence of aspect ratio on the modeshapes of free vibration of plates.

1.3 Dissertation Overview.

Chapter 2 of this thesis first formulates the *transient hydrodynamic force*. A benchmark forcing configuration, namely the uniform stretching load is defined, followed by the more realistic impact force model at a given impact speed V and deadrise angle β. The *methodology* of the analysis is next presented, detailing the normal mode expansion method for both free and forced vibration. Numerical evaluation of the dynamic deflection and the corresponding static deflection of the plate leads to the **Dynamic**

Load Factor (DLF). Modal analysis demands the study of modal participation and truncation. Thus the relative modal contribution of each mode, relative to the fundamental mode is studied. The DLF and the **Relative Modal Contribution** (RMC) are sensitive to structural parameters like deadrise angle, plate boundary conditions, damping, and aspect ratio. The influence of such parameters is included.

In Chapter 3, the structure is first simplistically modelled as a *beam*, whose free vibration analysis generates the natural frequencies and modeshapes of the beam. (These modes also form the basis functions for the plate modes). The beam is then subjected to the two loading configurations, at four different damping ratios and five deadrise angles, to generate a family of DLF plots. The self-similar behavior of the DLF is highlighted for a large range of wetting times.

Expanding the analysis in Chapter 4 to a more realistic geometry, free vibration is studied to generate the natural frequencies and modeshapes for *rectangular plates*. The forced vibration response of the plate is evaluated over a range of impact speeds and material properties. Different plate boundary conditions and aspect ratios further modify the DLF, and the corresponding RMCs.

The dry vibration analysis represents one of the extreme cases of the fluid-structure interaction problem. The investigation is now extended to the other extreme, i.e. *wet vibration analysis* in Chapter 5. The boundary value problem (BVP) of a vibrating plate in contact with water on one side is formulated, and the modal analysis is done by taking advantage of the body boundary condition (BBC), to generate the vibratory response characteristics of the plate. The dry and the wet vibration results from the respective analyses have been compared for both uniform and impact loading. The decrease in the natural frequency of the plate is also measured.

Finally, the work is discussed and conclusions are drawn, leading to recommendations for into possible future research.

1.4 Dissertation Contribution.

The three-year work resulting in this thesis leads to several interesting insights into transient hydrodynamic impact-induced vibrations of thin plates.

1) The quasi-static and the dynamic *zones* of the vibratory response over a range of impact velocities and material properties have been clearly established for both Uniform and Impact loading configurations.

2) The accuracy of the *dry natural frequencies* of plates have been established for 5 significant figures, and that of the *wet natural frequencies* to 4 significant figures. This shows that this reduced-order modelling does not compromise with the accuracy of the frequencies, while being efficient. Also, the frequencies have been grouped into three specific categories, which are the three kinds of solutions of the Eigen value analysis of the free plate vibration problem.

3) The *time-scales* of the problem are inclusive of the influence of the structural parameters like deadrise angle, plate boundary conditions, aspect ratio and damping ratio. The change in the plate response due to changing aspect ratios have been shown for both longitudinal and transverse stiffening of the hull bottom/keel, comparing its response to beam responses for extreme aspect ratios.

4) The *sensitivity* of the DLF to the above parameters have been studied and consistently established. Non-dimensionalization of the time-scale (independent variable) with respect to the deadrise produces a narrow band of DLF plots, for a deadrise from 1 degree to 30 degrees. Damping reduces the peak DLF and smooths the DLF characteristic in the quasi-static zone of the response.

5) The first 7x7 = 49 *modeshapes* of a CCCC plate have been established and tabulated systematically. The *unique* frequencies form the main diagonal of the matrix table. The *repeated* frequencies are adjacent to the main diagonal, and the *non-repeated* frequencies are diagonally adjacent to them. The two sets of frequencies lie in alternate

sub-diagonals as we proceed either way away from the main diagonal.

6) The *wet vibration* analysis results have been compared to those of the dry vibration analysis, again illustrating the fact that non-dimensionalization of time-scales self-similarize the Dynamic Load Factor (DLF) over the range of wetting speeds and material properties. In dry vibration, the impact force is non-dimensionalized by the plate inertia, while for the wet vibration analysis, it is non-dimensionalized by the total system inertia (plate+water inertia).

7) The relative modal contribution of the principal coordinates have been studied to establish the *modal truncation guidelines*, which evaluate the dynamic deflection within the limits of engineering accuracy. The decrease in natural frequencies and the corresponding added mass of vibrating plates have been calculated for three different plate boundary conditions, a wide range of aspect ratios and higher-order modeshapes.

8) The *modal contribution* to the total vibration for each of the modeshapes have been studied for the two different loading configurations, leading to understanding why a particular mode would be excited and another will not. It highlights why the odd beam modeshape parallel to the direction of the forcing is the most sensitive, while the even modeshape perpendicular to the forcing is the least sensitive. It also includes the contribution from the inter-mode coupling due to the stiffness and the added mass.

9) A special study has been done to study the dynamic response of the beams/plates at *zero wetting time* (i.e. instantaneous wetting), for four damping ratios, four boundary conditions and several aspect ratios.

10) The DLF charts form the basis for dynamic analysis of marine structures, useful to structural designers who conduct the static analysis under an area load. Here, the static analysis has also been done for the plate under the exact loading configuration.

CHAPTER II

ANALYSIS METHODOLOGY

Having introduced the problem, we now proceed to formulate its details and describe the method of the analysis. The transient loading is qualitatively and quantitatively described, followed by the analysis of the free and forced vibration of the structure by the normal mode analysis. The efficient modal analysis consumes much less time than the more accurate FEA, without compromising on the efficacy of the results and their relevance to the structural designer of marine vessels.

2.1 Problem Formulation.

The wedge-shaped bow section of the vessel is partially modelled as a flexible rectangular isotropic plate, subject to hydrodynamic impact loads, undergoing pure bending, with the rest of the bow-section rigid (Fig.2.1). The constant vertical impact velocity of the vessel is V. The water is assumed to be initially calm, and the vessel has zero heel. The deadrise (apex) angle is β, with respect to the horizontal. The structure has no flexural deflection or vibratory velocity at time $t = 0$. Upon impact, the plate (Fig.2.2) is set into flexural vibration, with all the natural frequencies excited to different levels. If the fundamental modal response is assumed dominant as Faltinsen [8], it is sufficient and efficient to consider $'$pure bending$'$ (Kirchhoff's plate), ignoring shear deformation and rotary inertia (Mindlin's plate).

Assumptions for pure bending :

(a) Plane cross sections remain plain after deformation.

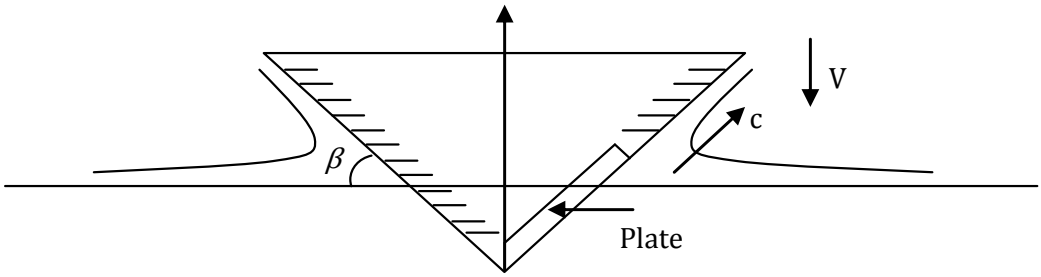

Figure 2.1: Two-dimensional model of impact hydrodynamics.

(b) Normals to the reference(neutral) axis remain normal.

(c) Changes in geometry of cross-section are neglected.

(d) Effects of shear deformation on displacements are neglected.

(e) Beam deformations and slopes are small.

This is a *dual* time-scale problem, with (**a**) the wetting time (time taken by the hydrodynamic load to sweep across the length of the plate) and (**b**) the fundamental natural frequency of the plate. Time-scales associated with (a) and (b) both influence the dynamic load factor (DLF). The corresponding static deflection, under exactly the same loading configuration, is calculated by Galerkin's method [58].

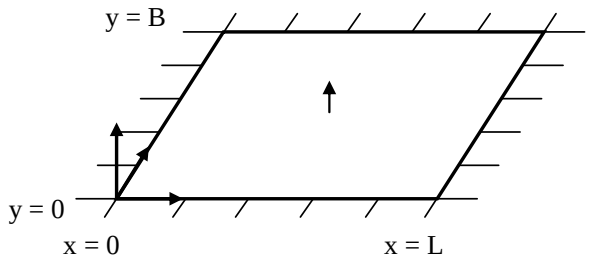

Figure 2.2: Kirchhoff's plate.

2.2 Transient Load Formulation

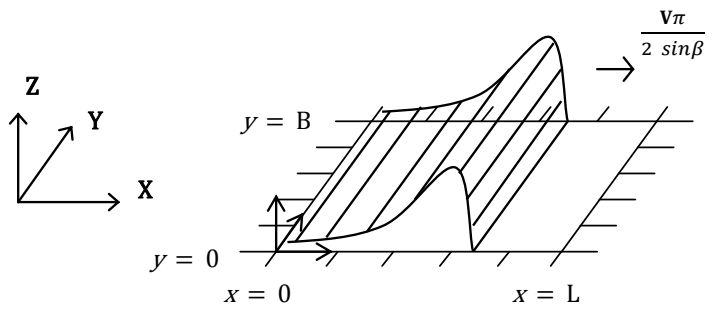

Figure 2.3: Transient Load.

The moving impact force is parallel to the X-axis of the rectangular Kirchhoff's plate (Fig.2.3) which has a length L and width B. The force does not vary along the Y-direction. The $x = 0$ and $x = \mathrm{L}$ boundaries of the plate typically correspond to to the longitudinal stiffeners; and the $y = 0$ and $y = \mathrm{B}$ boundaries typically correspond to the transverse stiffeners. For aspect ratio $\alpha > 1$, the hull is transversely framed, and for aspect ratio $\alpha < 1$, the hull is longitudinally framed.

2.2.1 Uniform Stretching Load

To compose a dynamic loading factor (DLF) typically associated with bridge engineering, the vibration of the plate subjected to a uniformly distributed stretching load moving across the dry plate (Fig.2.4) at a constant speed of V is analyzed by the modal expansion analysis.

There are *two* time-scales in this problem :

1) the time taken by the load to sweep across the plate T_{sp}, which is primarily dependent on the relative impact velocity V and deadrise angle β,

2) the fundamental frequency $\omega_{1,dry}$ of vibration of the plate, dependent on the geometrical and material properties of the plate, i.e. the boundary conditions, the damping ratio and the aspect ratio.

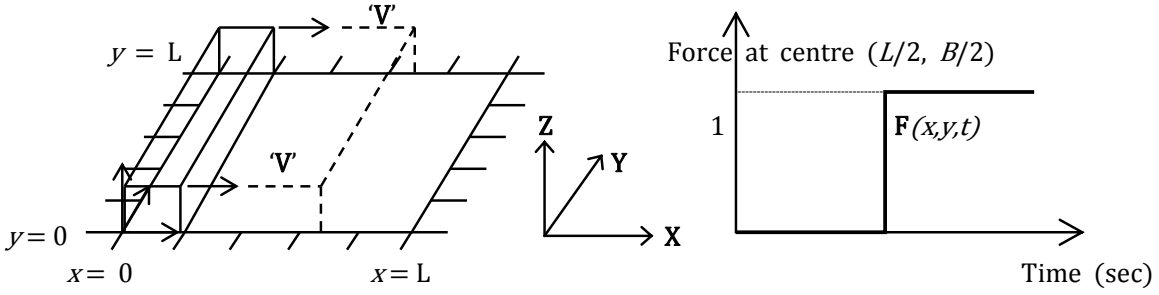

Figure 2.4: Uniform Stretching Load.

Defining the independent variables of the phenomenon, the *Splash time* is the time taken by the load to sweep across the length of the beam/plate. Non-dimensionalizing by the first natural period of the beam/plate, we define:

$$\text{Splash time } T_{sp} = \frac{L}{V} \quad \text{and} \quad \text{Non} - \text{D splash time} \quad \tau = T_{sp}\frac{\omega_{1,dry}}{2\pi}\sqrt{1-\zeta^2}. \tag{2.1}$$

This condenses the two time-scales into one. The composite time-scale (Eq.(2.1)) is the independent variable. The DLF is then plotted as a function of τ.

2.2.2 Impact Load

The response of the Kirchhoff's plate to the uniform stretching load helps establish the *benchmarks* of the modal analysis, namely (a) the time-scales, (b) the DLF, and (c) the RMC. Now we proceed to a more realistic model of the impact force distribution, defined by a moving jet head, stretching from the keel upwards. The maximum pressure

is a function of the vertical impact velocity V and the deadrise angle β.

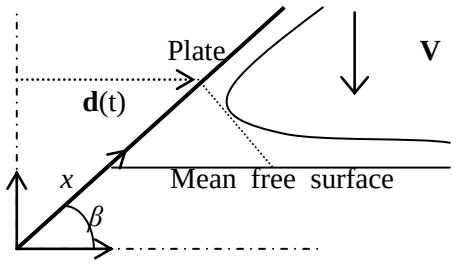

Figure 2.5: Impact Load.

The impact of the 2-D wedge section on a calm water surface at a downward velocity V (Fig.2.5) produces a rise up and a spray jet above the mean free surface. The impact pressure depends on V and the deadrise angle β. The maximum impact pressure occurs at the *spray root* $d(t)$, which is defined as the jet head translation at that instant. Pioneering research on impact pressure formulation by Wagner(1932) modelled a singularity in the pressure distribution at the spray root. Subsequent research by Cointe [6], Korobkin et al [13] and Faltinsen [9] indicates a superposition of asymptotic expansions of finite high pressures at the spray root and lower pressures away from it.

Peseux et al [12] define a closed form solution of the impact force as a function of space and time (Fig.2.6), using the following independent variables :

$$\text{Jet head } d(t) = \frac{Vt\pi}{2\tan(\beta)}, \quad \text{Jet head velocity } \dot{d}(t) = \frac{V\pi}{2\tan(\beta)},$$

$$\text{Jet Thickness } \delta(t) = \frac{\pi V^2 d(t)}{8\dot{d}(t)^2}.$$

The total non-dimensional impact pressure is :

$$P_{impact} = \frac{P_{outer} + P_{inner} - P_{common}}{\frac{1}{2}\rho_w V^2} \tag{2.2}$$

with components as : $P_{outer}(x,t) = \dfrac{V d(t)\dot{d}(t)}{\sqrt{[d^2(t) - x^2\cos^2(\beta)]}}$,

and $P_{common}(x,t) = \dfrac{V d(t)\dot{d}(t)}{\sqrt{2d(t)[d(t) - x\cos(\beta)]}}$.

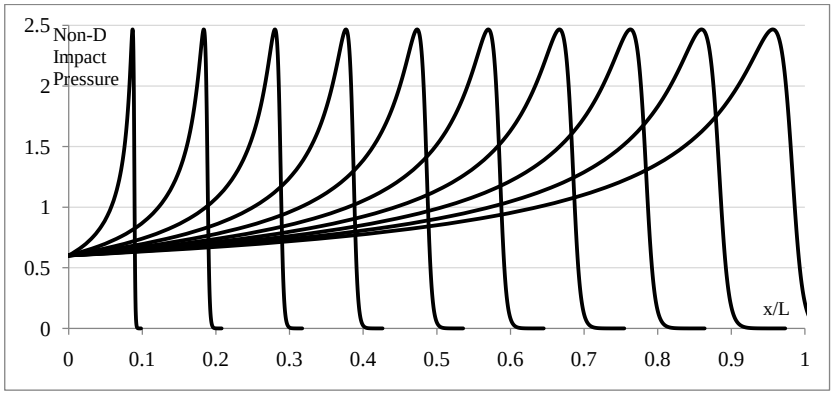

Figure 2.6: Sweeping Load at $\beta = 15$ degrees.

The inner pressure P_{inner} is expressed by Howison et al [7] as a *stretching transformation* with respect to the moving jet head $d(t)$. ξ is a parameter for this transformation, and X(t) is a dummy variable along the horizontal, scaled by the jet thickness and the deadrise angle β. The details have been given in Appendix 2.

Stretching the length : $x\cos(\beta) - d(t) = \tan^2(\beta).X$

$$\text{with } X = \frac{\delta(t)}{\pi}\left[\frac{6+4\xi}{1+\xi} - 4\sqrt{\frac{\xi-1}{\xi+1}} + log\left|\frac{\xi+1}{\xi-1}\right|\right]; \text{ with } \xi > 1, \xi < -1;$$

the inner pressure is defined as follows :

$$P_{inner}(x,t) = \rho_{water}\frac{\dot{d}(t)^2}{2}[1 - \{\xi - \sqrt{(\xi^2 - 1)}\}^2]$$

The superposition of the outer $P_{outer}(x,t)$ and inner pressures $P_{inner}(X(t),t)$ produces a closed form pressure distribution P_{impact} (Eq.(2.2)). The common pressure $P_{common}(x,t)$ needs to be subtracted since it has been double-counted in this superposition.

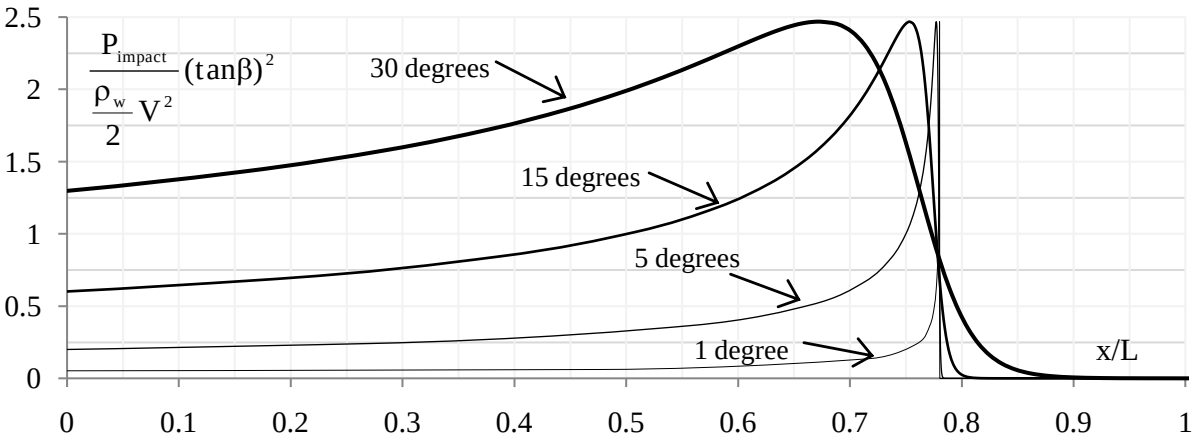

Figure 2.7: Impact Pressure Distribution.

The above impact pressure is used to study the response of beams and plates. The *keel pressure* is given as $P(0,t) = \rho_{water}V\dot{d}(t)$ and the *peak pressure* is given as

$$P_{peak} = \frac{\rho_{water}}{2}\dot{d}(t)^2;$$

which are the two constants of the stretching load. $P(0,t)$ is utilized in calculating the DLF at $\tau = 0$. The *stagnation pressure* of the vertical impact velocity is given as

$$P_{stagnation} = \frac{\rho_{water}V^2}{2}.$$

All the pressures (Fig.2.7) are non-dimensionalized by the stagnation pressure, and normalized by the deadrise angle, i.e. multiplying by $tan^2(\beta)$. Thus the maximum non-D pressure is 2.4674; and the maximum non-D keel pressure, at x = 0, is $\pi tan(\beta)$.

Here, the wetting time is defined and non-dimensionalized by the first natural period of the plate, as follows :

$$T_{sp} = \frac{2Lsin\beta}{V\pi}; \qquad \tau = \left[\frac{2Lsin\beta}{V\pi}\right] \frac{\omega_{1,dry}}{2\pi}\sqrt{1-\zeta^2}. \tag{2.3}$$

This is the independent variable (Eq.(2.3)) of the analysis, and the Dynamic Load Factor (DLF) is plotted against it, for the four different boundary conditions of the Kirchhoff's plate, and four different damping ratios.

2.3 Normal Mode Analysis.

The linear, second-order, homogeneous, governing differential equation for the free, damped vibration of the Kirchhoff's plate, ignoring gravity, is given by Eq.(2.4), where m is the mass per unit area of the uniformly thick plate, D is the flexural rigidity of the isotropic plate, and the damping $\mathbf{c}$ is implicitly calculated from the generalized damping. The generalized damping is proportional to the generalized mass and the generalized stiffness of the plate, all of which will be explained later. The dynamic deflection of the plate as a function of space as time is denoted as $Z(x, y, t)$.

$$m\frac{\partial Z^2(x,y,t)}{\partial t^2} + \mathbf{c}\frac{\partial Z(x,y,t)}{\partial t} + D\nabla^4 Z(x,y,t) = 0. \tag{2.4}$$

The deflection and the slope (curvature) are zero at the CC (SS) edges, given as :

$$Z(x,y,t) = 0, \frac{\partial Z(x,y,t)}{\partial x} = 0 \text{ at x = 0,L; } Z(x,y,t) = 0, \frac{\partial Z(x,y,t)}{\partial y} = 0 \text{ at y = 0,B.}$$

$$Z(x,y,t) = 0, \frac{\partial^2 Z(x,y,t)}{\partial x^2} = 0 \text{ at x = 0,L; } Z(x,y,t) = 0, \frac{\partial^2 Z(x,y,t)}{\partial y^2} = 0 \text{ at y = 0,B.}$$

The displacement and the velocity are zero at time t = 0, i.e.

$$Z(x, y, 0) = 0; \frac{\partial Z(x, y, 0)}{\partial t} = 0.$$

2.3.1 Free Vibration Analysis.

The dynamic deflection can be represented as a separation of the space and time variables as $Z(x, y, t) = G(x, y)F(t)$. Considering the mass and the stiffness to be uniformly distributed over the area, we get

$$mG(x, y)\frac{\partial^2 F}{\partial t^2} + \mathbf{c}G(x, y)\frac{\partial F}{\partial t} + D\nabla^4 G(x, y)F(t) = 0, \quad \text{which gives} \tag{2.5}$$

$$\frac{\ddot{F}(t)}{F(t)} = \frac{D}{m}\frac{\nabla^4 G(x, y)}{G(x, y)} = -\omega^2; \quad \text{where } -\omega^2 \text{ is the separation constant.}$$

Considering each of the equations of Eq.(2.5) separately,

$$\frac{\ddot{F}(t)}{F(t)} = -\omega^2 \quad \text{gives the principal coordinates, and}$$

$$\frac{D}{m}\frac{\nabla^4 G(x, y)}{G(x, y)} = -\omega^2 \quad \text{gives the plate modeshape.}$$

The equation for G(x, y) is a fourth order homogenous partial differential equation, generally not separable into two ordinary differential equations in x and y respectively. Resorting to the Rayleigh-Ritz method of approximate modeshape functions, the plate modeshape is assumed to be a weighted superposition of the 2-D beam modeshapes.

The total out-of-plane dynamic deflection $Z(x, y, t)$ is a function of space and time. Separating the variables into space and time, we assume $\Phi_k(x, y)$ as the k^{th} spatial shape function, and $q_k(t)$ as the temporal function of the k^{th} vibratory mode. The total out-of-plane dynamic deflection of the plate is approximately a linear superposition of

the modal deflections $Z_k(x, y, t)$, as given by Eq.(2.6),

$$Z(x, y, t) = \Sigma_{k=1}^{\infty} Z_k(x, y, t) = \Sigma_{k=1}^{\infty} \Phi_k(x, y) q_k(t), \tag{2.6}$$

with the 3-D plate modeshape (shape function) is defined as a series summation as follows :

$$\Phi_k(x, y) = \Sigma_{j=1}^{modex} \Sigma_{l=1}^{modey} A_{jl}^k \phi_j(x) \phi_l(y) = \Sigma_{j=1}^{modex} \Sigma_{l=1}^{modey} A_{jl}^k G_{jl}(x, y), \tag{2.7}$$

i.e. $G_{jl}(x, y) = \phi_j(x)\phi_l(y)$, *modex* is the number of modes considered in the x-direction, *modey* is the number of modes considered in the y-direction, and $\phi_j(x)$ and $\phi_l(y)$ are the respective 2-D beam modeshapes (forming an orthogonal set of functions). A_{jl}^k is the amplitude of each $G_{jl}(x, y)$ for the k^{th} natural frequency of vibration.

The plate modeshapes, given as a *weighted* spatial superposition of the product of the two beam modeshapes, do not form an orthogonal set of functions, i.e.

$$\int_0^L \int_0^B \Phi_k(x, y) \Phi_n(x, y) dx dy \neq 0,$$

for k not equal to n.

The Clamped-Clamped (CC) beam has zero deflection and zero slope at the ends. Thus the modeshape is given as

$\phi_j(x) = cos(\gamma_j x) - cosh(\gamma_j x) - \sigma_j sin(\gamma_j x) + \sigma_j sinh(\gamma_j x)$.

The Simply-Supported (SS) beam has zero deflection and zero bending moment at the ends. Thus the modeshape is given as $\phi_j(x) = sin(\gamma_j x)$.

Here, $\gamma_j^4 = m(x)\omega_j^2/EI(x)$ is the wave number of the beam vibration.

Substituting Eq.(2.7) in the fourth-order partial differential equation of G(x,y) and applying Galerkin's method (Shames and Dym 1991 [63]) A_{jl}^k is calculated as follows :

$$\Sigma_p \Sigma_r \int_L \int_B G_{pr} A_{jl}^k \left[\frac{d^4\phi_j}{dx^4}\phi_l + 2\frac{d^2\phi_j}{dx^2}\frac{d^2\phi_l}{dy^2} + \phi_j \frac{d^4\phi_l}{dy^4} - \omega^2 \frac{m}{D}\phi_j\phi_l \right] dx dy = 0. \tag{2.8}$$

The Eigen value analysis of Eq.(2.8) using Galerkin's method gives the frequencies (Eigen values) and modeshapes (Eigen vectors). Note that since the damping is assumed to be independent of space, the analysis results in the damped frequencies but the *undamped* modeshapes.

2.3.2 Damping.

There can be two methods to establish the damped frequencies :

1) Assume a damping ratio ζ, such that $\omega_{k,damped} = \omega_{k,natural}\sqrt{(1-\zeta^2)}$.

2) Use Modal analysis : Generalized damping is defined as $[C] = \zeta[C_{crit}]$, where the critical damping is $= [C_{crit}] = 2\sqrt{[M][K]}$; $\omega_{k,natural}$ = Eigen Values of $[M]^{-1}[K]$; and $\omega_{k,damped}$ = Eigen Values of $[K]/[M] - [C]^2/4[M]^2$. A similar model of *proportional damping* has been used by Man and Wilson [31,32].

Using the same value of the damping ratio ζ, the above two methods have been used to generate the damped frequencies of vibration for 3 different boundary conditions. The non-dimensional fundamental damped frequencies for a damping ratio of 10% are as follows (Table 2.1), which shows that the two methods generate the same damped frequency of vibration for 7 significant figures.

1^{st} *Non-D Damped Freq*	**CCCC**	**SSSS**	**CSCS**
Method 1	35.80497	19.64026	28.80575
Method 2	35.80497	19.64026	28.80575

Table 2.1 Fundamental damped frequencies of square plates with 10% damping.

The more rigorous Method 2 is important because the generalized damping matrices need to be established for the subsequent modal analysis, and the accuracy of the

damped frequencies generated thus can be compared to those generated by Method 1 for consistency. Damping reduces the dynamic amplification of the response of the plate, and thus reduces the DLF.

Here, the non-dimensional frequency is defined as $\omega_k \sqrt{\frac{mL^4}{D}}$.

2.3.3 Forced Vibration Analysis.

The governing differential equation for the forced, damped vibration of the Kirchhoff's plate is given by Eq.(2.9), where $F(x, y, t)$ is the transient pressure. The maximum structural response occurs early in the impact sequence, when the plate is assumed to be mostly dry. The fluid pressure field is not affected by the structural response.

$$m\frac{\partial Z^2(x,y,t)}{\partial t^2} + \mathbf{c}\frac{\partial Z(x,y,t)}{\partial t} + D\nabla^4 Z(x,y,t) = F(x,y,t). \tag{2.9}$$

Substitution of Eq.(2.6) into Eq.(2.9), and integration with weighting functions over the space, gives the normal mode expansion of the governing differential equations as a function of time only; with non-diagonal mass, damping and stiffness matrices, as follows:

$$\Sigma_{n=1}^{modex*modey} M_{kn}\ddot{q}_n(t) + \Sigma_{n=1}^{modex*modey} C_{kn}\dot{q}_n(t) + \Sigma_{n=1}^{modex*modey} K_{kn}q_n(t) = gf_k(t). \tag{2.10}$$

or writing in the matrix form $\quad [M]\{\ddot{q}(t)\} + [C]\{\dot{q}(t)\} + [K]\{q(t)\} = \{gf(t)\}.$

The generalized mass is defined as $M_{kn} = \int_0^L \int_0^B \Phi_k(x,y) m \Phi_n(x,y) dxdy$, the generalized stiffness is defined as $K_{kn} = \int_0^L \int_0^B \Phi_k(x,y) D\nabla^4 \Phi_n(x,y) dxdy$, the generalized forcing is defined as $gf_k(t) = \int_0^L \int_0^B \Phi_k(x,y) F(x,y,t) dxdy$, and the generalized damping is defined as $[C] = \zeta[C_{crit}]$, where the modal critical damping is defined as $[C] = 2\sqrt{[M][K]}$.

Eq.(2.10) is solved numerically by the stable Euler's implicit-explicit scheme, to calculate the principal coordinates $q_k(t)$ as a function of time. The principal coordinates are then multiplied by the corresponding plate modeshapes $\Phi_k(x, y)$ to generate the dynamic plate deflection $Z(x, y, t)$ as a function of space and time. Since pure bending is assumed and the deflections are small compared to the plate dimensions, the dynamic stresses developed are linearly proportional to the deflections. The instant and the location of the maximum deflection, and the maximum stress, are thus established.

2.3.4 Static Deflection

Commercial ship structural analysis involves the static analysis of a given plate panel, under an equivalent area load, i.e. the total forcing is assumed to be evenly distributed over the area of the plate. This work investigates the *dynamic* behavior of marine structures, and compares it the the static deflection due to the force of the *same configuration*.

The maximum static deflection of a square CCCC plate under a uniformly distributed load of 1 N/m^2 can be calculated by several methods as explained in Shames and Dym [63] as given below for the following geometric and material properties:
L = 1 m, B = 1 m, h = 0.001 m, E = 205 GPa, $\nu = 0.3$,

1) Timoshenko $\rightarrow$ 6.7118 x 10^{-5} m.

2) Ritz Method(1) $\rightarrow$ 6.8816 x 10^{-5} m.

3) Ritz Method(2) $\rightarrow$ 6.7251 x 10^{-5} m.

4) Kantorovich's Method $\rightarrow$ 6.6319 x 10^{-5} m.

5) Galerkin's Method $\rightarrow$ 6.7357 x 10^{-5} m. (This method is used in this analysis.)

2.4 Dynamic Load Factor.

The ratio of the dynamic deflection to the corresponding static deflection, under the equivalent loading conditions, is defined as the Dynamic Load Factor (DLF), i.e.

$$DLF = Max\left[\frac{Z(x,y,t)}{Max\{Z_{st}(x,y,t)\}}\right] \tag{2.11}$$

The static deflection $Z_{st}(x,y,t)$ is calculated by solving the following equation using Galerkin's method which includes the contribution of all the 3-D plate modeshapes. The classic static plate bending equation is :

$$D\nabla^4 Z(x,y,t) = F(x,y,t);$$

which gives

$$Z_{st}(x,y,t) = \Sigma_{j=1}^{modex}\Sigma_{l=1}^{modey} H_{jl}G_{jl}(x,y).$$

H_{jl} is the amplitude of the Galerkin's pre-multiplier $G_{jl}(x,y)$; and thus, it is the static counterpart of A_{jl}^k. Thus the DLF (Eq.(2.11)) forms a very important design parameter for the structural designer, who does the static analysis of the corresponding area load only.

As the impact load sweeps across the beam or plate (Fig.2.8), the static and the dynamic deflection both increase. The static deflection first increases and reaches its maximum at the midpoint when the peak pressure is also at the midpoint. As the dynamic defection increases, the static deflection has already seen to have started decreasing. The dynamic deflection reaches its maximum when the impact pressure has swept across the midpoint of the structure.

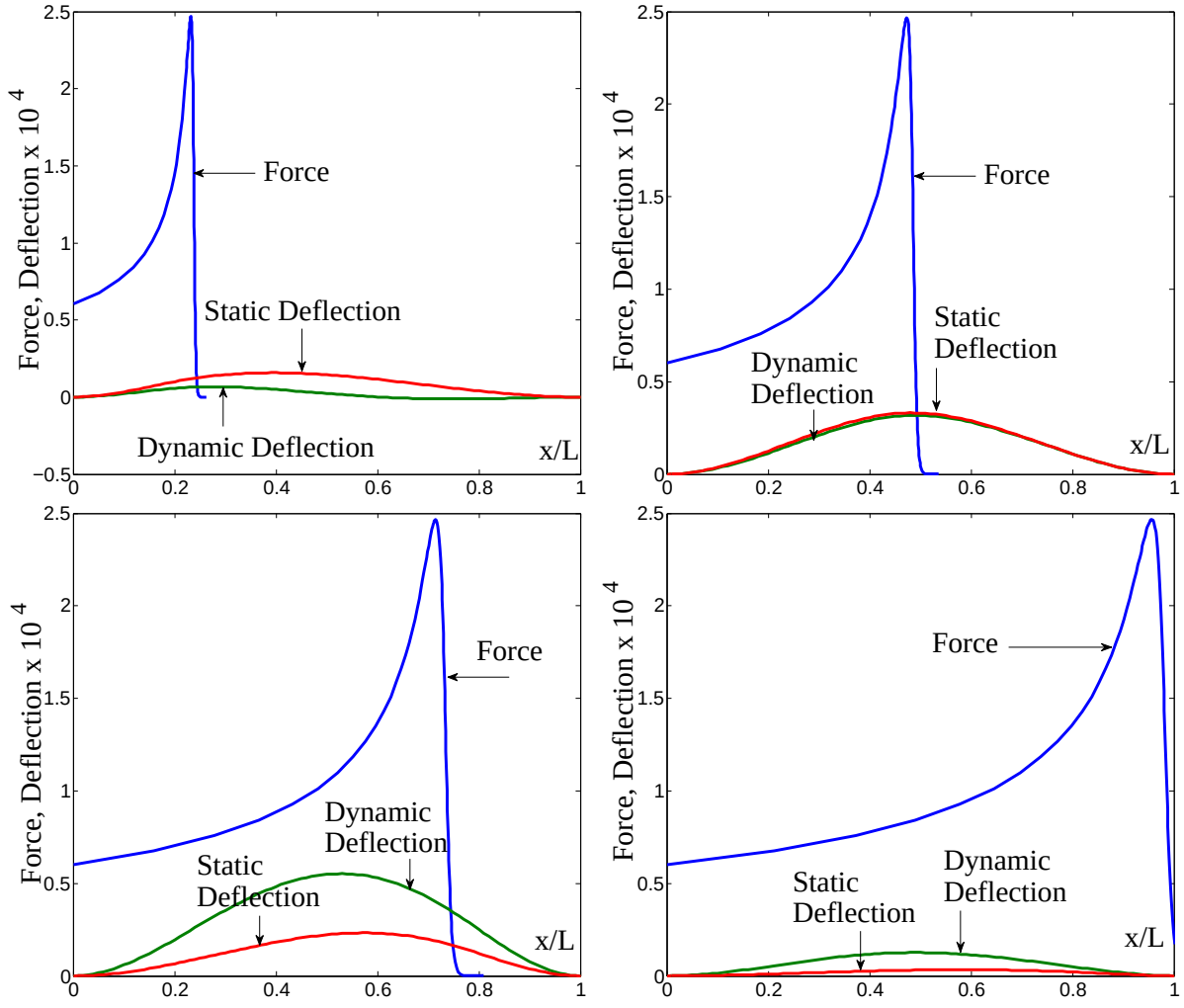

Figure 2.8: Sweeping load at deadrise $\beta = 15$ degrees, with the corresponding static and dynamic deflection (dry modes : no added mass).

At 25% wetting, the instantaneous DLF = 0.4271, i.e. the dynamic deflection is only 43% of the static deflection under the same loading configuration. When the impulse reaches halfway (50% wetting), the DLF rises to 0.9613. Now the static deflection starts decreasing and the DLF at 75% wetting becomes 2.3718. Once the peak pressure leaves the beam span, the static deflection decreases further, while the dynamic deflection picks up. At complete sweep, (100% wetting), the instantaneous DLF = 3.7478.

Once the impulse has swept across, the static deflection asymptotes to zero, but the dynamic deflection continues in the absence of damping, i.e. the structure keeps ringing at its natural frequency.

2.5 Relative Modal Contribution.

The total dynamic deflection is the summation of the modeshapes $\Phi_k(x, y)$, weighted by the time-dependent principal coordinates $q_k(t)$. The modeshapes have been normalized to 1, and thus the amplitudes of the principle coordinates generate the Relative Modal Contribution (R.M.C.). The forced vibration has been studied for 15x15 = 225 modeshapes, which ensures the numerical accuracy of the first 49 modeshapes and frequencies, up to the first 5 significant figures.

The participation of the different modes of vibration with respect to the dominant first mode was studied to determine the modal truncation limits (Eq.(2.12)). In this work, the normalized truncation limit is set to 10^{-3}. Modal amplitudes that have a RMC less than -3 are safely ignored. The relative modal contribution is quite sensitive to the impact speed. A slow speed or a stiff plate excites only the first few modes, making it possible to ignore the higher-order modes. A high impact velocity or a softer plate, on the other hand, excites higher modeshapes, necessitating the inclusion of more

number of modes, i.e. increasing the modal truncation limit, thereby consuming more computational time.

High values of the impact speed requires k = 225 modes to meet the $O(10^{-3})$ truncation criterion

$$Max\left[\frac{q_k(t)}{Max\{q_1(t)\}}\right] \geq 10^{-3}, \quad Log_{10}Max\left[\frac{q_k(t)}{Max\{q_1(t)\}}\right] \geq -3 \tag{2.12}$$

for all time t.

2.6 Parameter Space.

The dynamic response of the elastic plate, subject to transient hydrodynamic impact, is a function of several parameters, namely the added mass, the damping ratio, the deadrise angle, the aspect ratio, and the boundary conditions. Both the independent variable τ and the dependent variable DLF are functions of all of them.

2.6.1 Added Mass.

Added mass greatly lowers the natural frequency of the plate. Each modeshape is associated with its own modal added mass. The decrease in the natural frequencies depends on the spatial configuration of each modeshape. The time-scale of the problem gets compressed, thereby *squeezing* the DLF characteristic to lower values of τ. It, however, does not influence the peak DLF magnitude, which depends on the impact forcing magnitude and configuration.

2.6.2 Damping ratio.

Damping reduces the frequency of the plate, and decreases the dynamic amplification

of the elastic response, thereby reducing the peak DLF. This analysis has been done for $\zeta = 0.00$ and 0.20. The structural damping is not specified as a material property here, but as a modal parameter. The generalized damping is assumed to be the damping ratio ζ times the generalized critical damping for each modeshape. Hence this damping is *proportional* to the mass and stiffness properties of the plate. Damping reduces the peak amplification of the DLF, thus lowering the stress levels generated.

Purcell et al [48] experimentally studied the structural strength and reliability of patrol boats, subject to hydrodynamic impact loads. The times series of the stresses generated on the keel, bottom plating and stiffeners showed at damping of around $\zeta \approx$ 10%-15%. Thus the range of damping ratios considered in this work are inclusive of the usual damping present in marine structures.

2.6.3 Deadrise angle.

The deadrise angle β of the vessel, changes the wetting time of the plate, and the magnitude and distribution of the loading. The smaller the deadrise angle (Fig.2.9), the faster the wetting, the more *localized* the hydrodynamic pressure, and the more intense peak pressure. This analysis has been done for deadrise angles $\beta = 1$, 5, 15 and 30 degrees.

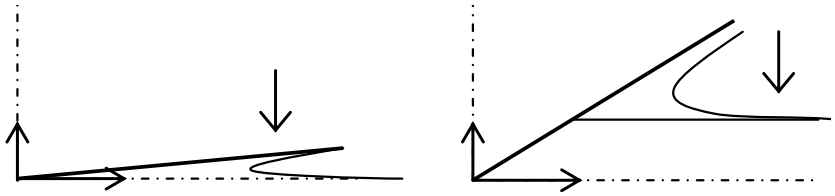

Figure 2.9: Deadrise angle (a) 5 degree and (b) 30 degree.

2.6.4 Boundary conditions.

This work considers four boundary conditions, namely CCCC, SSSS, CSCS (two orientations). The natural frequency of vibration of the plate changes due to the end conditions (Fig.2.10). The clamped end has zero deflection and zero slope, i.e. 100% fixity. The simply supported end has zero deflection and zero bending moment (curvature), i.e. 0% fixity (Fig.2.11). Thus this work examines the two extremes of end fixities, which would include all the practical intermediate fixities of structural components of the hull. Also, the added mass depends on the plate modeshape, which in turn depends on the end conditions. The stiffness hierarchy remains the same in wet vibration, i.e. CCCC being the stiffest and SSSS being the softest.

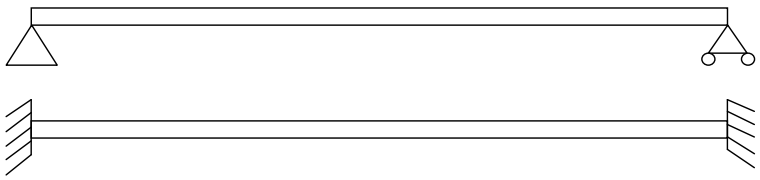

Figure 2.10: Boundary conditions (a) Simply-Supported and (b) Clamped-Clamped.

The *four* boundary conditions are as follows :

(a) **CCCC** : **C**lamped (built-in) on all sides.

(b) **SSSS** : **S**imply supported on all sides.

(c) **CSCS** : The opposite sides are **C**lamped and **S**imply Supported : the forcing is parallel to SS edges. The CC beam modeshape is along the forcing.

(d) **SCSC** The opposite sides are **S**imply Supported and **C**lamped : the forcing is parallel to CC edges. The SS beam modeshape is along the forcing.

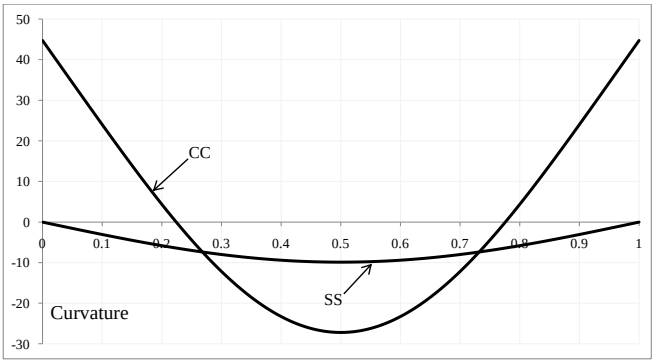

Figure 2.11: Curvature of the first modeshape of a CC and SS beam.

2.6.5 Aspect ratio.

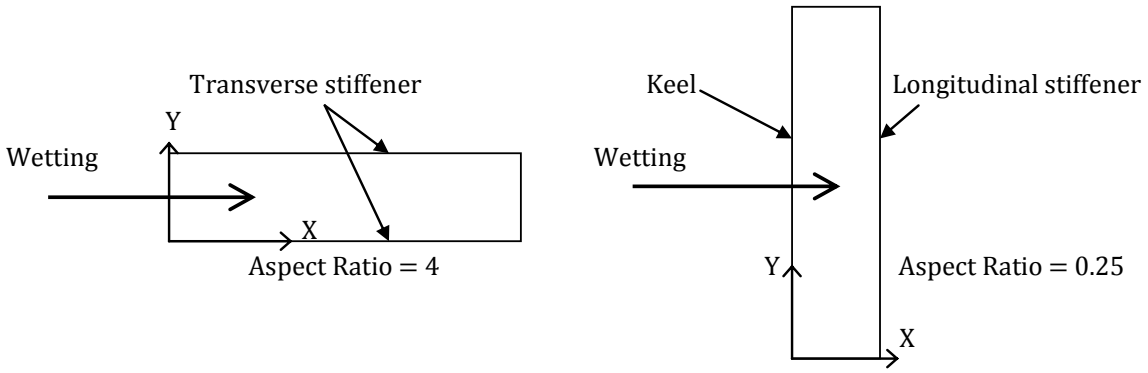

Figure 2.12: Transient Load on Rectangular plates.

The aspect ratio (Fig.2.12) changes the natural frequency of the plate and the wetting time. The free vibration analysis has been done for aspect ratios α = 10, 5, 4, 3, 2, 1, 0.5, 1/3, 0.25, 0.2, 0.1. The forced vibration analysis has been done for a fewer number of aspect ratios, to demonstrate the distinct dynamic behaviors. Plates with α = a and α = 1/a have different DLF characteristics, except at very low α, when the

two DLFs approach a unique value. At large aspect ratios, the natural frequencies and DLFs of CSCS plates approach that of a Clamped-Clamped (CC) beam, and those of and SCSC plate approach that of a Simply-Supported (SS) beam. The DLFs for $\alpha < 1$ approach that of an Euler-Bernoulli beam, while the DLFs for $\alpha > 1$ move away from the $\alpha = 1$ characteristic, to a trend where little vibration occurs.

2.7 Family of problems.

Including the above parameters, the following vibration problems are solved, as listed below. Table 2.2 lists the parameter space of the dry beam vibration problem.

Dry Beam	Boundary Conditions		Damping Ratio %					Deadrise Angle (degrees)			
Uniform Load	CC	SS	0	1	5	10	20				
Impact Load	CC	SS	0	1	5	10	20	1	5	15	30

Table 2.2 Family of dry beam vibration problems.

Table 2.3 shows the parameter space of the dry plate vibration problem. The additional parameter of aspect ratio multiplies the number of problems, and hence the computation time. The parameter space for the wet plate vibration is the same as that of the dry vibration.

Dry Plate	Boundary Conditions				Damping Ratio %		Deadrise Angle (degrees)				Aspect Ratio			
Uniform Load	CC	SS	CS	SC	0	20					1	2	5	10
	CC	SS	CS	SC								0.5	0.2	0.1
Impact Load	CC	SS	CS	SC	0	20	1	5	15	30	1	2	5	10
	CC	SS	CS	SC								0.5	0.2	0.1

Table 2.3 Family of dry plate vibration problems.

CHAPTER III

DRY VIBRATION OF EULER-BERNOULLI BEAM

3.1 Beam Vibration : Modal Analysis.

The transient impact loads can be modelled as a distributed stretching load moving across a beam of unit breadth, at a constant speed c. Considering undamped forced vibrations, the dynamic response $\mathrm{Z}(x,t)$ of the beam as a function of space and time is evaluated numerically by the fourth-order Runge-Kutta method. Since the fundamental mode is assumed dominant, it is sufficient to consider only *pure* bending of the beam (*Euler-Bernoulli beam*), ignoring shear deformation and rotary inertia (*Timoshenko beam*). The corresponding static deflections $Z_{st}(x,t)$ are calculated by numerical integration, given the impact load $\mathrm{F}(x,t)$. The ratios of the dynamic and static deflections give the DLF.

3.1.1 Free Vibration

The free vibration equation of motion for the beam, ignoring gravity, is

$$m(x)\frac{d^2Z(x,t)}{dt^2} + EI(x)\frac{d^4Z(x,t)}{dx^4} = 0. \tag{3.1}$$

The mass $\mathrm{m}(x)$ and the stiffness $\mathrm{EI}(x)$ is assumed to be uniformly distributed over the length of the beam. The longitudinal strain due to the small amplitude vibrations of the beam are assumed to be too small to cause negative lateral strains. So the Poisson's ratio term in the flexural rigidity is ignored.

The deflection is a linear superposition of the Eigen vectors

$$Z(x,t) = \Sigma_{j=1}^{\infty}\phi_j(x)q_j(t)$$

where $\phi_j(x) = j^{th}$ modeshape function and $q_j(t) = j^{th}$ principle coordinate. The modeshape are the Eigen vectors of Eq.(3.1)

$$\phi_j(x) = A1_j cos(\gamma_j x) + A2_j sin(\gamma_j x) + A3_j cosh(\gamma_j x) + A4_j sinh(\gamma_j x). \tag{3.2}$$

where $\gamma_j = \omega^2_{j,dry}\left(\frac{m}{EI}\right)$ are the corresponding Eigen values of Eq.(3.1). The four constants A1, A2, A3 and A4 in Eq.(3.2) are calculated from the four boundary conditions of the beam, i.e.

$$Z(0,t) = Z(L,t) = 0; \quad \frac{dZ(0,t)}{dx} = \frac{dZ(L,t)}{dx} = 0 \quad \text{for a Clamped-Clamped beam;}$$
$$Z(0,t) = Z(L,t) = 0; \quad \frac{d^2Z(0,t)}{dx^2} = \frac{d^2Z(L,t)}{dx^2} = 0 \quad \text{for a Simply-Supported beam.}$$

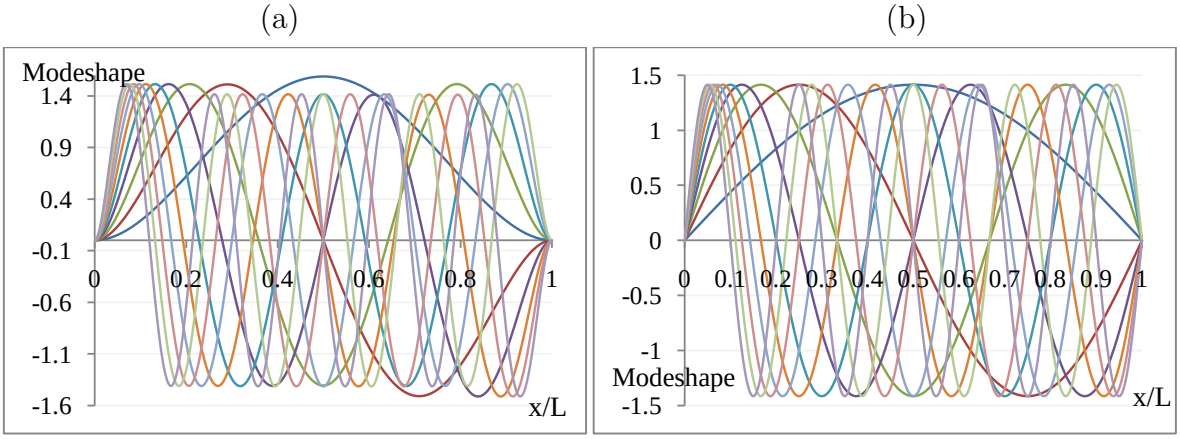

Figure 3.1: First 10 beam modeshapes (a) CC beam, (b) SS beam.

There are an infinite number of distinct values of γ_j, each of which corresponds to distinct natural frequencies ω_j and modeshapes $\phi_j(x')$ (Fig.3.1). The CC modeshapes are given as: $\phi_j(x') = cos(\gamma_j x') - cosh(\gamma_j x') - \sigma_j sin(\gamma_j x') + \sigma_j sinh(\gamma_j x')$.

The first five wave numbers are $\gamma = 4.7300$, 7.8532, 10.9956, 14.1372, 17.2787. The higher order wave numbers are given as $\gamma_j = (2j+1)\frac{\pi}{2}$ (Gonclaves[70]). For modes > 5, the closed form expressions for the modeshape $\phi_j(x')$ are given in Appendix 1. Calculation of γ_j determines $\omega_{j,dry}$, the dry natural frequencies of the beam.

The SS modeshapes are given as $\phi_j(x') = sin(\gamma_j x')$; with the wave number given as $\gamma_j = j\pi$.

3.1.2 Forced Vibration

The forced vibration equation of motion for the beam is given as

$$m(x)\frac{d^2Z(x,t)}{dt^2} + EI(x)\frac{d^4Z(x,t)}{dx^4} = F(x,t).$$

The governing system of differential equations is non-dimensionalized with respect length and time as $dt' = \omega_{1,dry}$ dt and $dx' = \frac{dx}{L}$. Thus the governing differential equation, including the hydrodynamic external sectional force $(\frac{N}{m})$, is given as :

$$m(x')\Sigma_{j=1}^{\infty}\phi_j(x')\frac{d^2q_j(t')}{dt'^2} + EI(x')\Sigma_{j=1}^{\infty}\frac{d^4\phi(x')}{dx^4}q_j(t') = F(x',t'). \tag{3.3}$$

Taking advantage of the orthogonality property of the Eigenvectors $\phi_j(x)$, the set of equations (Eq.(3.3)) is pre-multiplied by the j^{th} modeshape and integrated over the length. The resulting uncoupled non-dimensional modal equation of motion follows:

$$M_{jj}\omega_{1,dry}^2\frac{d^2q_j(t')}{dt'^2} + K_{jj}q_j(t') = gf_j(x',t'), \tag{3.4}$$

where Generalized mass is given as $M_{jj} = \int_L \phi_j(x')m(x')\phi_j(x')dx'$;
Generalized forcing is given as $= gf_j(t') = \int_L \phi_j(x')F(x',t')dx'$;
Generalized stiffness is given as $K_{jj} = \int_L \phi_j(x')EI(x')\frac{d^4\phi_j(x')}{dx'^4}dx'$ and $\frac{K_{jj}}{M_{jj}} = \omega_{j,dry}^2$.

Utilizing the above relations, Eq.(3.4) can be re-written as follows :

$$\frac{d^2 q_j(t')}{dt'^2} + \left(\frac{\omega_{k,dry}^2}{\omega_{1,dry}^2}\right) q_j(t') = \frac{g f_j(t')}{M_{jj}\omega_{1,dry}^2}. \tag{3.5}$$

Thus we obtain the uncoupled system of ordinary differential equations (Eq.(3.5)) for the principal coordinates $q_j(t)$. This system of non-dimensional governing differential equations is solved by numerical time integrators, Euler's implicit-explicit scheme and the Fourth order Runge-Kutta method. Once the principle coordinates $q_j(t)$ have been evaluated, they are multiplied by the pre-calculated modeshape functions $\phi_j(x)$ to generate the total dynamic deflection $Z(x,t)$ as a function of space and time. Fig.3.2 shows the deflection, velocity and the acceleration of the mid-point of the beam as a function of time.

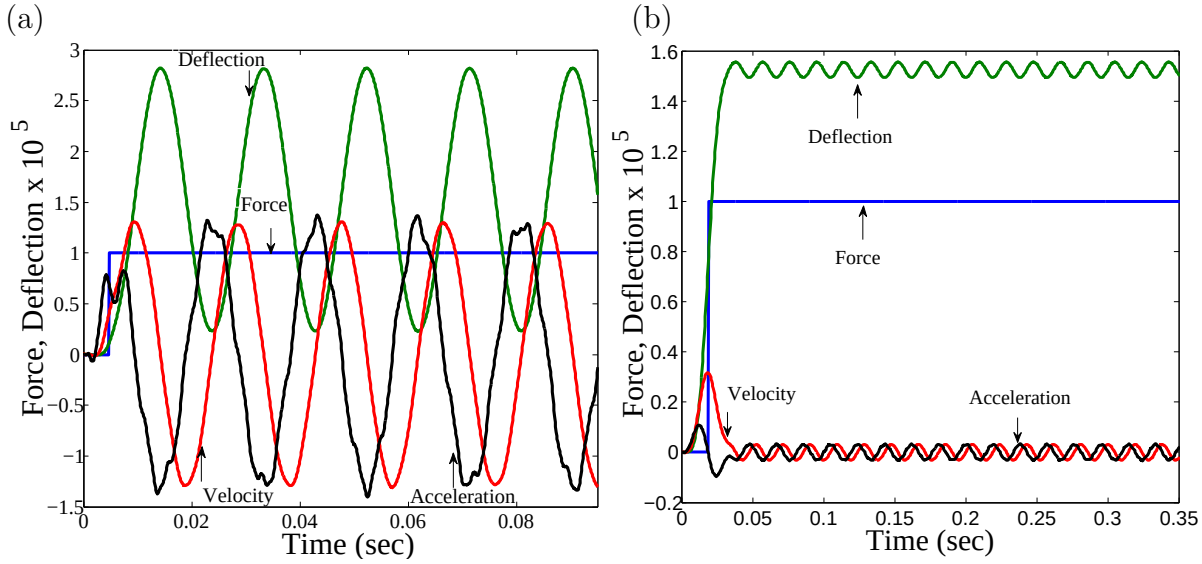

Figure 3.2: Force, Mid-point Deflection, Velocity and Acceleration at (a) $\tau = 0.5$ (b) $\tau = 2.0$.

3.1.3 Dynamic Loading Factor

The dynamic load factor DLF can be defined in one of the following four ways, where $Z(x,t)$ is the dynamic deflection and $Z_{st}(x,t)$ is the equivalent static defection.

1) The dynamic deflection is divided by the maximum possible static deflection in space and time. The ratio is a function of space and time. The maximum ratio in space and time is defined as the DLF_1.

$$DLF_1 = Max\left[\frac{Z(x,t)}{Z1_{st}}\right]. \tag{3.6}$$

2) The dynamic deflection at every time step is divided by the maximum static deflection at the corresponding time-step. The ratio itself is a function of time, and the maximum of that is chosen as DLF_2.

$$DLF_2 = Max\left[\frac{Z(x,t)}{Z2_{st}(t)}\right].$$

3) The dynamic deflection at every location is divided by the maximum static deflection at the corresponding location. The ratio itself is a function of space, and the maximum of that is chosen as DLF_3.

$$DLF_3 = Max\left[\frac{Z(x,t)}{Z3_{st}(x)}\right].$$

4) The dynamic deflection at every location and time-step is divided by the static deflection at the corresponding location and the time-step. The ratio is a function of space and time. The maximum of this ratio is DLF_4.

$$DLF_4 = Max\left[\frac{Z(x,t)}{Z_{st}(x,t)}\right].$$

Warning : Do not divide by $Z_{st}(0,t)$, since the deflection is zero to the ends.

For the analysis and discussion, DLF_1 (Eq.(3.6)) is chosen. It is the most robust DLF, since the structural designer will not require the spatial and temporal distribution of the static deflection to calculate the corresponding maximum dynamic deflection.

3.1.4 Relative Modal Contribution

For the loading conditions studied in this work, the fundamental mode of vibration $Z_1(x,t)$ is the principal contributor to the total displacement, the contributions of the higher modes decreasing exponentially. Modal truncation studies of Section 3.2.2 demonstrate that modes contributing less than 10^{-6} times the fundamental mode can be safely ignored. The j^{th} principle coordinate $q_j(t)$ is normalized by the fundamental principle coordinate $q_1(t)$ to generate the Relative Modal Contribution (RMC) for different impact velocities, i.e.

$$RMC_j = log_{10}\left[Max\frac{q_j(t')}{Max\{q_1(t')\}}\right]. \tag{3.7}$$

In the beam vibration analysis in this thesis, the first 30 modes of vibration have been considered, which renders $RMC_{30} < -7$. This means that the highest mode has a contribution 10^{-7} times that of the fundamental mode, and hence can be safely ignored within the limits of engineering accuracy.

3.1.5 Response at zero wetting time.

For zero wetting time, i.e. $\tau = 0$, the uniform load acts over the whole of the beam from time $t = 0$ onwards. This represents an impact at infinite speed; or a plate of zero stiffness/infinite mass. The forced vibration equation of motion for the beam is given as

$$m(x')\frac{d^2Z(x',t')}{dt'^2} + EI(x')\frac{d^4Z(x',t')}{dx'^4} = 1. \tag{3.8}$$

3.2 Dynamic response of beams to uniform stretching load.

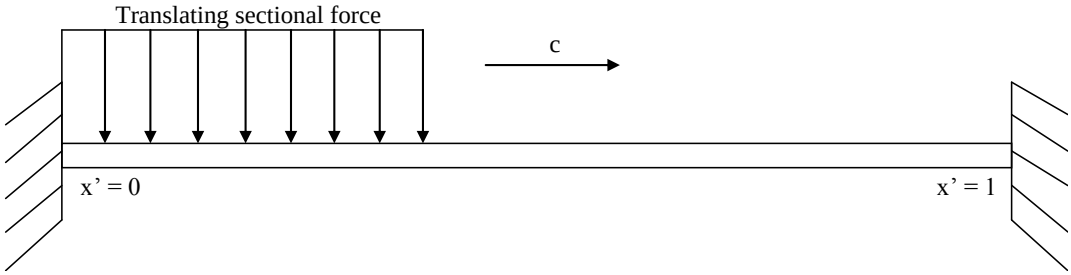

Figure 3.3: Uniform load moving across the beam at a speed c.

The dynamic response of a uniform beam to a uniformly distributed load of unit magnitude, stretching at a speed c across the beam (Fig.3.3), is analyzed with normal mode summation, generating the dynamic load factor (DLF) and the modal contribution (RMC) surface.

$$T_{sp} = \frac{L}{c}, \qquad \tau = \frac{L}{c}\frac{\omega_{1,dry}}{2\pi}.$$

3.2.1 Dynamic Loading Factor.

At large values of τ, the dynamic and static deflection at the midpoint of the beam both rise as the wetting time as shown in Fig.3.4. Then $Z(x, y, t)$ oscillates about the static deflection time series. The DLF equals 1.0204, i.e. the dynamic overshoot is only 2.04% more than the $Z_{st}(x, y, t)$. At this τ, the behavior is seen to be quasi-static. Inclusion of 5% damping reduces the DLF to 1.0203. The $Z(x, y, t)$ asymptotes to less than $\pm 0.1\%$ of $Z_{st}(x, y, t)$ after about 15 oscillations. Reducing the wetting time leads to a more dynamic response as shown in Fig.3.5. Undamped vibration at $\tau = 0.5$ produces a DLF of 1.8562, i.e. the dynamic overshoot is as much as 85.6%. Inclusion of 5% damping reduces the DLF to 1.7385.

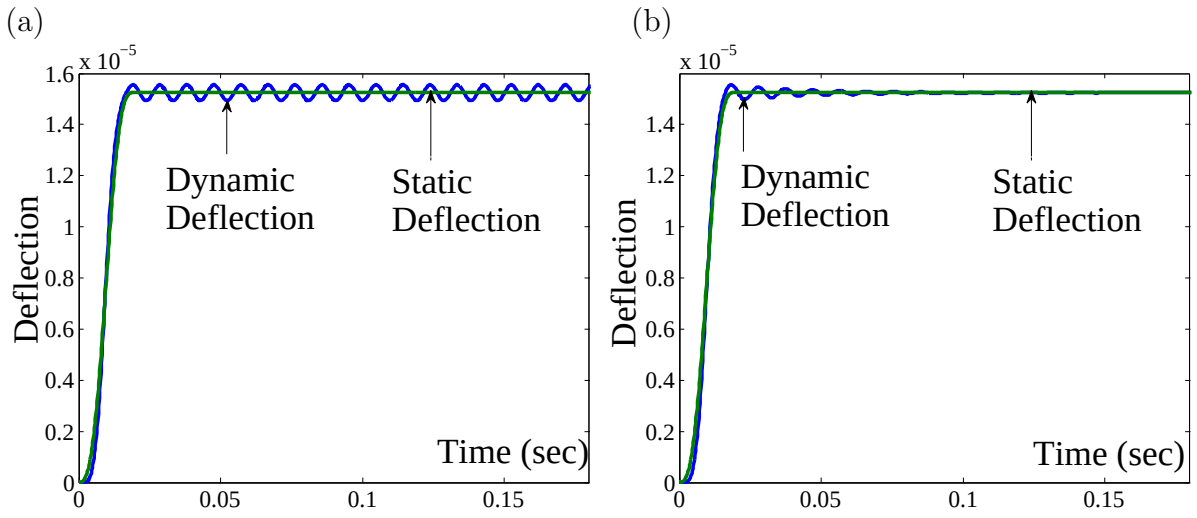

Figure 3.4: Time Series of a CC beam at $\tau = 2.0$, for (a) 0% damping and (b) 5% damping.

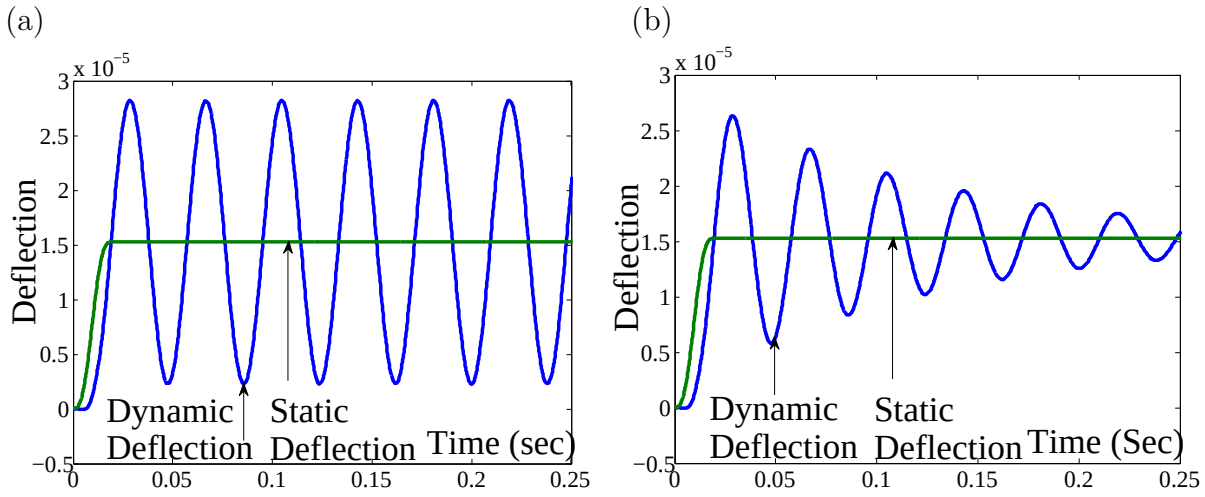

Figure 3.5: Time Series of a C-C beam at $\tau = 0.05$, for (a) 0% damping and (b) 5% damping.

The DLF of the CC and SS beams to the above moving load has been shown in Fig.3.6 and Fig.3.7 respectively. At low speeds, it is close to 1, i.e.the structural response is nearly quasi-static. Thus this response cannot be considered as a slamming-response. For both the boundary conditions, static analysis is expected to suffice for $\tau \geq 2.5$.

For $\tau \leq 2$, the dynamic response becomes increasingly prominent, showing considerable overshoots above the static analysis. At smaller τ the DLF steeply rises to asymptote to $\sim$2.00, which is the DLF for a uniformly distributed load instantaneously acting on the beam. The response for $\tau < 1$ can be said to be a slamming-response, which is somewhat restricted by the damping. The response at zero damping provides the upper limit of the response characteristic for a range of τ.

The designer aims to design structure with the boundary conditions and, stiffness and damping such that the composite time-scale τ is greater than 2.5 for the most probable impact velocities. To operate in the quasi-static range, the forcing speed should be low, or the natural frequency of the beam must be high. A craft meant for inland operations (i.e. calm waters) can afford a softer structure, where slamming is less common. A sea-going vessel, on the other hand would require a stiffer bottom structure to ensure a quasi-static response. High-speed vessels, though use mostly in calm waters, needs stiffer material, since the varying dynamic lifts (partially supporting the craft weight) cause repeated slamming of the bow at high impact speeds.

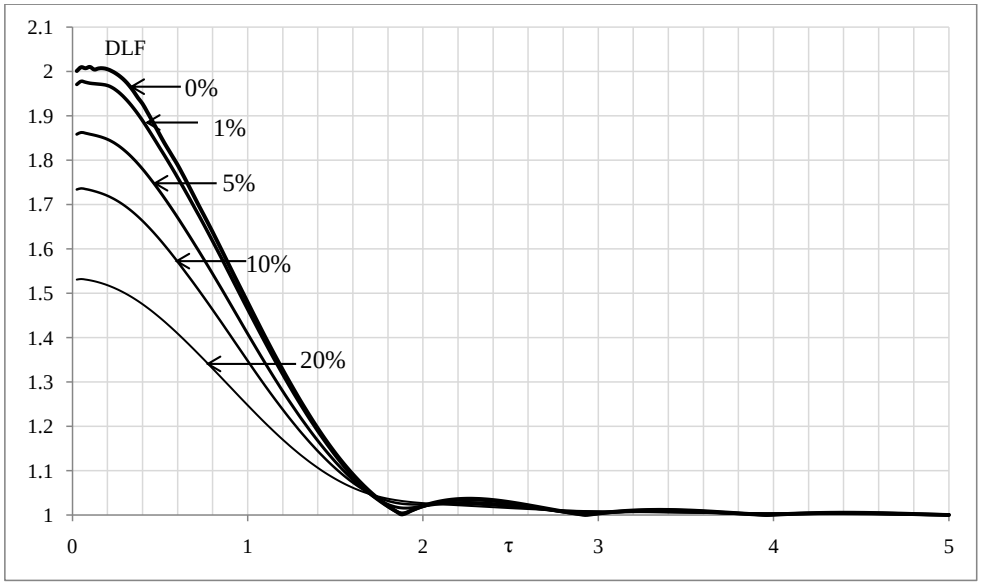

Figure 3.6: DLF of C-C Beam in response to Uniform Stretching Load, at five different damping ratios.

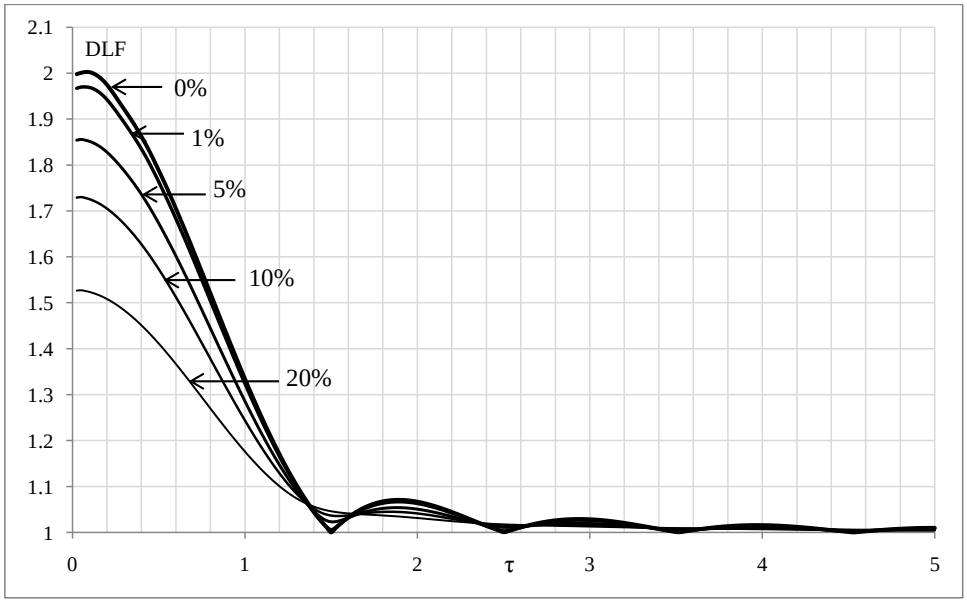

Figure 3.7: DLF of S-S Beam in response to Uniform Stretching Load, at five different damping ratios.

3.2.2 Relative Modal Contribution.

The modal contribution of the CC and SS beams to the above uniform stretching load at various transient speeds has been shown in Fig. 3.8 and 3.9. It is seen that the 20^{th} mode contributes to the order of 10^{-6} times the first mode. This modal truncation study serves as a representative guideline for other forcing configurations, where the modal superposition limit is set to the first 20 modes. The even modeshapes integrate to zero, whereas the odd ones integrate to non-zero. Since the load is uniformly distributed over the length, the odd modeshapes are more likely to be excited than the even ones. Interestingly, at relatively high speeds (small τ), the RMC surface shows a particular higher mode (hence a corresponding higher frequency of vibration) is excited for a given speed. The modal contribution for $\tau < 0.25$ is not as smooth, with each speed associated with a particular vibratory overtone.

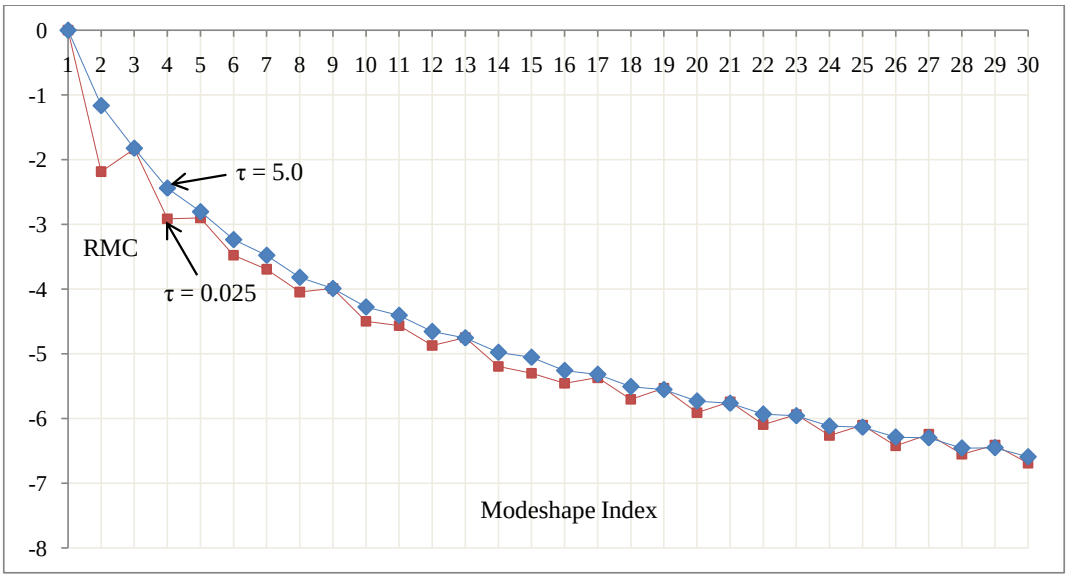

Figure 3.8: RMC of C-C beam for uniform load.

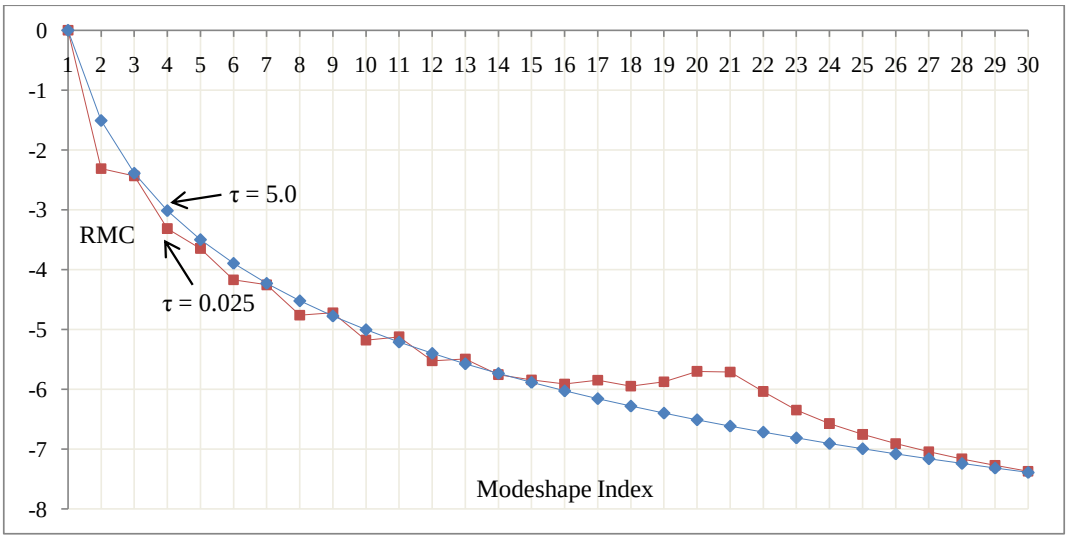

Figure 3.9: RMC of S-S beam for uniform load.

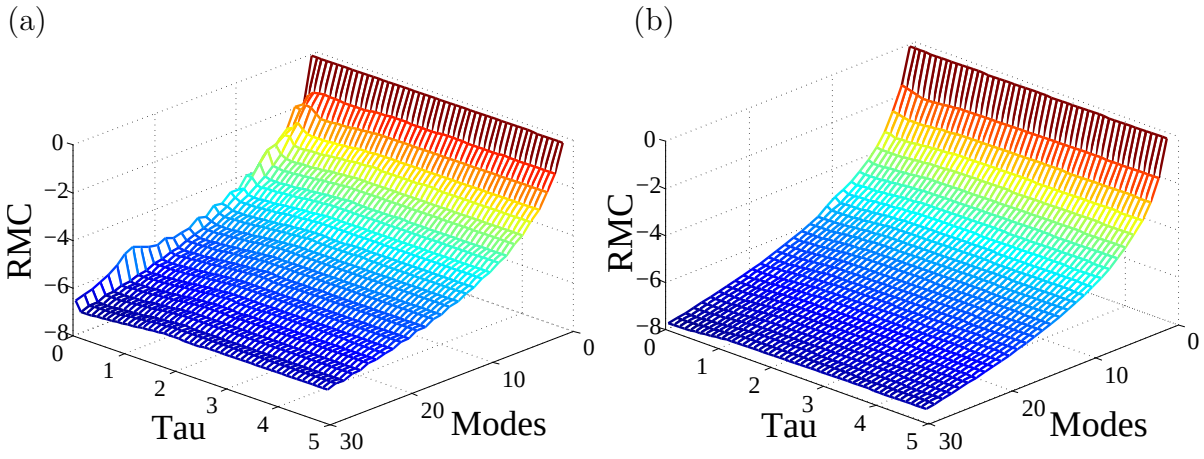

Figure 3.10: RMC contours for uniform load on a (a)CC beam (b)SS beam.

Fig.3.10 shows the RMC contours of a CC and SS beam to a uniform load over a range of values of τ. Inclusion of the first 30 modeshapes for a CC beam shows that the RMC for the highest mode is less than -6; and for a SS beam, it is less than -7. The higher the modeshape index, the less is its contribution to the dynamic response, because the loading configuration excites only the first few modeshapes. The pattern is consistent except for very small values of τ, when the impact speed is so much that the higher order modes also contribute to the deflection.

3.2.3 Response at Zero Wetting time.

For $\tau = 0$, the numerical analysis for a uniformly distributed load acting on the beam instantaneously (Eq.3.8) yields the following results (Table 3.1).

Uniform Load	$\zeta = 0\%$	$\zeta = 1\%$	$\zeta = 5\%$	$\zeta = 10\%$	$\zeta = 20\%$
CC	2.008	1.978	1.863	1.737	1.533
SS	2.000	1.970	1.857	1.732	1.529

Table 3.1 DLF at $\tau = 0$ for CC and SS beams, at 5 damping ratios.

The DLF for a CC beam asymptotes to 2.008, while that of a SS beam goes to 2 within numerical accuracy. Damping reduces this maxima to a lower dynamic amplification. The CC beam consistently shows a DLF greater than the SS beam, due to its greater curvature (bending moments).

3.3 Dynamic response of beams to impact load.

The response of the beam to the uniform stretching load helps establish the benchmarks of the modal analysis, namely the time-scales, DLF, and RMC. Now we proceed

to a more realistic model of the impact force distribution, defined by a moving jet head, stretching from the keel upwards (from $x' = 0$ to $x' = 1$ and beyond). The maximum pressure is a function of the vertical impact velocity V and the deadrise angle β.

3.3.1 Dynamic Loading Factor.

Applying the impact forcing on the dry beam at various impact speeds, the dynamic load factor (DLF) is estimated by the normal mode analysis. At large τ, the response is nearly quasi-static (DLF ≈ 1) irrespective of the deadrise angle.

Fig.3.11 shows the time series of the dynamic and static deflection of the midpoint of a clamped-clamped beam at $\tau = 1.0$, for a deadrise angle of $\beta = 15$ degrees. The undamped vibration produces a DLF = 1.6508, i.e. the dynamic overshoot is about 65% more than the static deflection under an equivalent loading. Inclusion of 20% damping reduces the DLF to 1.3048, i.e. a 30.5% dynamic overshoot over the static deflection. It is interesting to note that, with 20% damping, there is only one dynamic oscillation greater than the static maximum (the first one). Sufficient damping causes the subsequent dynamic stress maximum to be less than the static maximum.

Fig.3.12 shows the times series of the dynamic and static deflection of the midpoint of a clamped-clamped beam at $\tau = 0.2$ and 2.5, for a deadrise angle of $\beta = 15$ degrees. The behavior at $\tau = 2.5$ is quasi-static, with the dynamic deflection rising approximating the static deflection during the impulsive wetting, and then ringing about the zero mean. The static deflection is negligible after the impact load has passed. The DLF is 1.1136, i.e. only 11.4% dynamic overshoot greater than the static deflection.

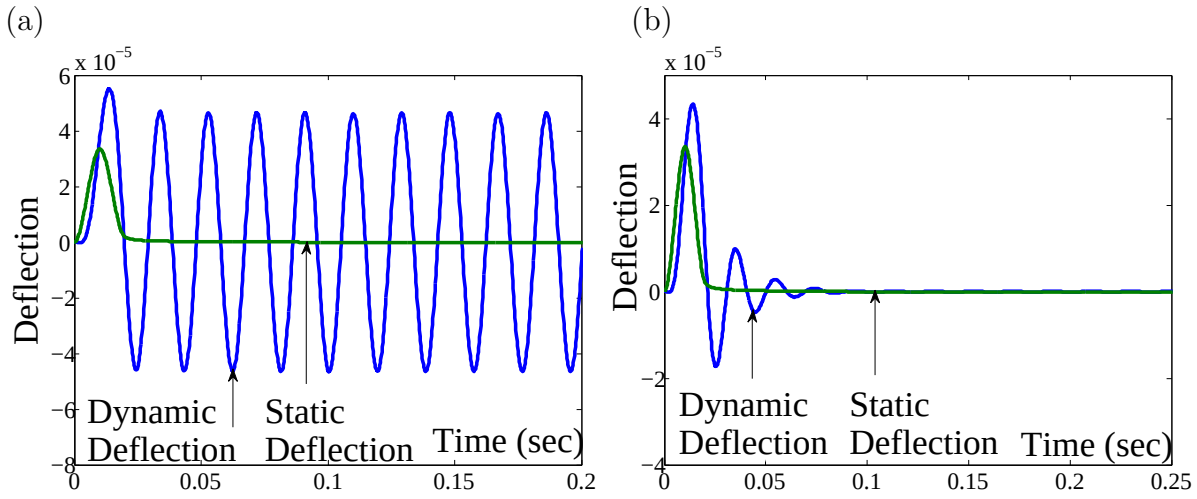

Figure 3.11: Undamped and damped time series of a C-C beam at $\tau = 1.0$ for (a) 0% damping and (b) 20% damping, in response to impact loading at $\beta = 15$ degrees.

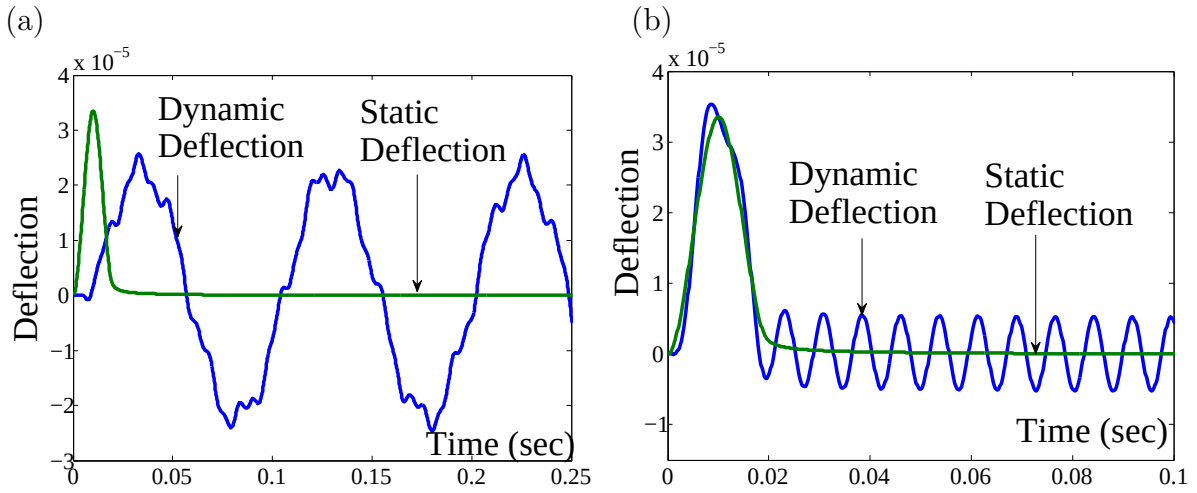

Figure 3.12: Undamped time series of a C-C beam at (a)$\tau = 0.2$, (b)$\tau = 2.5$, in response to impact loading at $\beta = 15$ degrees.

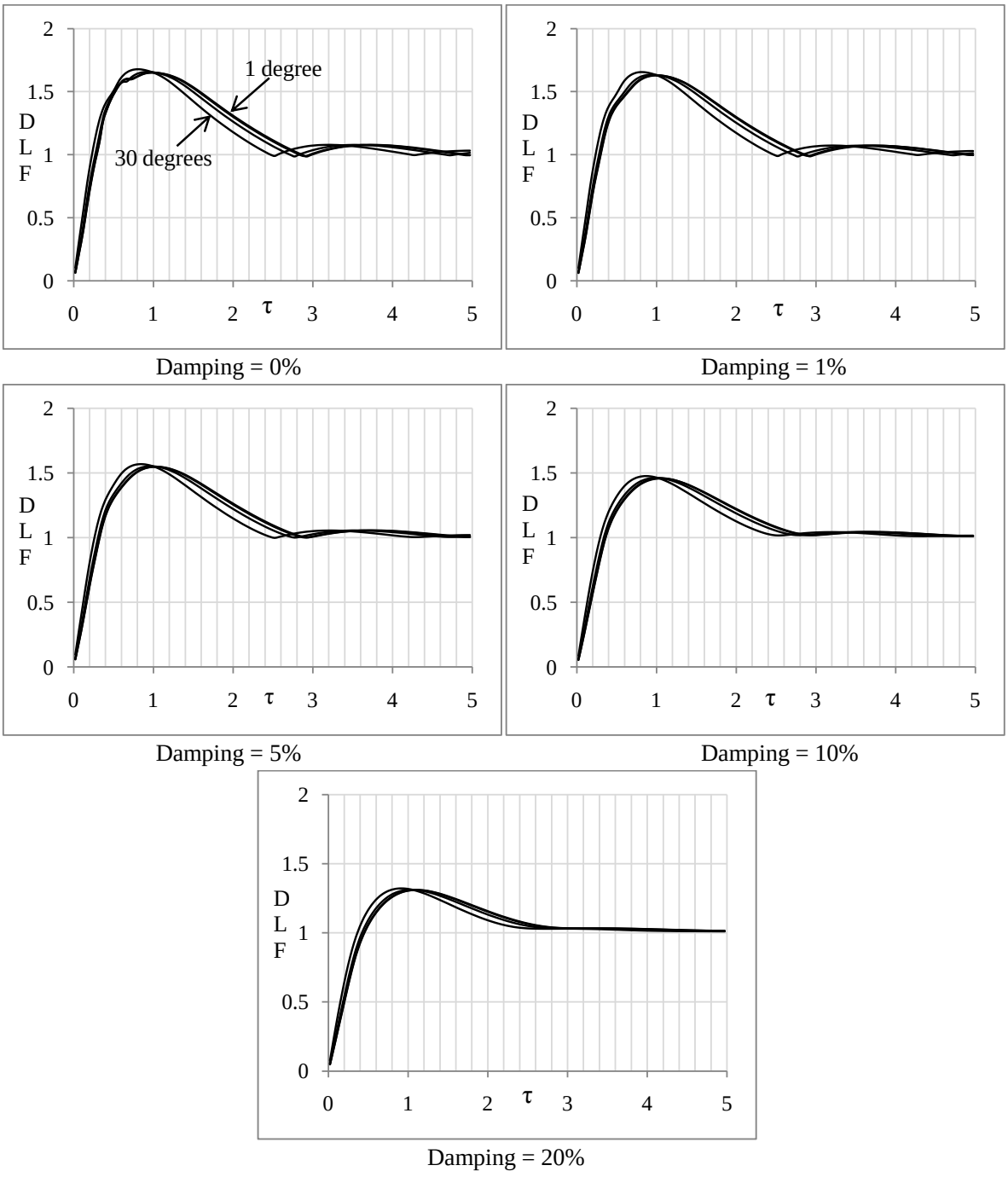

Figure 3.13: DLF for CC beam, subject to Impact loading, at 5 damping ratios and 4 deadrise angles.

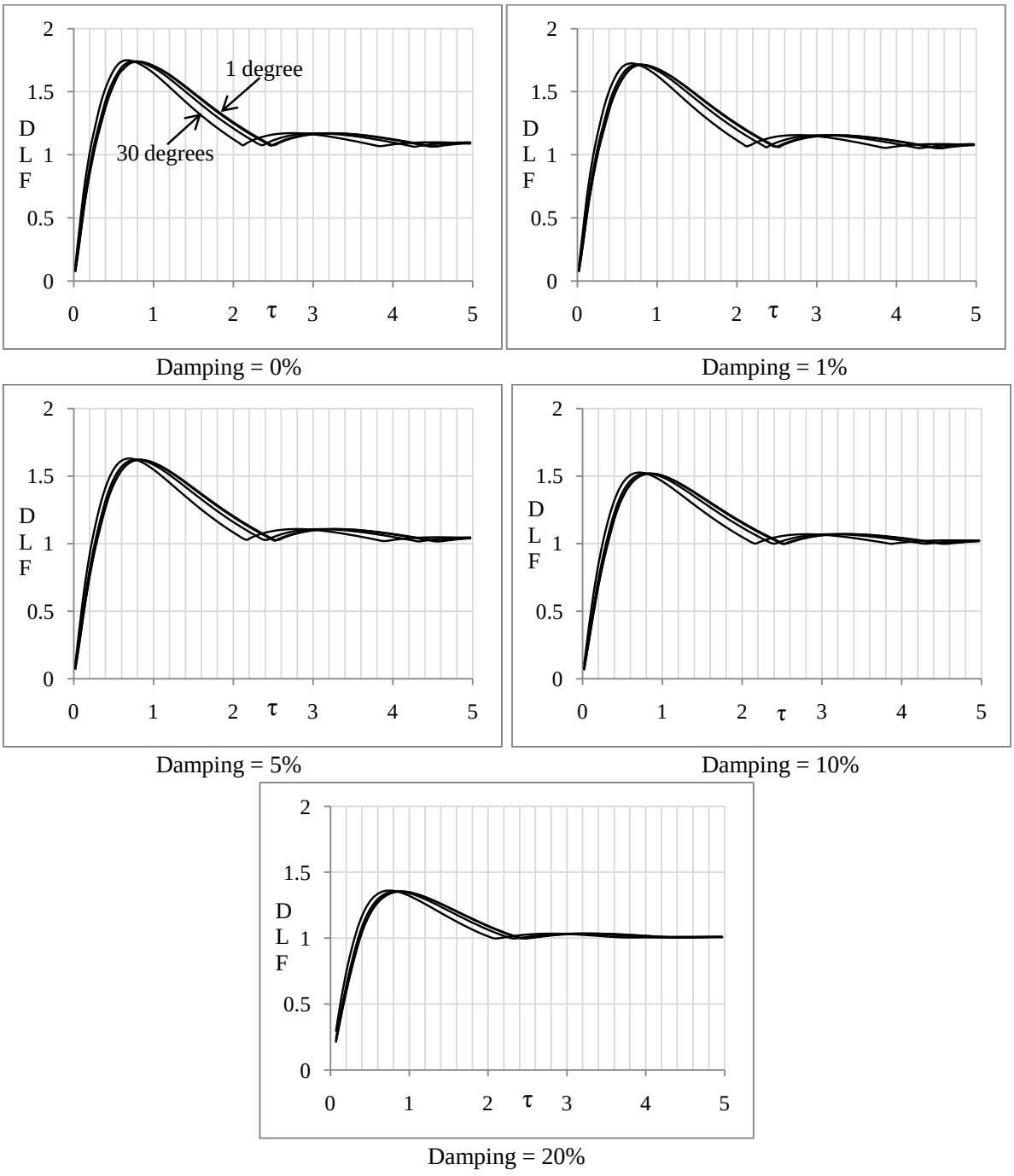

Figure 3.14: DLF for SS beam, subject to impact loading, at 5 damping ratios and 4 deadrise angles.

The behavior at $\tau = 0.2$ is interesting, with the DLF at 0.7140, i.e. the maximum dynamic deflection is only 71% of the maximum static deflection. However, the first dynamic maxima is reached after the impulse has passed over and the static deflection has subsided to almost zero. The time series shows more irregular behavior, with aperiodicity present. This occurs due to the excitation of higher order modeshapes at greater the impact speeds.

Figures 3.13 and 3.14 show the DLF of Clamped-Clamped and Simply-Supported beams respectively, at four different deadrise angles $\beta = 1$, 5, 15, and 30 degrees; and at five different damping ratios $\zeta = 0\%$, 1%, 5%, 10%, and 20%. The time-scale is non-dimensionalized with respect to the deadrise angle, and hence the DLF characteristic is almost the same for a range of deadrise angles. Between $1 < \tau < 2.5$, a smaller deadrise angle produces a greater DLF due to more severe and concentrated impact pressure. A greater deadrise angle smears and spreads the impact pressure distribution, thereby producing a slightly smaller DLF. Beyond $\tau = 2.5$, all the deadrise angles produce a quasi-static behavior.

Damping is seen to reduce the dynamic amplification and hence the maximum DLF.

3.3.2 Relative Modal Contribution.

Fig.3.15 shows the Relative Modal Contribution (RMC) contours for undamped CC and SS beams, subject to impact loading at a deadrise angle of $\beta = 1$ degree. Inclusion of the first 30 modeshapes in the normal mode analysis ensures that the RMC of the highest modeshape is less than -5 for a CC beam, and less than -6 for a SS beam; for most of the τ range. Interesting rises in the RMC contour is seen at very small τ for both the boundary conditions, when higher order modes get excited to as much as 10^{-3}

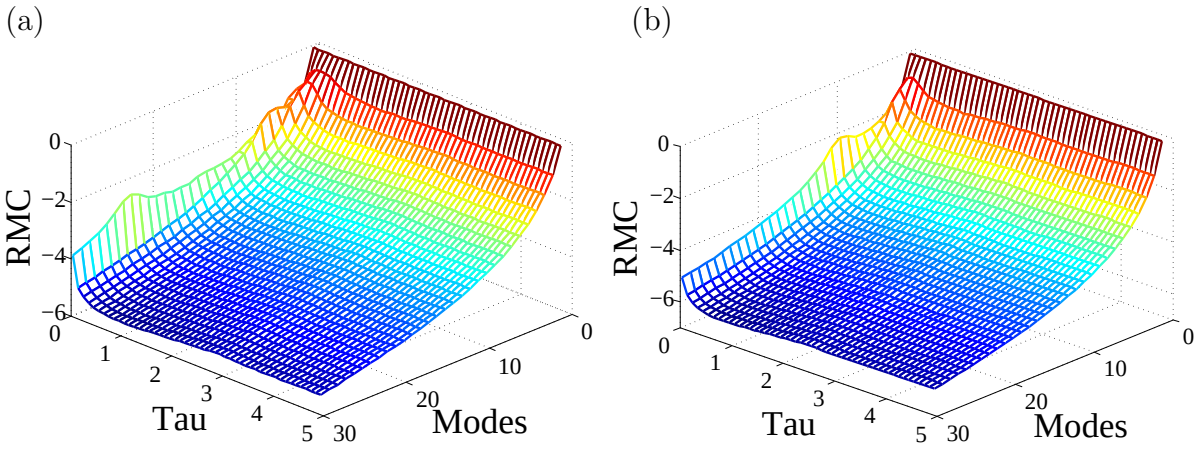

Figure 3.15: RMC at zero τ, subject to Impact loading at $\beta = 1$ degree, for (a) CC beam and (b) SS beam.

times of the fundamental modeshape. Still, the modal truncation limit of 30 is sufficient to guarantee engineering accuracy of the dynamic deflection.

3.3.3 Response at Zero Wetting time.

Fig.3.16 shows the DLF at $\tau = 0$ for CC and SS beams, for a range of deadrise angles β. The DLF asymptotes to a non-zero value for zero wetting time, for $\beta > 0$. The SS beam consistently shows a greater DLF for $\tau = 0$ than a CC beam. Statically, the beam feels the peak pressure; but dynamically, the beam feels only the keel pressure, or the pressure at $x' = 0$. The maximum static deflection under a smack force F $\approx \delta$(x,t) gives a very large static stress.

3.4 Discussion.

A hydroelastic study of an Euler-Bernoulli beam subjected to various loading con-

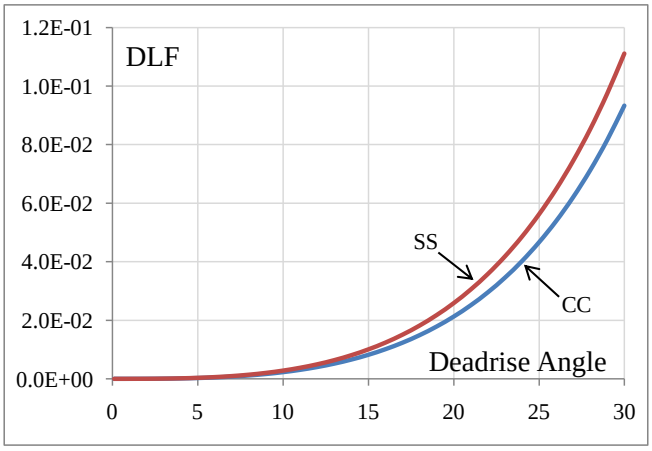

Figure 3.16: DLF at $\tau = 0$ for CC and SS beams.

ditions is presented. The primary motivation behind this work was to provide a basic interface between dynamic response to concentrated moving loads and marine slam-induced vessel vibrations. A straightforward numerical analysis of an elastic beam yields several dynamic response results and non-dimensional formulations. The dynamic response of the Euler-Bernoulli beam subjected to a uniform load sweeping across at a constant speed, is considered as a benchmark result of this investigation. Applying impact forcing as an external force on the dry beam at various deadrise angles results in typical trends of the DLF, with parameters like deadrise angle and boundary conditions causing little difference. The non-dimensionalization of the loading time (*Splash time*) by three distinct parameters, i.e. natural frequency, deadrise angle, and damping can serve as a generic vibration analyses parameter.

The non-D splash time τ serves as input to evaluate the local elastic responses of structures subjected to impact loads. For example, a 1 m bow frame of a vessel with a fundamental natural frequency of 10 Hz, slamming against the water at a vertical

velocity of 15 m/s, generates a non-dimensional splash time of 0.67. The corresponding DLF can be read from Fig.3.7 and Fig.3.8, where the impact pressure is modelled as a uniform stretching load. At large deadrise angles ($\beta > 20$ degrees), the pressure configuration is almost like a uniform stretching load. The maximum DLF in response to the uniform load is around 2.00, while that in response to the impact loading is around 1.70. Thus the uniform stretching load can be considered as an upper limit of the impact loading, from the perspective of response analyses. The DLF for high speed crafts subjected to impact loading would be better estimated from Fig.3.13 and Fig.3.14, since they have lower deadrise angles and operate widely under different operational and environmental conditions.

The choice of the definition of the DLF is based on returning a complete maximum dynamic response corresponding to the equivalent maximum static response. The evaluation of the configuration of the dynamic deflection in space and time need not be a part of the already long design procedure.

Ward [27] investigated the impact stresses on the bow of a sailboat, assuming a constant stretching load, whose magnitude remains a constant during the forcing (thereby reducing the peak pressure like a rectangular hyperbola px = P_0 sweeping across the plate, where p is the force per unit length, P_0 is the total pressure magnitude, and x is the wetted length). He predicted the quasi-static response well (DLF ≈ 1), but generated a very small DLF ($< 20\%$ of the static deflection) at very large impact speeds. The latter is true for the Impact loading model, but not for a Uniform load model, where the DLF approached 2 for very high impact speeds. Also, the peak DLF is estimated to be approximately 1.5, which is nearly the same as the peak DLF in the impact load response studied here. The crude representation of the impact force model with a uni-

form load model hampers the interpretation of the results with respect to the physics of the impact.

The dry vibration assumes that the maximum structural response (hence the maximum stresses and strains) occurs early in the impact sequence, with most of the beam dry. Thus, the impact forcing can be considered as an external loading on a dry beam. In the other limit, the completely wet vibration assumes that the maximum structural response occurs later in the impact sequence, when the beam is completely submerged. Now, the impact forcing gets augmented by a radiation pressure, which is the inertia of the fluid set into motion by the beam. This completely wet vibration condition is the subject of Chapter 5.

The impact-induced local hull vibrations involve complicated hydrodynamics, with the maximum response occurring with the beam nearly halfway into the water. Local changes in the structure geometry, stiffness, deadrise angle further complicate the response and its analysis. The impact forcing model would also be affected by the wet chines. A probabilistic analysis in various sea states with forward vessel speed can, in fact, generate the slamming spectrum and the slam-induced flexural response spectra for both long-crested and short-crested seas.

CHAPTER IV

DRY VIBRATION OF KIRCHHOFF PLATE

This chapter examines the vibration characteristics of a dry Kirchhoff's plate, subject to transient loads using one-way coupling between the fluid and the structure, and the numerically efficient normal mode analysis. The natural frequencies and modeshapes for a very large number of modes can be generated for the free vibration. Admissible functions, satisfying the boundary conditions, have been used to generate the plate modeshapes, and the corresponding natural frequencies. Modal analysis generates the coupled system of non-homogeneous modal dynamic governing differential equations, which are solved by stable numerical time-integration. The superposition of the modal dynamic deflections gives the total dynamic deflection $Z(x,y,t)$.

The ratio of the largest $Z(x,y,t)$ to the largest $Z_{st}(x,y,t)$ is defined as the dynamic load factor (DLF). First, the DLF in response to a uniform unit stretching load is established followed by the DLF in response to an impact load under different deadrise angles β. The behavior of the structure is qualitatively dynamic or quasi-static, with DLF varying between the range of 0 and 2, for a range of impact speeds of the moving load.

To determine modal truncation guidelines, the modal contributions with respect to the dominant fundamental mode are studied for different impact speeds V and deadrise angles β. Inclusion of a greater number of modes increases the numerical accuracy, but also increases computational time. Those higher-order modes which contribute negligibly in comparison to the fundamental modeshape are ignored in order to optimize the

trade-off between the analysis accuracy and computational efficiency.

4.1 Free dry vibration of plates.

The free vibration (*Eigen Value*) analysis of the square plate (Fig.4.1), with Galerkin's method; having different end conditions; yields the natural frequencies ω_k (*Eigenvalues*) and the modeshapes $\Phi_k(x, y)$ (*Eigenvectors*). The details have been given in Appendix 3. The Eigen value analysis, of the homogeneous system of equations of free vibration, gives the Eigen values $-\omega^2$ (*natural frequencies*) and the A^k_{jl}. The k^{th} natural frequency has one dominant associated modeshape, as well as lesser contributions from the others, whose amplitudes are given by A^k_{jl} (Leissa [36]).

The amplitudes are non-dimensionalized by the largest A^k_{jl} for a given Eigen value. The natural frequency is non-dimensionalized by the geometric and material properties, i.e. the length of the plate L, the mass per unit area of the plate m, and the stiffness of the plate D.

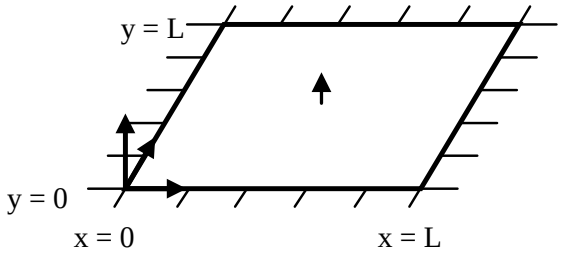

Figure 4.1: Kirchhoff's plate.

The non-dimensional plate frequency (*Non-D* ω) is defined as $\omega_k\sqrt{\frac{D}{mL^4}}$, where $D = \frac{Eh^3}{12(1-\nu^2)}$. They are tabulated below, after verification with respect to existing values, namely, Leissa [36] (Non-D $\omega_1 = 35.98$) and Young[35] (Non-D $\omega_1 = 35.99$). The nu-

merical convergence of the frequencies has been studied with an Eigen analysis of 30x30 = 900 modeshapes.

Modes	1 x 1	3 x 3	5 x 5	10 x 10	20 x 20	30 x 30
Freq	36.10867	36.00676	35.99149	35.98623	35.98525	35.98520

Table 4.1 Convergence of the CCCC plate fundamental frequency up to 5 significant figures, with higher modal truncation limits.

Consider a two degree-of-freedom (2-DOF) system, vibrating freely. The Eigen values analysis of the system of governing equations of free vibration gives the Eigen Values (λ) and the Eigen Vectors. The characteristic equation is a quadratic in λ, given as $a\lambda^2 + b\lambda + c = 0$, where a, b, and c are real, arbitrary constants. The discriminant of the equation is $D = \frac{\sqrt{b^2-4ac}}{2a}$. The nature of the two roots λ_1 and λ_2 given by the value of D is as follows:

(1) D = 0 $\rightarrow$ the roots are *real* and *equal*, e.g, $\lambda^2 - 2\lambda + 1 = 0$ gives λ_1, $\lambda_2 = 1$.

(2) $D > 0$ and a perfect square $\rightarrow$ the roots are *real*, *rational* and *unequal*, e.g, $\lambda^2 + 5\lambda + 4 = 0$ gives λ_1 = -1, λ_2 = -4.

(3) $D > 0$ and a not perfect square $\rightarrow$ the roots are *real*, *irrational* and *unequal*, occurring as surd pairs, e.g, $\lambda^2 + 4\lambda + 1 = 0$ gives $\lambda_1 = -2+\sqrt{3}$, $\lambda_2 = -2-\sqrt{3}$.

(4) $D < 0 \rightarrow$ the roots are *complex* and *unequal*, occurring as complex conjugate pairs, e.g, $\lambda^2 + \lambda + 1 = 0$ gives $\lambda_1 = \frac{-1+i\sqrt{3}}{2}$, $\lambda_2 = \frac{-1-i\sqrt{3}}{2}$.

(5) b = 0 $\rightarrow$ the roots are *purely imaginary*, occurring as complex conjugate pairs, e.g, $\lambda^2 + 2 = 0$ gives $\lambda_1 = i\sqrt{2}$, $\lambda_2 = -i\sqrt{2}$.

Framing of the Eigen value problem of free vibration of the plate, involving 10x10 modeshapes, generates the characteristic equation of the order of λ^{100}. Thus the equation

has 100 roots, some of which are unique and some occur in pairs. The details have been explained in Appendix 3.

4.1.1 Frequencies

Table 4.1 gives the first 5(five) significant figures of the fundamental natural frequency for the 30x30 = 900 modeshapes. Inclusion of more and more modeshapes leads to increased accuracy of higher and higher frequencies. The 30x30 = 900 analysis converges the 100^{th} frequency to 4 significant figures. For higher convergence of the same, a 40x40 = 1600 analysis might be necessary.

There are three(3) kinds of frequencies of a CCCC /SSSS plate.

Type(a) ***Unique*** *frequencies* : when $j = l$.

Type(b) *Repeated frequencies* ($j \neq l$) or ***Identical*** *twins*: when j is odd and l is even, or vice-versa. Their modeshapes occur in pairs, i.e. they are identical, only rotated in space by 90 degrees.

Type(c) *Non-repeated but very close frequencies* ($j \neq l$) or ***Fraternal*** *twins* : when j and l are both odd, or both even. Their modeshapes are very different from each other. These frequencies occur when the contributing beam modeshape(s) and its(their) curvature(s) are not orthogonal to each other.

The three kinds of frequencies occurs for CCCC plates. The SSSS plate has either unique or repeated frequencies, since its contributing beam modeshapes and their curvatures are orthogonal to each other. For a CSCS plate, *all* the frequencies are unique.

Table 4.2 contains the first 7x7 = 49 non-dimensional natural frequencies of the various boundary conditions and converged to five significant figures. It contains the following components for the three different boundary conditions.

k = Plate modeshape index, listed in the ascending order of the frequency magnitudes.

j = Dominant beam modeshape index in the X-direction.

l = Dominant beam modeshape index in the Y-direction.

Non-D ω = non-dimensional natural frequency of the plate, accurate for 5 significant figures.

As an example, j = 3 and l = 5 signifies A^k_{35} is the largest amplitude in the series summation of $\Phi_k(x, y)$.

4.1.2 Modeshapes

Table 4.3 gives the first 7x7 = 49 modeshapes (Φ^k_{jl}) of a CCCC plate. The diagonal of the table contains the Unique (*Type a*) frequencies, in which we find the *chessboard-like* deflection configuration. The diagonals on either side of the main diagonal contains the repeated frequencies (*Type b*) frequencies. The diagonals adjacent to them contains the non-repeated (*Type c*) frequencies. The *Type b* and *Type c* frequencies appear alternately in the outer sub-diagonals.

Table 4.4 contains the A^k_{jl} for the first six modeshapes. For k = 1, The contributing modehapes are $A_{11} = 1$, $A_{13} = A_{31} = 0.014$, $A_{33} = 0.003$, and so on. The odd beam modeshapes $\phi_j(x)$ and $\phi_l(y)$ contribute the most, while the even beam modeshapes contribute the least. e.g. $A_{22} = O(10^{-14})$. A_{11} and A_{44} matrices are exactly symmetrical. For k = 2 and 3 modes, A_{12} and A_{21} contribute almost equally. The A^2_{jl} and A^3_{jl} matrices are nearly transposes of each other; each producing *bilaterally symmetrical* modeshapes. Similarly, for k = 5 and 6, A_{13} and A_{31} contribute equally. However, A^5_{jl} is skew-symmetric, while A^6_{jl} is symmetric; each generating *radially symmetrical* modeshapes.

	CCCC			SSSS			CSCS		
k	**j**	**l**	**NonD ω**	**j**	**l**	**NonD ω**	**j (CC)**	**l (SS)**	**NonD ω**
1	1	1	35.985	1	1	19.739	1	1	28.951
2	1	2	73.393	1	2	49.348	1	2	54.743
3	2	1	73.393	2	1	49.348	2	1	69.327
4	2	2	108.21	2	2	78.957	2	2	94.585
5	3	1	131.58	3	1	98.696	1	3	102.22
6	1	3	132.20	1	3	98.696	3	1	129.10
7	3	2	165.00	3	2	128.30	2	3	140.20
8	2	3	165.00	2	3	128.30	3	2	154.78
9	1	4	210.52	1	4	167.78	1	4	170.35
10	4	1	210.52	4	1	167.78	3	3	199.81
11	3	3	220.03	3	3	177.65	2	4	206.70
12	4	2	242.15	4	2	197.39	4	1	208.39
13	2	4	243.14	2	4	197.39	4	2	234.59
14	3	4	296.33	3	4	246.74	1	5	258.61
15	4	3	296.33	4	3	246.74	3	4	265.20
16	1	5	308.97	1	5	256.61	4	3	279.65
17	5	1	309.23	5	1	256.61	2	5	293.76
18	5	2	340.66	5	2	286.22	5	1	307.39
19	2	5	340.66	2	5	286.22	5	2	334.03
20	4	4	371.34	4	4	315.83	4	4	344.54
21	3	5	392.86	3	5	335.57	3	5	351.12
22	5	3	394.00	5	3	335.57	1	6	366.82
23	1	6	427.35	1	6	365.18	5	3	379.36
24	6	1	427.35	6	1	365.18	2	6	401.08
25	6	2	458.22	6	2	394.78	6	1	425.91
26	2	6	458.81	2	6	394.78	4	5	429.68
27	4	5	467.38	4	5	404.65	5	4	444.15
28	5	4	467.38	5	4	404.65	6	2	452.91
29	3	6	510.64	3	6	444.13	3	6	457.45
30	6	3	510.64	6	3	444.13	1	7	494.87
31	5	5	562.41	5	5	493.48	6	3	498.53
32	1	7	565.38	1	7	493.48	2	7	528.48
33	7	1	565.54	7	1	493.48	5	5	528.89
34	6	4	583.13	6	4	513.22	4	6	535.17
35	4	6	584.33	4	6	513.22	6	4	563.38
36	2	7	596.36	2	7	523.09	7	1	564.21
37	7	2	596.36	7	2	523.09	3	7	584.02
38	7	3	647.61	7	3	572.44	7	2	591.50
39	3	7	648.42	3	7	572.44	5	6	633.81
40	5	6	677.89	5	6	602.05	7	3	637.42
41	6	5	677.89	6	5	602.05	6	5	647.93
42	4	7	720.47	4	7	641.52	4	7	660.95
43	7	4	720.47	7	4	641.52	7	4	702.45
44	6	6	792.45	6	6	710.61	6	6	752.47
45	5	7	813.33	5	7	730.35	5	7	758.97
46	7	5	814.56	7	5	730.35	7	5	786.99
47	7	6	927.68	7	6	838.92	6	7	877.11
48	6	7	927.68	6	7	838.92	7	6	891.34
49	7	7	1062.2	7	7	967.22	7	7	1015.7

Table 4.2 First 7x7 natural frequencies of a square CCCC, SSSS and CSCS plate.

j → / l ↓	1	2	3	4	5	6	7
1	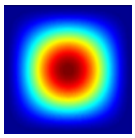	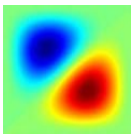	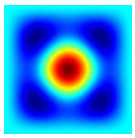	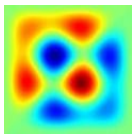	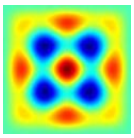	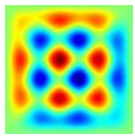	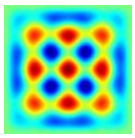
2	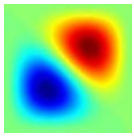	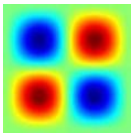	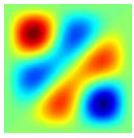	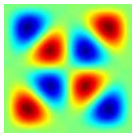	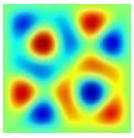	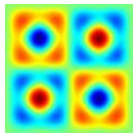	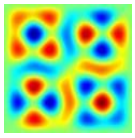
3	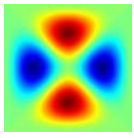	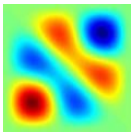	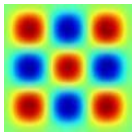	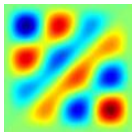	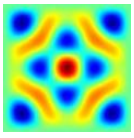	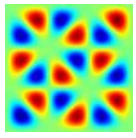	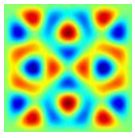
4	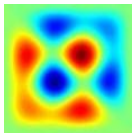	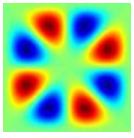	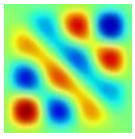	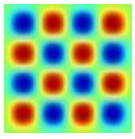	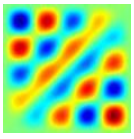	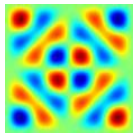	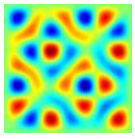
5	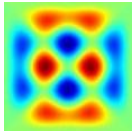	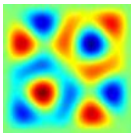	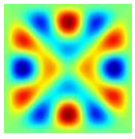	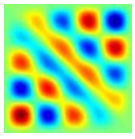	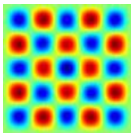	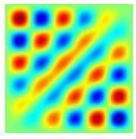	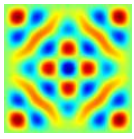
6	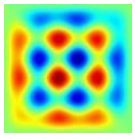	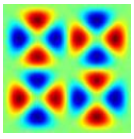	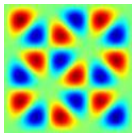	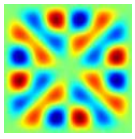	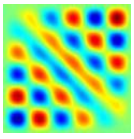	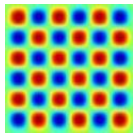	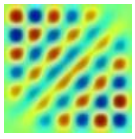
7	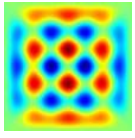	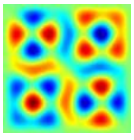	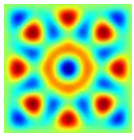	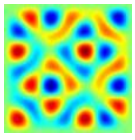	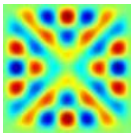	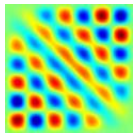	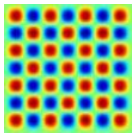

Table 4.3 First 7x7 modeshapes of a square CCCC plate.

k = 1

Modes x y	***1***	***2***	***3***	***4***	***5***
1	1	-1.5E-08	0.01421	-1E-07	0.001994
2	-1.5E-08	2.95E-14	6.06E-09	-3.1E-14	1.25E-09
3	0.01421	6.06E-09	-0.00315	4.52E-08	-0.00097
4	-1E-07	-3.1E-14	4.52E-08	-6.8E-13	1.76E-08
5	0.001994	1.25E-09	-0.00097	1.76E-08	-0.00045

k = 2

Modes x y	***1***	***2***	***3***	***4***	***5***
1	-2.5E-08	-1	6.33E-09	-0.01011	1.83E-07
2	-0.97973	2.03E-07	-0.04007	3.68E-07	-0.0069
3	5.92E-09	-0.0409	-1.1E-08	0.002312	-4E-08
4	-0.0099	3.76E-07	0.002265	-1E-07	0.001156
5	1.8E-07	-0.00704	-3.9E-08	0.00118	-4.7E-08

k = 3

Modes x y	***1***	***2***	***3***	***4***	***5***
1	1.12E-09	-0.91154	1.9E-08	-0.00921	1.69E-07
2	1	-9.1E-09	0.040896	-3.9E-07	0.007038
3	-2E-08	-0.03728	4.72E-10	0.002108	-3.2E-08
4	0.010106	3.55E-07	-0.00231	4.65E-09	-0.00118
5	-1.9E-07	-0.00642	3.56E-08	0.001075	2.09E-09

Table 4.4 A_{jl}^{k} for the first six frequencies of square plates.

k = 4

Modes x / y	***1***	***2***	***3***	***4***	***5***
1	1.6E-14	-8.5E-08	4.59E-12	-8.9E-09	1.67E-13
2	-8.5E-08	-1	9.04E-08	-0.03278	5.95E-07
3	-5.4E-12	9.04E-08	-4.4E-14	-5.3E-09	2.89E-14
4	-8.9E-09	-0.03278	-5.3E-09	0.00206	-2.5E-08
5	9.81E-14	5.95E-07	1.65E-13	-2.5E-08	1.13E-13

k = 5

Modes x / y	***1***	***2***	***3***	***4***	***5***
1	-3.1E-13	-2.7E-08	-1	7.06E-07	-0.00856
2	2.73E-08	-5.8E-12	3.19E-07	-3.5E-13	1.48E-09
3	1	-3.2E-07	1.49E-12	-8.5E-07	0.014542
4	-7.1E-07	4.07E-15	8.47E-07	2.09E-14	-2.5E-09
5	0.008559	-1.5E-09	-0.01454	2.54E-09	-8E-14

k = 6

Modes x / y	***1***	***2***	***3***	***4***	***5***
1	0.028015	-1.8E-08	-1	4.71E-07	-0.00541
2	-1.8E-08	6.18E-14	2.47E-07	6.49E-13	-9.8E-09
3	-1	2.47E-07	-0.12846	7.26E-07	-0.01199
4	4.71E-07	6.59E-13	7.26E-07	4.04E-12	-8.6E-08
5	-0.00541	-9.8E-09	-0.01199	-8.6E-08	0.002117

Table 4.4 A_{jl}^{k} for the first six frequencies of square plates.

4.2 Dynamic response of plates to uniform stretching load.

A unit load stretches across the plate of length L at a speed of V. The plate is set into small-amplitude flexural vibrations, which are analyzed by the modal analysis methodology. The dynamic load factor (DLF) is plotted against the non-dimensionalized wetting time

$$\tau = \frac{L}{V}\frac{\omega_{1,dry}}{2\pi}\sqrt{1-\zeta^2}, \tag{4.1}$$

for the four different boundary conditions of the Kirchhoff's plate, and four different damping ratios.

4.2.1 Dynamic Loading Factor.

Fig.4.2 shows the DLF results of a *square* Kirchhoff's plate, subject to transient uniform loading over a wide range of impact velocities. For $\tau > 2$, the dynamic behavior of the plate is restricted to 0%-5% of the static response. With decreasing τ, the DLF steadily and steeply rises to a little over 2.00 for undamped vibration. Damping reduces the peak DLF and also smoothens the DLF characteristic in the quasi-static zone.

Interestingly, the CCCC and the CSCS plate behave similarly except for very small τ. Similarly, the DLFs of the SSSS and SCSC plate superimpose over each other except very small τ. This highlights the fact that the beam modeshape *parallel* to the direction of the forcing (x-direction here) is a major factor influencing the dynamic behavior. The beam modeshape (i.e. boundary conditions on $y = 0$ an $y = L$) perpendicular to the forcing direction (y-direction here) has little or no influence on the nature of the DLF.

Also, the CSCS and SCSC DLFs deviate from the CCCC and SSSS DLFs respectively, and approach *each other* at very low τ values, showing that the orientation of

the forcing becomes insignificant at very high impact speeds. For a damping of 5%, the maximum DLF asymptotes to an average of 1.89. For a damping of 10%, the maximum DLF asymptotes to an average of 1.76.

Fig.4.3 shows the time series of the dynamic and static deflection of the midpoint of the plate, at $\tau = 1.0$ and 0.5. At larger values of τ (Fig.4.3a), when the fundamental plate modeshape is the prime contributor, the dynamic deflection time-series is periodic. Thus a short record length, including only one dynamic peak in the time series, is sufficient to calculate the global DLF at that τ. This reduces the computation time, since the time-integration is required for a limited number of time steps, enough to include one fundamental time-period of the plate.

Reducing the τ (Fig.4.3b) cause the higher order modeshapes to participate in the deflection, leading to aperiodicity in the time-series, as seen in Fig.4.3b. At such wetting speeds, the DLF becomes a function of the record length, explaining the *erratic* behavior of the DLF characteristic for $\tau < 0.4$ in Fig.4.2. Elaborating, Fig.4.3b shows that the first dynamic peak is less than the second in the time series. A record length of a *single* fundamental period would return a lower value of DLF than a record length of *two* fundamental periods. This aperiodicity becomes more and more pronounced for smaller and smaller τ, due to the increased presence of the higher order modes, causing an ambiguity in the accuracy of the DLF, and leading to rough DLF characteristics.

However, this uncertainty is present only for undamped vibration. Damping causes the vibration to decay with time, with the higher modes damped faster than the first mode; typically giving the first dynamic peak as the *global* maximum in the time series, irrespective of the record length. This is clearly seen in Fig.4.2b, where the DLF characteristics for all the four boundary conditions are smooth even for very small τ.

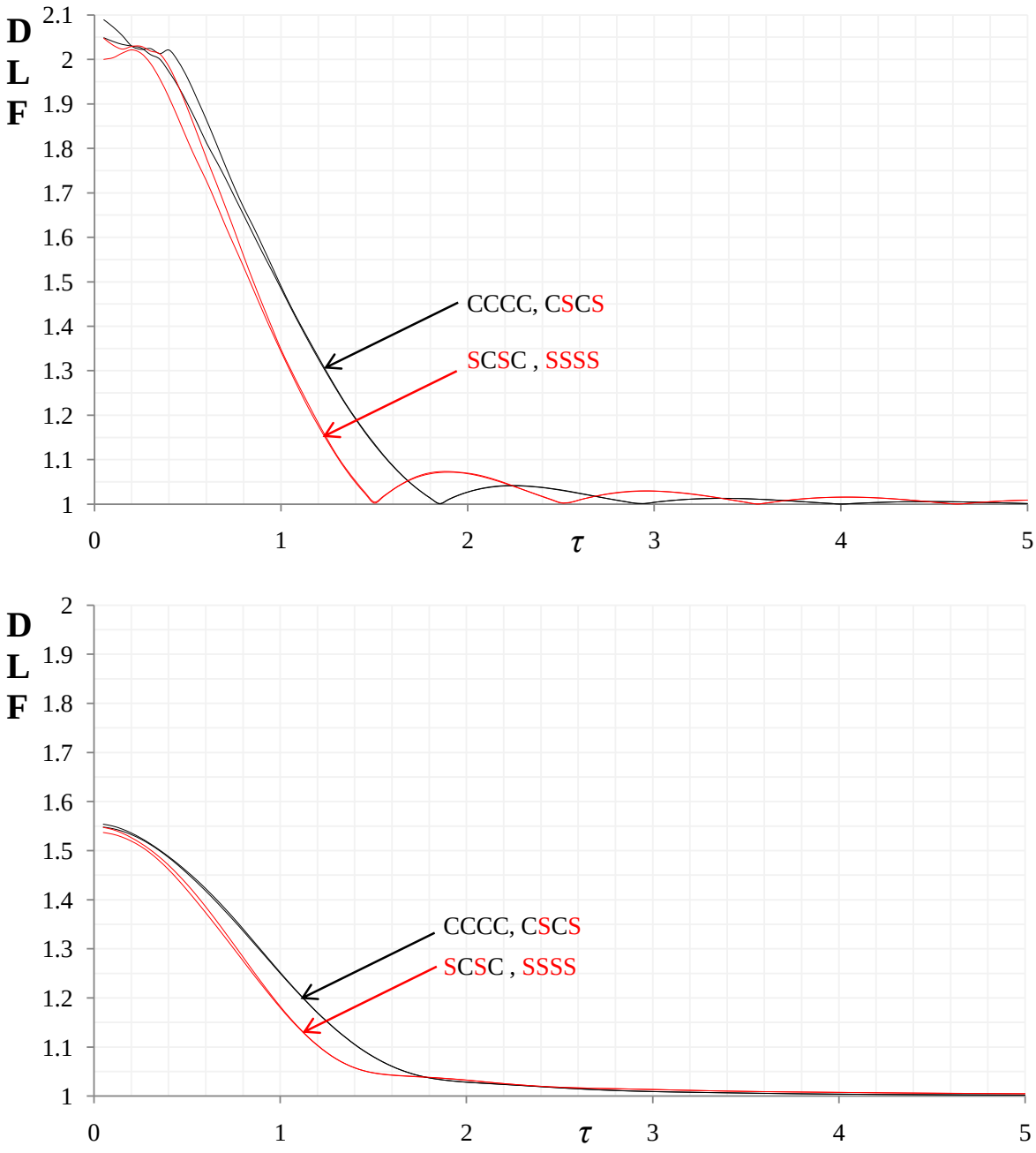

Figure 4.2: DLF for uniform loading for plates for four(4) boundary conditions, ζ = (a) 0%, (b) 20%.

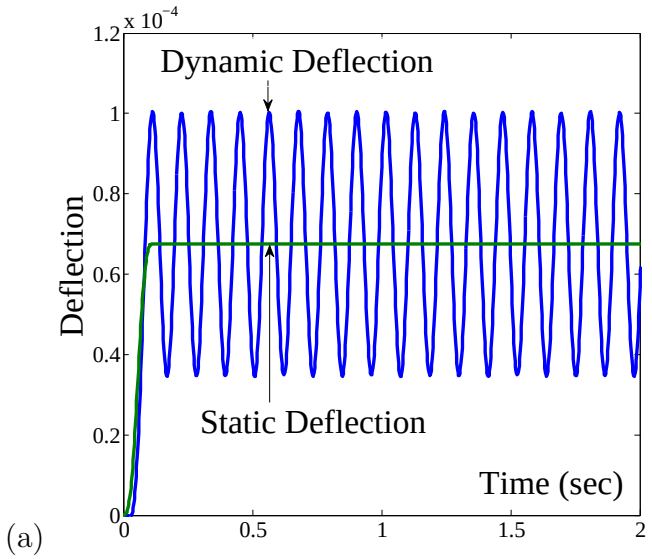

(a)

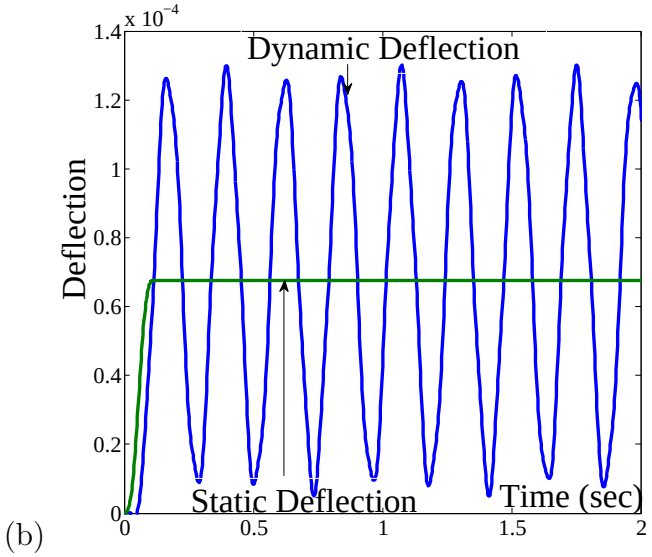

(b)

Figure 4.3: DLF as a function of the record length, for $\tau =$ (a) 1.0, (a) 0.50.

4.2.2 Relative Modal Contribution.

The modal truncation is set at 15x15 = 225 modeshapes, since the highest modeshapes have R.M.C. < -3, i.e. the contribution of the highest modeshape in this limit is 10^{-3} times that of the fundamental modeshape. At high values of τ (> 3), the plate

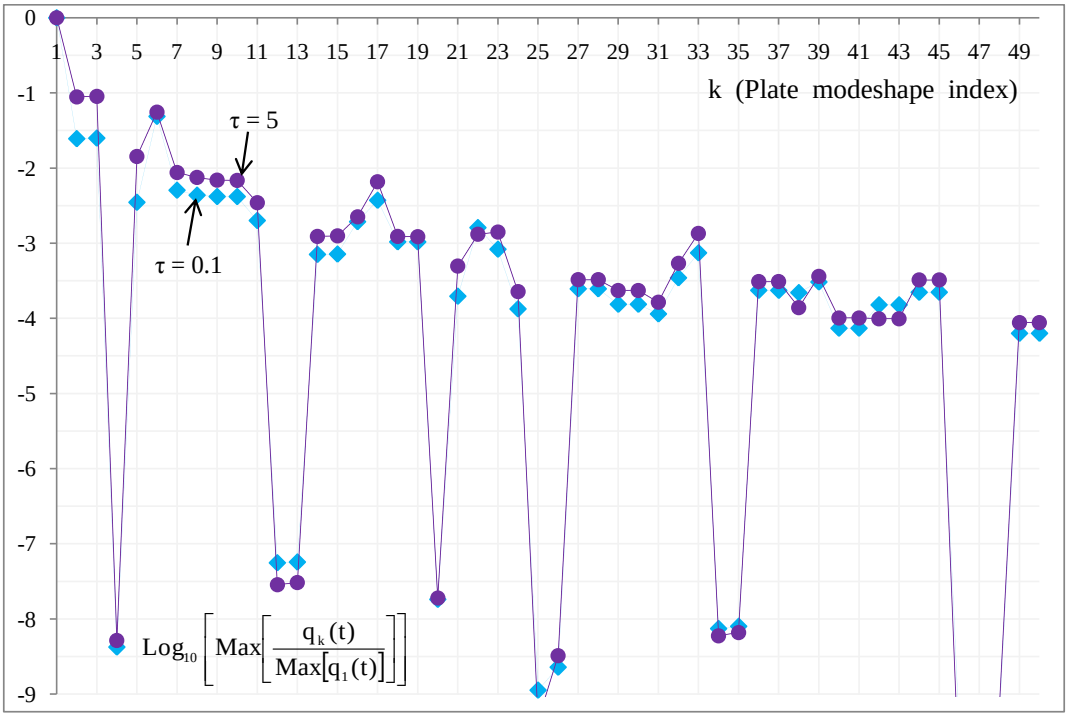

Figure 4.4: RMC of a CCCC plate subject to uniform loading at $\tau = 0.1$, 5.0.

behaves quasi-statically, with the DLF nearly 1. For smaller values of τ, there is a more pronounced dynamic behavior. Fig.4.4 illustrates the comparative RMC, of a CCCC plate, subject to uniform loading, for the strongly dynamic response ($\tau = 0.1$) and the quasi-static response ($\tau = 5.0$). The behavior at $\tau = 5.0$ shows a marginally greater RMC for nearly all the higher order plate modeshapes than the behavior at $\tau = 0.1$.

Since the load is uniformly distributed in both directions, the odd beam modeshapes

contribute significantly, and the even beam modeshapes have very little contribution. As seen below, the modeshapes with indices k = **4** (j = 2, l = 2), **12** (j = 4, l = 2), **13** (j = 2, l = 4) and **20** (j = 4, l = 4), have very little contribution $O(\ 10^{-8})$ compared to the fundamental modeshape. However, they are not exactly zero, since the static coupling of the stiffness matrix causes the principal coordinate $q_k(t)$ to be non-zero, even though the corresponding generalized forcing is zero. Also, the repeated frequencies (*Type b* frequencies) have equal contribution and RMC. E.g. both the modeshapes k = **2** (j = 1, l = 2) and k = **3** (j = 2, l = 1) have the same RMC at a given τ. But, k = **5** (j = 3, l = 1) and k = **6** (j = 1, l = 3), having very close frequencies (*Type c* frequencies) but very different modeshapes, show close but unequal RMC.

4.2.3 Response at zero wetting time.

Boundary conditions	**CCCC**	**SSSS**	**CSCS**	**SCSC**
Damp = 0%	2.0939	2.0000	2.0528	2.0528
Damp = 5%	1.9154	1.8633	1.8941	1.8941
Damp = 10%	1.7730	1.7413	1.7611	1.7611
Damp = 20%	1.5530	1.5382	1.5486	1.5486

Table 4.5 DLF at zero wetting time for 4 boundary conditions and 4 ζ's.

For zero wetting time, the uniform load acts over the whole of the plate from time $t = 0$ onwards. Table 4.5 above shows that the DLF at zero wetting time is same for CSCS and SCSC orientations up to the first 5 significant figures. This also stands for the response of an extremely soft or an infinitely massive structure. The CCCC plate has a higher DLF than the SSSS plate, since the former has more spatial curvature than the latter, and thus produces a greater dynamic amplification.

4.2.4 Generalization of the time-scale by the wave number of the beam modeshapes.

This exercise is done to generalize the DLF of the plates of different boundary conditions as far as possible, for the convenience of the structural designer. The plate modeshapes $\Phi_k(x, y)$ are a weighted sum of the product of the beam modeshapes in the x and y directions, as reiterated below.

$$\Phi_k(x, y) = \Sigma_{j=1}^{modex} \Sigma_{l=1}^{modey} A_{jl}^k \phi_j(x) \phi_l(y) = \Sigma_{j=1}^{modex} \Sigma_{l=1}^{modey} A_{jl}^k G_{jl}(x, y).$$

However, it is the beam modeshape (dependent on the end conditions), *parallel* to the direction of the forcing, $\phi_j(x)$, which strongly influences the DLF characteristic. The perpendicular modeshape, $\phi_l(y)$, has significantly less influence of the nature of the DLF. For this, we first revisit the beam vibration problem.

The undamped free vibration of an Euler-Bernoulli beam has the following linear, homogeneous, second order, governing differential equation :

$$m(x)\frac{\partial^2 z(x,t)}{\partial t^2} + EI(x)\frac{\partial^4 z(x,t)}{\partial x^4} = 0.$$

The dependent unknown 2-D dynamic deflection $Z(x,t)$ is a function of x and t. Separation of variables leads to : $Z(x,t) = \mathrm{G}(x)F(t)$. Thus

$$\frac{\ddot{F}(t)}{F(t)} = \frac{EI(x)}{m(x)}\frac{G^{IV}(x)}{G(x)} = -\omega^2,$$

where ω is the separation constant, which generates two independent equations. The principal coordinates are generated by $\ddot{F}(t) + \omega^2 F(t) = 0$, and the beam modeshapes are generated by $G^{IV}(x) = \frac{m(x)\omega^2}{EI(x)}G(x)$. Replacing $\gamma_j^4 = \frac{m(x)\omega_j^2}{EI(x)}$, the general solution to the beam modeshape is :

$\phi_j(x) = A1_j cos(\gamma_j x) + A2_j sin(\gamma_j x) + A3_j cosh(\gamma_j x) + A4_j sinh(\gamma_j x)$. The four constants, A1, A2, A3 and A4 are calculated from the end conditions. γ_j is the wave number of the j^{th} beam vibration modeshape.

(a) The Clamped-Clamped (CC) beam has zero deflection and zero slope at the ends. Thus the modeshape is $\phi_j(x) = cos(\gamma_j x) - cosh(\gamma_j x) - \sigma_j sin(\gamma_j x) + \sigma_j sinh(\gamma_j x)$; with the fundamental wave number $\gamma_{CC} = 4.7300$. Here, $\sigma_j = \frac{cos(\gamma_j L) - cosh(\gamma_j L)}{sin(\gamma_j L) - sinh(\gamma_j L)}$. The generalization of the time-scale with respect to the clamped-clamped (CC) beam wave number is done as

$$\tau_{CC} = \left(\frac{L}{V}\right) \frac{\omega_1}{2\pi} \sqrt{1-\zeta^2} \sqrt{\frac{4.73}{\gamma_n}}, \tag{4.2}$$

with n = 1,2,3,4. Here, $\gamma_{1,2} = 4.73$ for the CCCC and CSCS plates; and $\gamma_{3,4} = \pi$ for the SSSS and SCSC plates.

(b) The Simply-Supported (SS) beam has zero deflection and zero bending moment at the ends. Thus the modeshape is $\phi_j(x) = sin(\gamma_j x)$; with the fundamental wave number $\gamma_{SS} = \pi$. The generalization of the time-scale with respect to the simply-supported (SS) beam wave number is done as

$$\tau_{SS} = \left(\frac{L}{V}\right) \frac{\omega_1}{2\pi} \sqrt{1-\zeta^2} \sqrt{\frac{\pi}{\gamma_n}}, \tag{4.3}$$

with n = 1,2,3,4. Here, $\gamma_{1,2} = 4.73$ for the CCCC and CSCS plates; and $\gamma_{3,4} = \pi$ for the SSSS and SCSC plates.

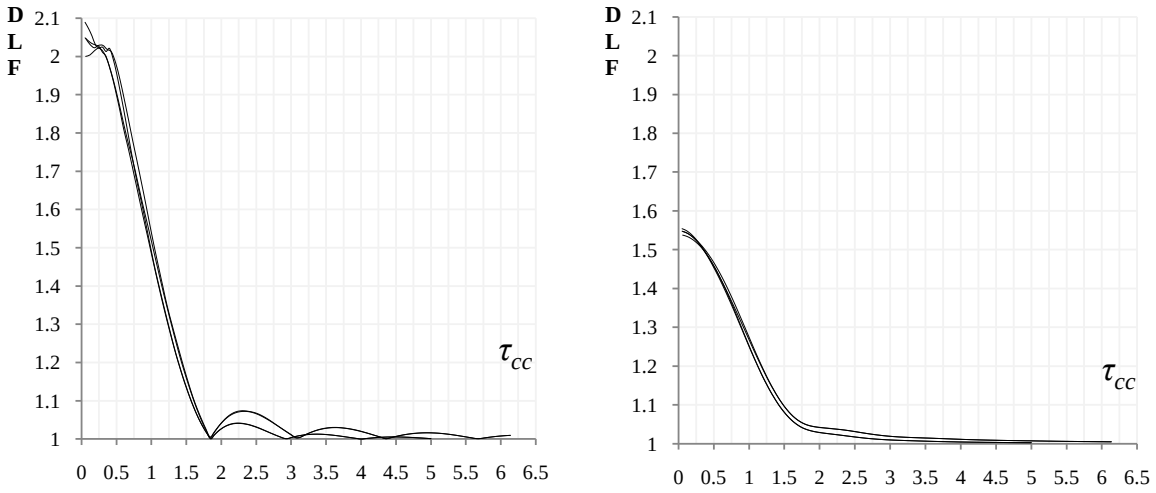

DLF for uniform loading for plates for four(4) BCs generalized w.r.t. CC wave number, with ζ = (a) 0%, (b) 20%.

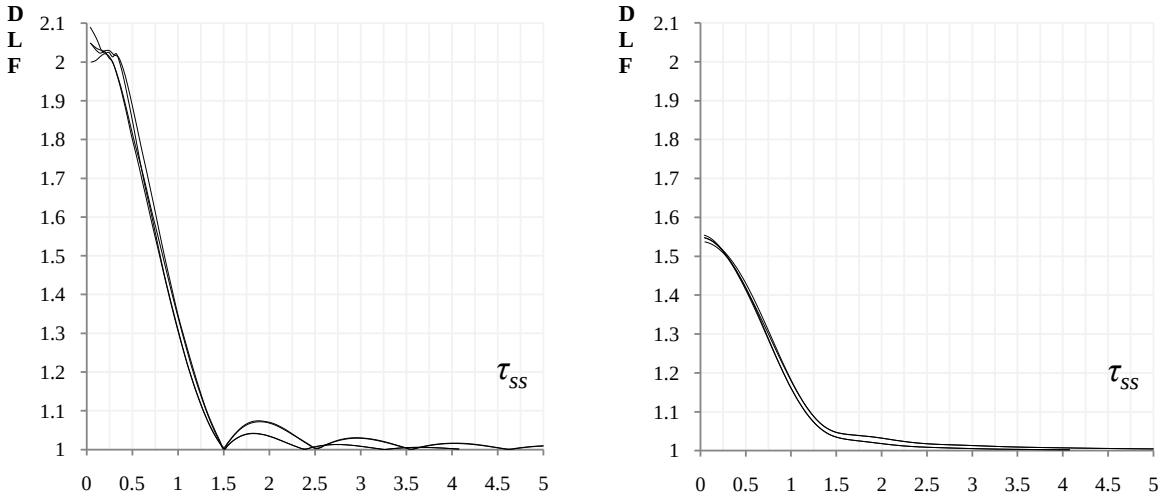

DLF for uniform loading for plates for four(4) BCs generalized w.r.t. SS wave number, with ζ = (a) 0%, (b) 20%.

Figure 4.5: Uniform Load DLF generalized to the beam wave numbers.

This modifies the time-scale such that the DLFs for all the four plate boundary conditions (CCCC, SSSS, CSCS and SCSC) are similar within the region of practical interest of the structural designer, i.e. $0.5 < \tau < 2$. The self-similar behavior becomes more and more pronounced for higher and higher damping. For a liberal damping ratio of 20%, it is seen that a single DLF characteristic represents the response of the plate with *all* the four boundary conditions, in both the modified time-scales (Fig.4.5). It also shows that the *first* quasi-static behavior (DLF = 1), for all the four boundary conditions, occurs at $\tau_{CC} = 1.85$ (Eq.(4.2)) and $\tau_{SS} = 1.50$.(Eq.(4.3))

4.3 Dynamic response of plates to impact load.

The response of the Kirchhoff's plate to the uniform stretching load helps establish the benchmarks of the modal analysis, namely the time-scales, the DLF, and the RMC for square plates. Now we proceed to a more realistic model of the impact force distribution, defined by a moving jet head, stretching from the keel upwards. The maximum pressure is a function of the vertical impact velocity V and the deadrise angle β.

4.3.1 Dynamic Loading Factor.

The Dynamic Load Factor (DLF) characteristics for a square Kirchhoff's plate subject to impact loading at four deadrise angles, i.e. 1, 5, 15 and 30 degrees, is shown below (Fig.4.6 and Fig.4.7). There are two different damping ratios : 0% and 20%, for the four different boundary conditions of the Kirchhoff's plate (i.e. CCCC, SSSS, CSCS, and SCSC). The non-D splash time is given by Eq.(4.1). It is seen that damping lowers the peak DLF, and moves it to a slightly higher τ. However, since the time-scale is non-dimensionalized with respect to the fundamental damped frequency of vibration,

the quasi-static behavior begins from a fixed τ, for a given deadrise angle. Grouping the four deadrise angles for a constant damping, the results are as follows. A high τ means slower impact speed, or a stiffer/light plate. A low τ means a faster impact speed, or a softer/massive plate.

Large values of τ causes a quasi-static behavior of the plate for all deadrise angles, all boundary conditions, and all damping ratios. Decreasing τ leads to a steady increase in the DLF, which reaches a peak, and then sharply drops to a virtually zero DLF. At extremely low τ, the impact pressure sweeps across the plate so quickly that the plate does not get the time to respond (quasi-stationary response). At very high impact speeds, i.e. $\tau < 0.6$, the smaller deadrise angle has a marginally lower DLF than the larger deadrise angle, since the pressure sweep is faster for a smaller τ, giving the structure less time to react.

Mild roughness in the DLF characteristic is seen around the peak, which again occurs due to aperiodicity in the time-series of the dynamic deflection, explained in Sec.4.2.1. It becomes smooth again for lower τ, unlike the Uniform Load DLF (Fig.4.2), because the almost instantaneous impact sweep barely excites the higher order modeshapes.

For structural designers, the region $1 < \tau < 2$ is of practical interest, since the coalesced time-scales of typical marine design problems lie here. In this region, a smaller deadrise angle produces a slightly higher DLF for a given τ. This is because the plate, at a smaller deadrise angle, suffers a much larger and more localized impact pressure, which causes far severe dynamic deflections and hence, greater dynamic flexural stresses and strains. Hence the lower-most DLF in the following charts stands for $\beta = 30$ degrees and the uppermost DLF stands for $\beta = 1$ degree.

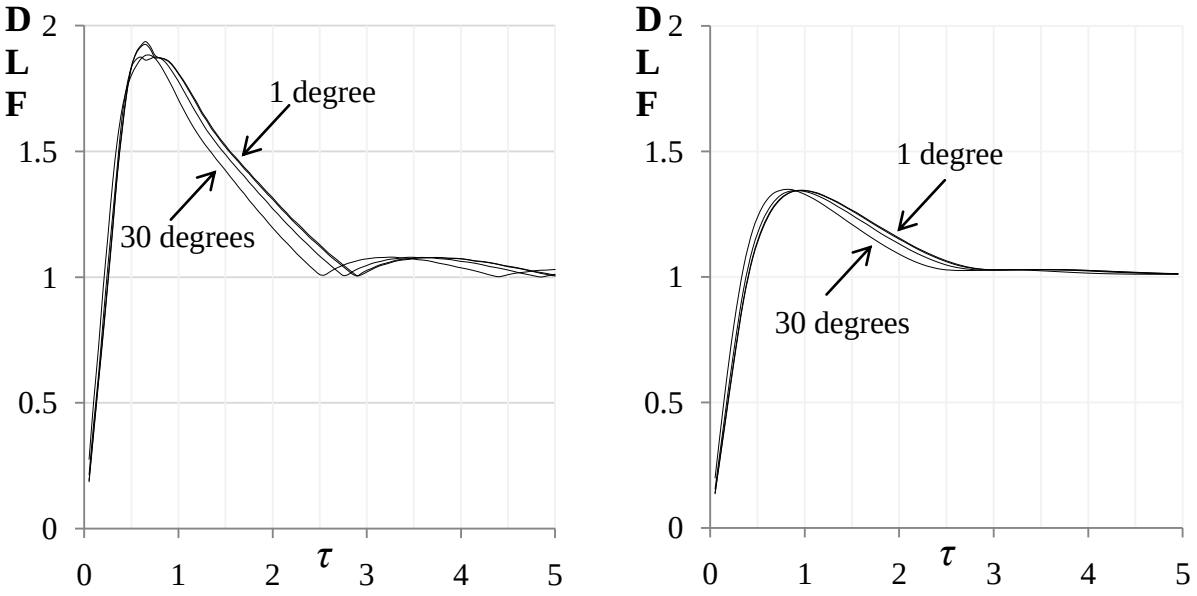

DLF for the **CCCC** plate at four (4) deadrise angles, ζ = (a) 0%, (b) 20%.

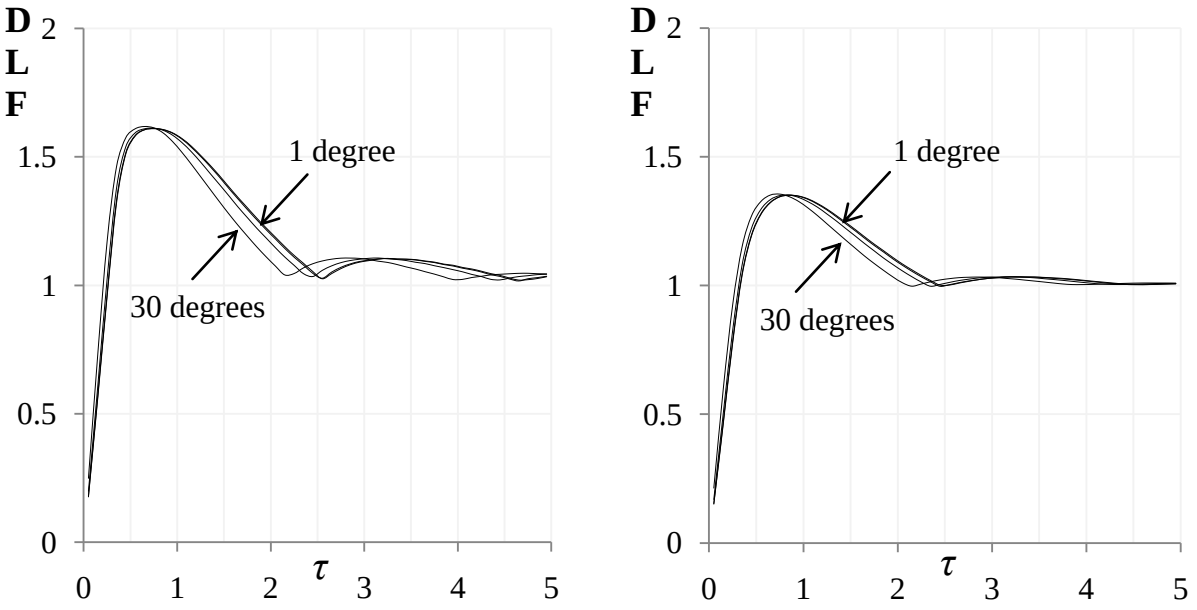

DLF for the **SSSS** plate at four (4) deadrise angles, ζ = (a) 0%, (b) 20%.

Figure 4.6: Impact Load DLF of CCCC and SSSS plates.

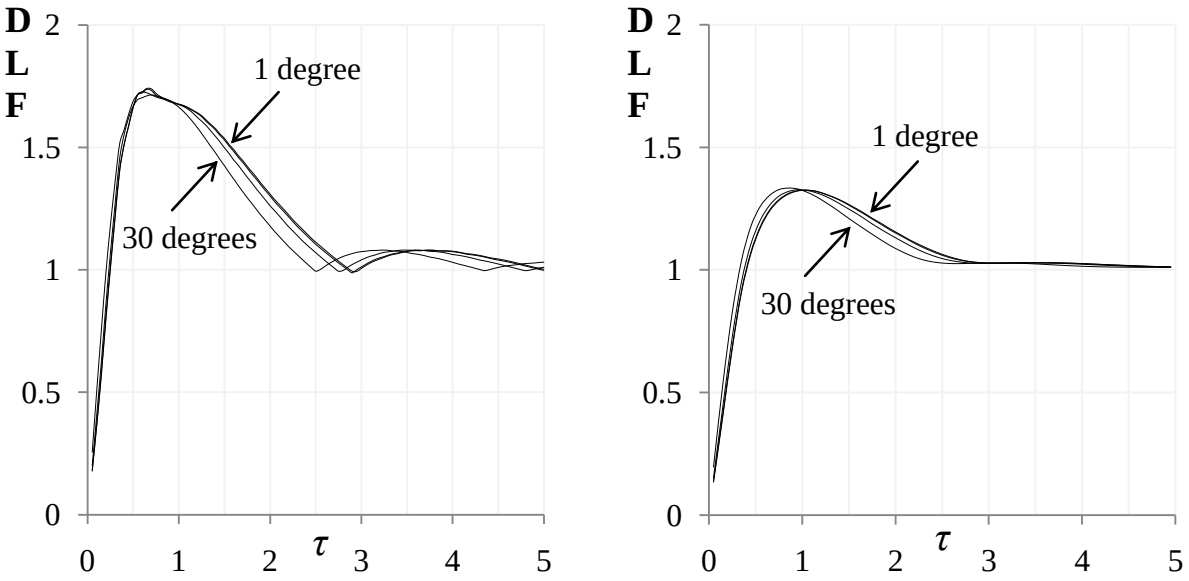

DLF for the **CSCS** plate at four (4) deadrise angles, ζ = (a) 0%, (b) 20%.

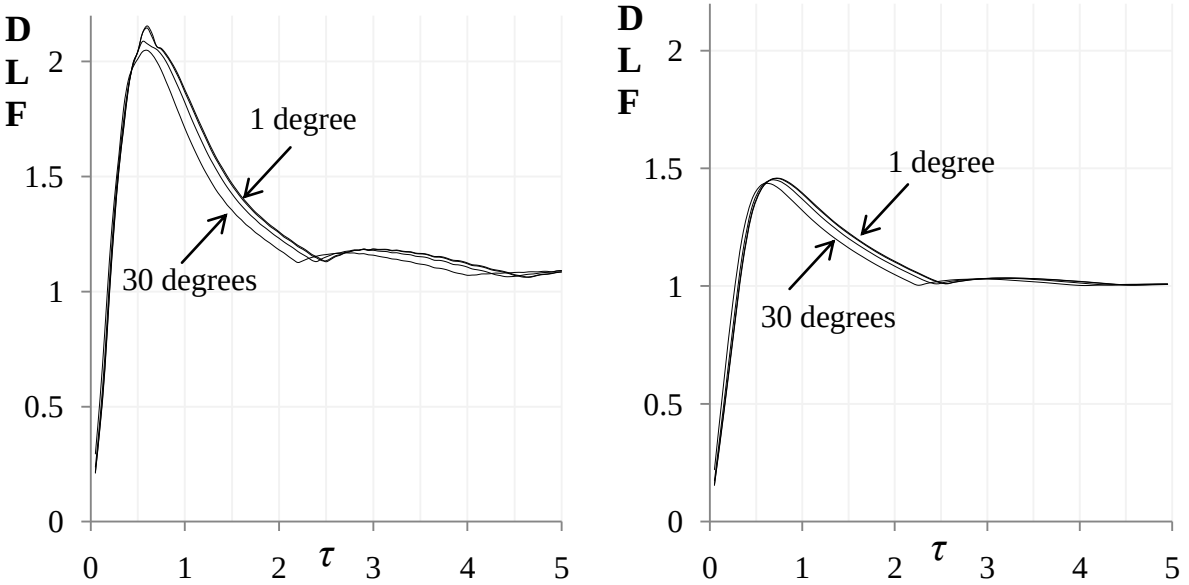

DLF for the **SCSC** plate at four (4) deadrise angles, ζ = (a) 0%, (b) 20%.

Figure 4.7: Impact Load DLF of CSCS and SCSC plates.

Table 4.6 below shows the maximum DLFs for plates with 5% and 10% damping, at deadrise angles β = 1, 5, 15 and 30 degrees; and also the corresponding τ at which they occur. The DLF for these intermediate damping ratios show similar trends as the above plots, except that the damping reduces the peak DLF.

		CCCC		**SSSS**		**CSCS**		**SCSC**	
	$\zeta \rightarrow$	5%	10%	5%	10%	5%	10%	5%	10%
1 degree	DLF	1.693	1.552	1.610	1.512	1.583	1.483	1.873	1.709
	τ	0.45	0.45	0.4	0.4	0.45	0.5	0.35	0.35
5 degrees	DLF	1.692	1.552	1.610	1.512	1.583	1.483	1.872	1.709
	τ	0.45	0.45	0.4	0.4	0.45	0.5	0.35	0.35
15 degrees	DLF	1.695	1.549	1.611	1.513	1.584	1.485	1.867	1.704
	τ	0.4	0.4	0.4	0.4	0.4	0.45	0.35	0.35
30 degrees	DLF	1.699	1.556	1.618	1.518	1.595	1.495	1.846	1.682
	τ	0.35	0.40	0.35	0.35	0.4	0.4	0.3	0.3

Table 4.6 Maximum DLF for plates subjected to impact loads, for ζ = 5%, 10%; and the corresponding τ.

Also, a larger deadrise angle has a smaller corresponding τ for the peak DLF, i.e. the peak DLF shifts *left* on the τ-axis for increasing deadrise angle. For decreasing τ, the DLF for smaller deadrise angles drops earlier, since the pressure sweeps across too fast to amplify the dynamic response.

4.3.2 Relative Modal Contribution.

To highlight why and to what extent the higher order modes are important, the following (Fig.4.8) is shown, with a comparison of a CCCC plate's DLFs for 1x1, 2x2, 3x3 and 6x6 modes, i.e. for a summation of 1, 4, 9, and 36 plate modeshapes respectively, at zero damping and at a deadrise angle of 1 degree. For $\tau > 3$, all the four DLFs show

a similar behavior. However, decreasing the τ makes the contribution of the higher modeshapes more and more pronounced. At the peak DLF, the second modeshape is seen to have $\sim$17% increase in the maximum. Hence the inclusion of the higher order modeshapes is imperative.

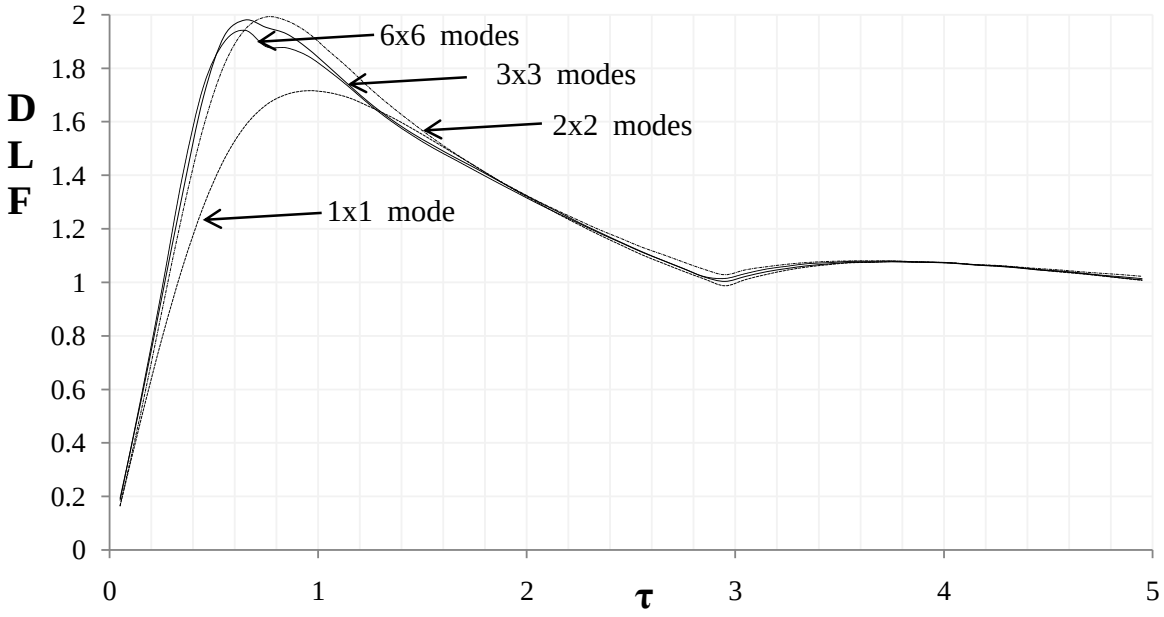

Figure 4.8: CCCC plate's DLFs at $\zeta = 0$ and at $\beta = 1$ degree.

To demonstrate the relative contribution of each modeshape, the following (Fig.4.9) is the RMC of a CCCC plate's dynamics for 15x15 modes, at zero damping and at a deadrise angle of $\beta = 1$ degree. The RMC of only the first 7x7 = 49 modes have been presented for clarity.

The modal truncation for the impact loading is set at 15x15 = 225 modeshapes. For $\tau \sim$0.05, the highest modeshapes have R.M.C. < -3, i.e. the contribution of the highest modeshape in this limit is 10^{-3} times that of the fundamental modeshape. However,

for $\tau >= 0.5$, the highest modeshapes have R.M.C. < -5, i.e. the contribution of the highest modeshape in this limit is only 10^{-5} times that of the fundamental modeshape. It is seen that for a lower value of τ (greater impact speed), the higher order modeshapes have a greater contribution than at higher values of τ (slower impact speeds).

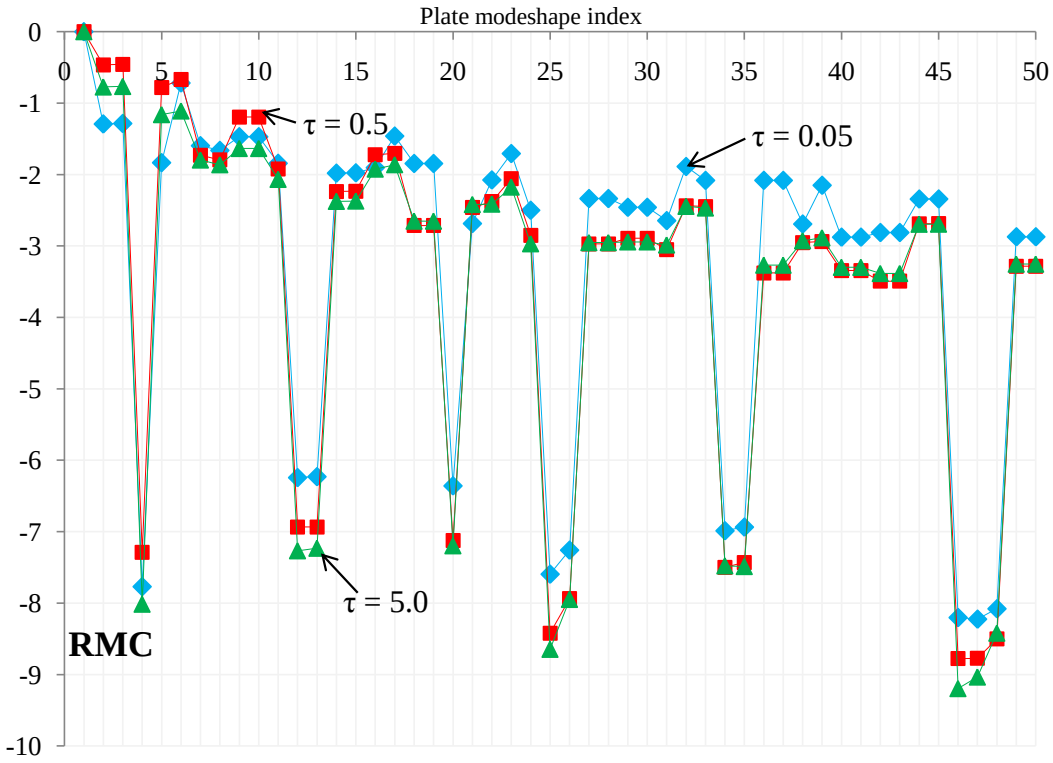

Figure 4.9: RMC of a CCCC plate for 15x15 modes, at zero damping, and at $\beta = 1$ degree, for $\tau = 0.05, 0.5, 5.0$.

The impact load is uniformly distributed in the Y-direction, and thus odd beam modeshapes along the Y-axis contribute significantly, and the even beam modeshapes have very little contribution (Refer Sec.3.2.2). This loading configuration has a concentrated load at the jet head, which excites the odd modeshapes along the X-axis,

also.

As seen above, the modeshapes with indices k = **25** (j = 6, l = 2), **26** (j = 2, l = 6), **34** (j = 6, l = 4) and **35** (j = 4, l = 6), have very little contribution of O($10^{-7.5}$) compared to the fundamental modeshape. However, like the beam vibration RMC, they are not exactly zero, since the static coupling of the plate stiffness matrix causes the principal coordinate $q_k(t)$ to be non-zero, even though the corresponding generalized forcing is zero.

Also, the (*Type b*) repeated frequencies (having similar modeshapes), have equal contributions and RMC. E.g. both the modeshapes k = **9** (j = 1, l = 4) and k = **10** (j = 4, l = 1) have the same RMC at a given τ. Similarly, modeshapes k = **14** (j = 3, l = 4) and k = **15** (j = 4, l = 3) also have the same RMC.

However, k = **32** (j = 1, l = 7) and k = **33** (j = 7, l = 1), having very close (*Type c*) frequencies but very different modeshapes, have close but unequal RMC. The time-scale of the pressure aligns nearly equally with both the non-repeated frequencies, but its spatial configuration aligns differently with them, and hence the difference in their RMCs.

4.3.3 Response at zero wetting time.

For zero wetting time under impact, the keel pressure acts over the whole plate from time t = 0 onwards. Damping has no influence over this limiting value of the DLF for any deadrise angle or any boundary condition. Table 4.7 shows the limiting values of the DLF for the four boundary conditions. Unlike the uniform loading limiting DLFs, the CCCC and CSCS show almost equal DLFs at zero wetting time, and likewise, the SSSS and SCSC DLFs approach each other. For the impact loading configuration, the

loading direction is important at $\tau = 0$ also.

Deadrise angle	CCCC	SSSS	CSCS	SCSC
1 degree	4.03E-06	4.04E-06	4.03E-06	4.04E-06
5 degrees	4.83E-04	4.86E-04	4.83E-04	4.85E-04
15 degrees	1.32E-02	1.33E-02	1.32E-02	1.32E-02
30 degrees	1.25E-01	1.27E-01	1.26E-01	1.27E-01

Table 4.7 DLF at zero wetting time for 4 boundary conditions and 4 deadrise angles.

The deadrise angle of 1 degree is seen to produce an extremely small deflection, virtually a quasi-stationary response. Increasing the deadrise angle leads an increasing limiting value of the DLF, though only ∼12% of the static deflection, under exactly the same pressure distribution.

4.3.4 Generalization of the time-scale by the wave number of the beam mode-shapes.

For impact loading, the generalization of the time-scale with respect to the wave number of the beam modeshape, parallel to the direction of the transient forcing, is done as follows. It is different from the generalization used for the uniform loading. The generalization of the time-scale with respect to the clamped-clamped (CC) beam wave number is done as

$$\tau_{CC} = \left(\frac{2Lsin\beta}{V\pi}\right) \frac{\omega_1\sqrt{1-\zeta^2}}{2\pi} \left[\frac{4.73}{\gamma_n}\right]^{1/4}, \tag{4.4}$$

with n = 1,2,3,4. Here, $\gamma_{1,2} = 4.73$ for the CCCC and CSCS plates; and $\gamma_{3,4} = \pi$ for the SSSS and SCSC plates. The generalization of the time-scale with respect to the simply-supported(SS) beam wave number is done as

$$\tau_{SS} = \left(\frac{2Lsin\beta}{V\pi}\right) \frac{\omega_1\sqrt{1-\zeta^2}}{2\pi} \left[\frac{\pi}{\gamma_n}\right]^{1/4}, \tag{4.5}$$

with n = 1,2,3,4. Here, $\gamma_{1,2} = 4.73$ for the CCCC and CSCS plates; and $\gamma_{3,4} = \pi$ for the SSSS and SCSC plates.

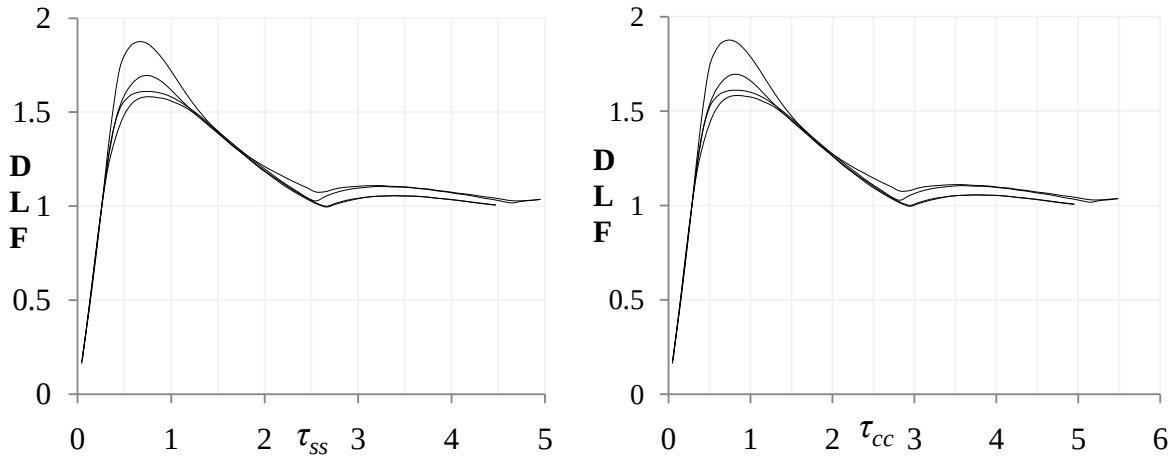

Figure 4.10: Comparative DLF for the four BCs at 5% damping, at $\beta = 1$ degree, generalized to the (a) SS and (b) CC beam fundamental wave number γ.

This modifies the time-scale such that the DLFs for all the four plate boundary conditions (CCCC, SSSS, CSCS and SCSC) are similar within a region of practical marine design interest, i.e. $1.5 < \tau < 2.5$. (Fig.4.10). The quasi-static behavior, i.e. DLF = 1, begins at the same τ (Eq.(5.4) and Eq.(5.5)) for all the four boundary conditions, for both the γ-generalizations. Also, at $\tau < 0.4$, all the four boundary conditions, once again, show self-similar behavior. The maximum DLF, too, is seen to occur at around the same τ for all the four boundary conditions, with both the generalizations.

4.4 Vibration of Rectangular plates.

A new dimension has been added to the parameter space of the problem, i.e. the aspect ratio. The previous work has been extended from a square plate to a more

practical rectangular plate. The response of plate with aspect ratios $\alpha > 1$ and $\alpha < 1$ have been both studied, since the vessels may be either longitudinally framed or transversely framed. The vibration of plates for large aspect ratios have been compared to that of an Euler-Bernoulli beam [60], since the formers' frequencies approach the latter's.

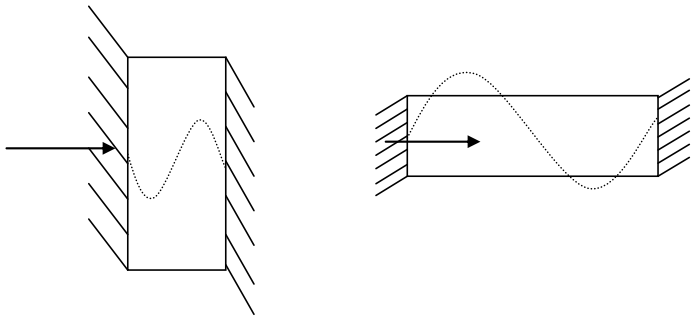

Figure 4.11: CSCS plate with aspect ratios (a) $\alpha = 0.25$ and (b) $\alpha = 4$.

Fig.4.11 shows a CSCS plate the aspect ratios 0.25 and 4, with the forcing direction shown. For (a), the plate vibrates like a CC beam, with the beam modeshape parallel to the forcing direction. The beam modeshape parallel to the direction of the forcing gets excited, as shown. For (b), the vibration in either axis is restricted, leading to erratic DLF characteristics. Here, the beam modeshape parallel to the direction of the forcing is restricted by the narrow beam, leading to a disturbed response.

4.4.1 Free vibration of Rectangular plates.

The dry analysis of rectangular plates (CCCC, SSSS, CSCS) has been done for 100 modes to establish the accuracy of the first four significant figures of the first 36 frequencies, non-dimensionalized by $\sqrt{\frac{D}{mL^4}}$, to generate the Non-D $\omega_{k,dry}$ (Table 4.8).

α	0.1	0.2	0.25	0.33	0.5	1	2	3	4	5	10
CCCC	22.43	22.63	22.79	23.19	24.57	**35.98**	24.57	23.19	22.79	22.63	22.43
SSSS	*9.968*	*10.26*	*10.48*	*10.96*	*12.33*	***19.73***	*12.33*	*10.96*	*10.48*	*10.26*	*9.968*
CSCS	22.42	22.59	22.71	22.99	23.81	**28.95**	*13.68*	*11.35*	*10.64*	*10.34*	*9.978*
SCSC	*9.978*	*10.34*	*10.64*	*11.35*	13.68	**28.95**	23.81	22.99	22.71	22.59	22.42

Table 4.8 Fundamental frequencies of rectangular plates with four boundary conditions.

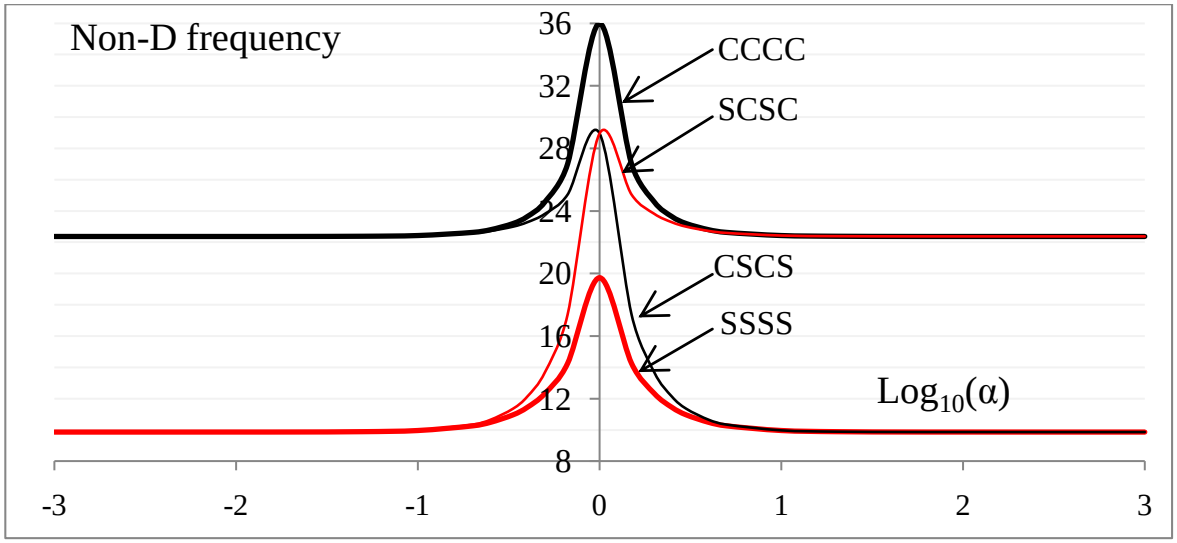

Figure 4.12: Fundamental frequencies of rectangular plates.

The aspect ratio changes (a) the natural frequency of the plate and (b) the wetting time. This analysis has been done for 11 aspect ratios. At large α, the natural frequencies and DLFs of CCCC plates approach that of a Clamped-Clamped (CC) beam, and those of and SSSS plate approach that of a Simply-Supported (SS) beam. A CSCS plate tends to vibrate like a CC beam at a low aspect ratio; and as a SS beam at a high aspect ratio. Likewise, a SCSC plate vibrates like a SS beam at a low aspect ratio; and as a CC beam at high aspect ratio. Fig.4.12 shows the frequencies plotted as a function of $log_{10}(\alpha)$.

k	j	l	α = 0.1	j	l	α = 0.2	j	l	α = 0.5	j	l	α = 2	j	l	α = 5	j	l	α = 10
1	1	1	22.43	1	1	22.64	1	1	24.58	1	1	24.58	1	1	22.64	1	1	22.43
2	1	2	22.62	1	2	23.45	1	2	31.84	2	1	31.84	2	1	23.45	2	1	22.62
3	1	3	22.93	1	3	24.90	1	3	44.80	3	1	44.80	3	1	24.90	3	1	22.93
4	1	4	23.38	1	4	27.05	1	4	63.36	4	1	63.36	4	1	27.05	4	1	23.38
5	1	5	23.98	1	5	30.04	2	1	64.00	1	2	64.00	5	1	30.04	5	1	23.98
6	1	6	24.72	1	6	33.85	2	2	71.12	2	2	71.12	6	1	33.85	6	1	24.72
7	2	1	61.75	2	1	62.01	2	3	83.41	3	2	83.41	1	2	62.01	1	2	61.75
8	2	2	61.99	2	2	63.00	1	5	87.33	5	1	87.33	2	2	63.00	2	2	61.99
9	2	3	62.40	2	3	64.69	2	4	100.9	4	2	100.9	3	2	64.69	3	2	62.40
10	2	4	62.96	2	4	67.03	1	6	116.4	6	1	116.4	4	2	67.03	4	2	62.96
11	2	5	63.72	2	5	70.20	3	1	123.3	1	3	123.3	5	2	70.20	5	2	63.72
12	2	6	64.59	2	6	73.99	2	5	124.0	5	2	124.0	6	2	73.99	6	2	64.59
13	3	1	121.0	3	1	121.3	3	2	130.5	2	3	130.5	1	3	121.3	1	3	121.0
14	3	2	121.3	3	2	122.3	3	3	142.7	3	3	142.7	2	3	122.3	2	3	121.3
15	3	3	121.7	3	3	124.1	2	6	152.2	6	2	152.2	3	3	124.1	3	3	121.7
16	3	4	122.3	3	4	126.6	3	4	159.9	4	3	159.9	4	3	126.6	4	3	122.3
17	3	5	123.1	3	5	129.9	3	5	182.6	5	3	182.6	5	3	129.9	5	3	123.1
18	3	6	124.1	3	6	133.8	4	1	202.3	1	4	202.3	6	3	133.8	6	3	124.1
19	4	1	200.0	4	1	200.2	4	2	209.5	2	4	209.5	1	4	200.2	1	4	200.0
20	4	2	200.2	4	2	201.3	3	6	210.1	6	3	210.1	2	4	201.3	2	4	200.2
21	4	3	200.7	4	3	203.2	4	3	221.8	3	4	221.8	3	4	203.2	3	4	200.7
22	4	4	201.3	4	4	205.8	4	4	238.9	4	4	238.9	4	4	205.8	4	4	201.3
23	4	5	202.2	4	5	209.2	4	5	261.6	5	4	261.6	5	4	209.2	5	4	202.2
24	4	6	203.1	4	6	213.2	4	6	288.7	6	4	288.7	6	4	213.2	6	4	203.1
25	5	1	298.7	5	1	299.0	5	1	301.1	1	5	301.1	1	5	299.0	1	5	298.7
26	5	2	299.0	5	2	300.1	5	2	308.4	2	5	308.4	2	5	300.1	2	5	299.0
27	5	3	299.5	5	3	302.1	5	3	320.9	3	5	320.9	3	5	302.1	3	5	299.5
28	5	4	300.1	5	4	304.7	5	4	338.0	4	5	338.0	4	5	304.7	4	5	300.1
29	5	5	301.1	5	5	308.3	5	5	360.8	5	5	360.8	5	5	308.3	5	5	301.1
30	5	6	302.0	5	6	312.3	5	6	387.9	6	5	387.9	6	5	312.3	6	5	302.0
31	6	1	417.1	6	1	417.4	6	1	419.5	1	6	419.5	1	6	417.4	1	6	417.1
32	6	2	417.4	6	2	418.5	6	2	426.9	2	6	426.9	2	6	418.5	2	6	417.4
33	6	3	417.9	6	3	420.5	6	3	439.4	3	6	439.4	3	6	420.5	3	6	417.9
34	6	4	418.5	6	4	423.2	6	4	456.6	4	6	456.6	4	6	423.2	4	6	418.5
35	6	5	419.5	6	5	426.8	6	5	479.5	5	6	479.5	5	6	426.8	5	6	419.5
36	6	6	420.4	6	6	430.9	6	6	506.5	6	6	506.5	6	6	430.9	6	6	420.4

Table 4.9 First 6x6 = 36 Non-dimensional Frequencies of rectangular CCCC plates, with the dominant beam indices, for 6 different aspect ratios.

Table 4.9 shows the first 6x6 = 36 frequencies of a CCCC plate at 3x2 = 6 different aspect ratios. For $\alpha = \mathbf{0.1}$, the fundamental modeshape in the x-direction, i.e. j = 1 dominates the first six plate plate modeshapes. The next six frequencies are dominated by j = 2 beam modeshape, the next six by j = 3 beam modeshape, and so on. The trend is reversed for the plate with $\alpha = \mathbf{10}$. Here, the fundamental modeshape in the y-direction, i.e. l = 1 dominates the first six plate modeshapes. The next six frequencies are dominated by l = 2 beam modeshape, the next six by l = 3 beam modeshape, and so on. There is a large difference of magnitude between the 6^{th} and the 7^{th} frequency, the 12^{th} and the 13^{th} frequency and so on.

The above trend is replicated by the plates with $\alpha = \mathbf{0.2}$ and $\alpha = \mathbf{5}$ respectively. This shows that the plate behaves almost like a beam, with the higher modeshapes along the shorter edge hardly participating in the vibration. The frequency-magnitudes can be easily grouped into six sequential sets with a common j value, i.e. there are quantum leaps in the frequency magnitude down the frequency table.

As the plate becomes more squarish, the beam modeshapes along the shorted edge become more prominent, and the above sequencing gets distorted, with the plate with $\alpha = \mathbf{0.5}$ having the plate modeshape k = 5 dominated by j = 2 and l = 1 beam modeshapes, instead of j = 1 and l = 5 beam modeshapes. This trend is mirrored by the plate with $\alpha = \mathbf{2}$ having the plate modeshape k = 5 dominated by j = 1 and l = 2 beam modeshapes, instead of j = 5 and l = 1 beam modeshapes. The increase in the frequency magnitude is far more gradual, with k = 7 (j = 2, l = 3) and k = 8 (j = 1, l = 5) having close frequencies, indicting similar excitement under forcing, and comparable modal contribution in vibration.

4.4.2 Response to Uniform Loading.

A unit load stretches across the plate of length L and width B, at a speed of V. The plate is set into small-amplitude flexural vibrations. The dynamic load factor (DLF) is plotted against the non-dimensionalized wetting time τ for the four different boundary conditions of the Kirchhoff's plate.

4.4.2a Dynamic Loading Factor.

Plates with $\alpha = \mathbf{a}$ and $\alpha = 1/\mathbf{a}$ have different DLF characteristics, except at very low τ, when the two DLFs asymptote to a unique value. The DLFs for $\alpha < 1$ approach that of an Euler-Bernoulli beam, while the DLFs for $\alpha > 1$ blur away from the $\alpha = 1$ characteristic to a trend where little vibration occurs.

Fig.4.13(a) shows the DLF of CC and SS beams under Uniform stretching load, at zero damping. Fig.4.13(b) shows the DLF of the plates with aspect ratio $\alpha = \mathbf{0.1}$. The SSSS and SCSC plates behave like a SS beam at low aspect ratios, while the CCCC and CSCS plates behave like a CC beam at low aspect ratios.

The Fig.4.14 above shows that for $\alpha = \mathbf{0.5}$, the CCCC and CSCS plates behave similarly, and so do the SSSS and SCSC plates. But for $\alpha = \mathbf{2}$, The CCCC and SCSC behave similarly, while the SSSS and the CSCS plates behave similarly. This trend continues for $\alpha = \mathbf{5}$ and $\mathbf{10}$ as shown below in Fig.4.15.

As seen in the following plots, plates with all the four boundary conditions have the same DLF at very low wetting times, for aspect ratios $\alpha = \mathbf{0.1}$, $\mathbf{5}$, $\mathbf{10}$. This is because the forcing works on the whole plate almost instantaneously, making the direction of forcing immaterial with respect to the boundary conditions.

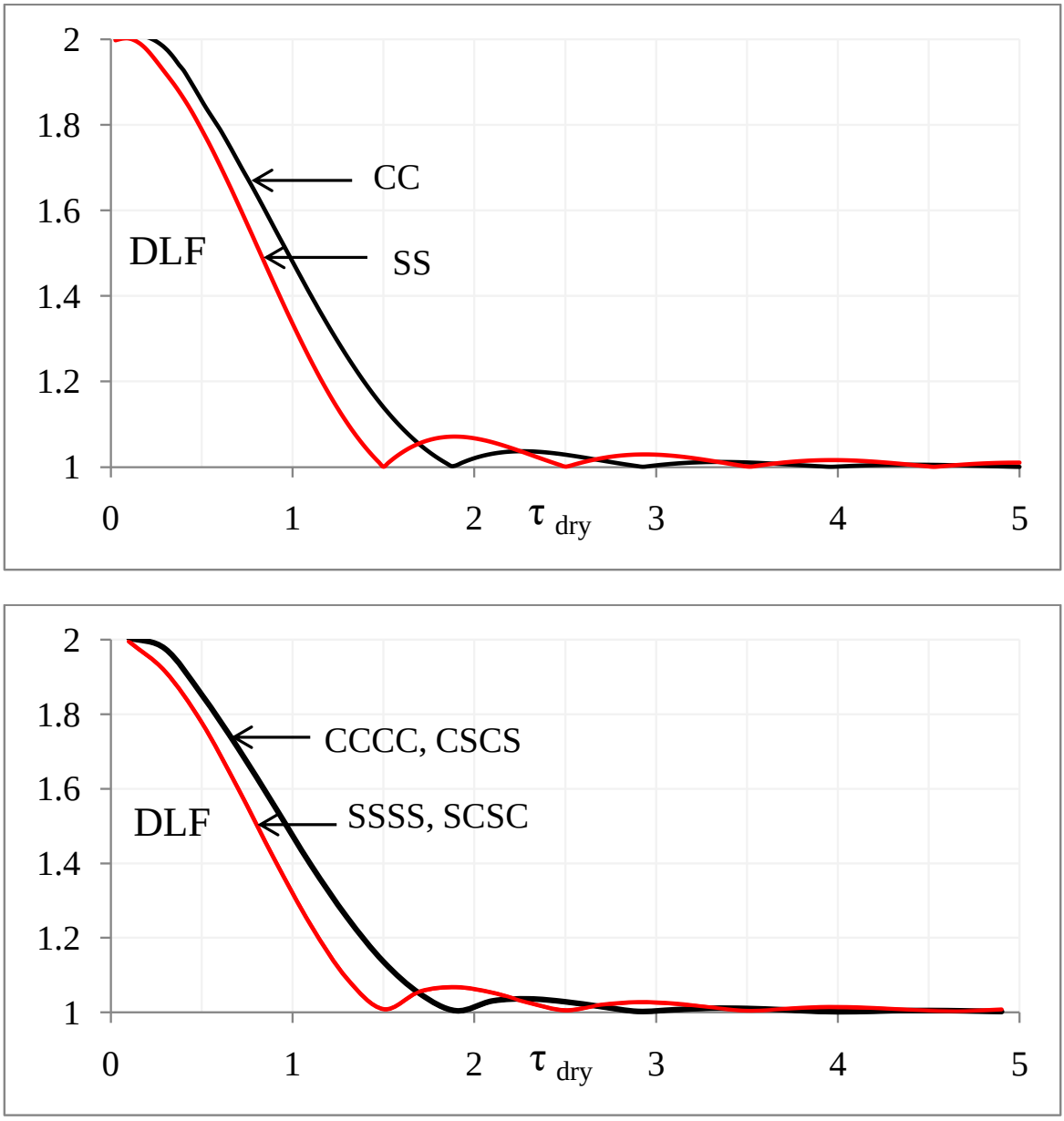

Figure 4.13: (a) CC and SS beam DLF to Uniform load, (b) DLF of plates at $\alpha = 0.1$ to uniform load, for zero damping.

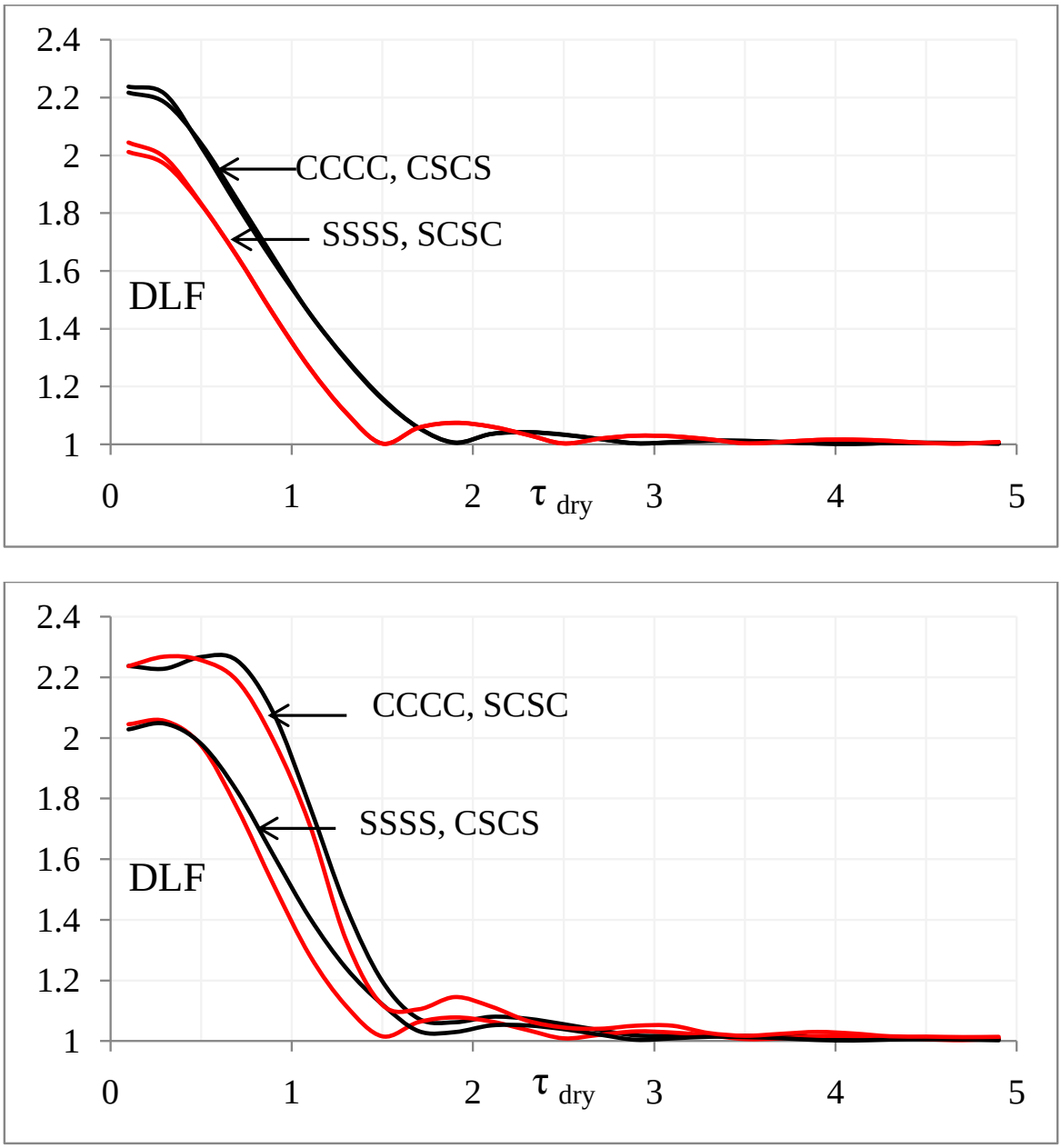

Figure 4.14: (a) DLF of plates at $\alpha = 0.5$ to uniform load, (b) DLF of plates at $\alpha = 2$ to uniform load, for zero damping.

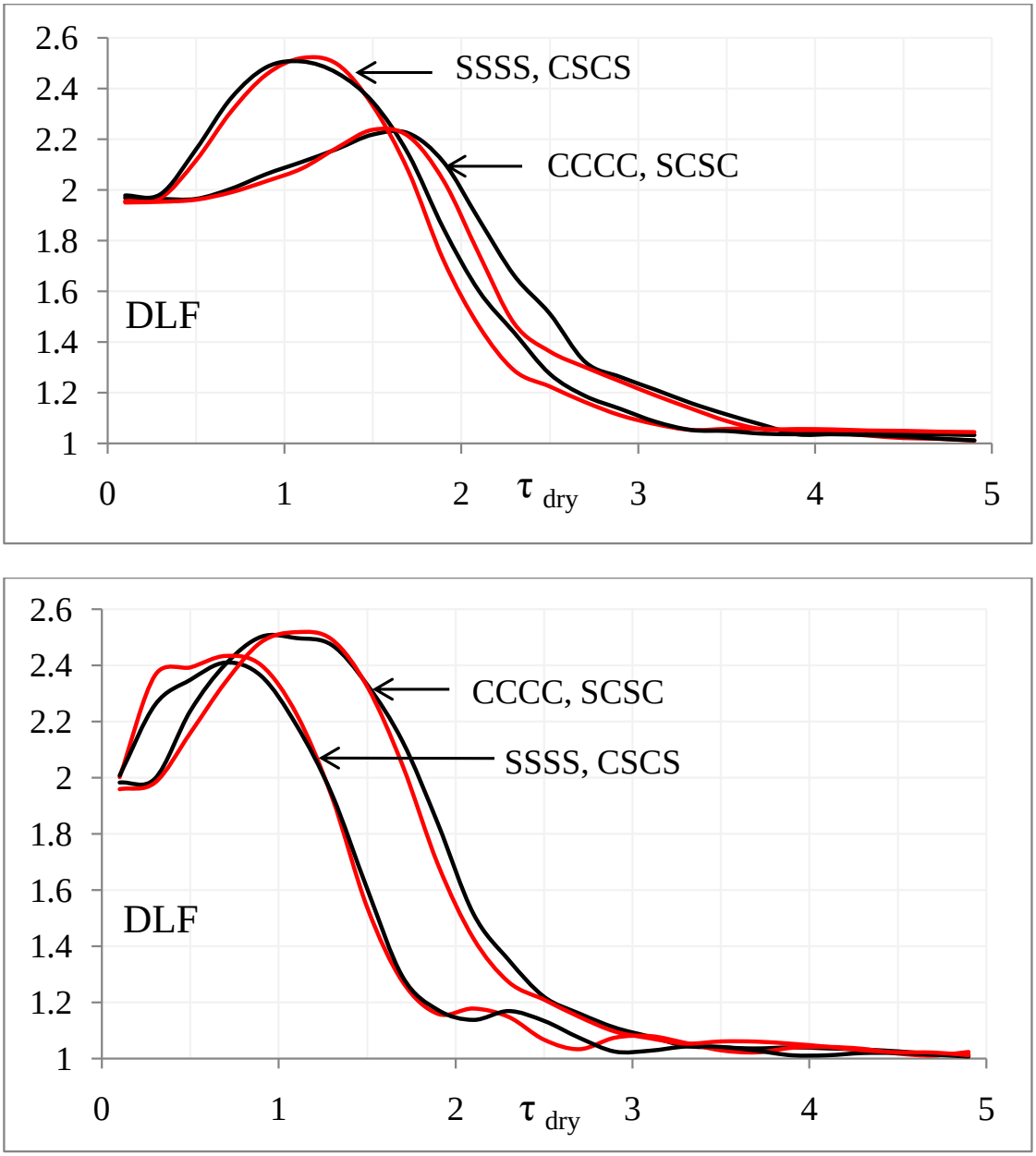

Figure 4.15: (a) DLF of plates at $\alpha = 5$ to uniform load, (b) DLF of plates at $\alpha = 10$ to uniform load, for zero damping.

4.4.2b Relative Modal Contribution.

To study the influence of aspect ratio on the modal truncation limits, the Relative Modal Contribution(R.M.C.) of the first 6x6 = 36 plate modeshapes is estimated for the rectangular plate, at two different non-D wetting times $\tau = 0.1$ and 5.0.

Fig.4.16(a) shows the RMC for a plate at $\alpha = \mathbf{10}$, i.e. the forcing is parallel to the *longer* edge. Modes having the dominant y-direction beam mode *odd*, have a considerable contribution to the dynamic deflection; and those having the dominant y-direction beam mode *even*, have an insignificant contribution, less than $O(10^{-7})$. Making the plate more squarish, fig.4.16(b) shows the RMC for a plate at $\alpha = \mathbf{2}$. Modeshapes with a dominant x-direction beam mode *odd*, have a large contribution; and those with a dominant x-direction beam mode *even*, have an insignificant contribution, less than $O(10^{-7})$.

Turning the plate by 90 degrees, such that the forcing is parallel to the *shorter edge*, Fig.4.17(a) shows the RMC for plate at $\alpha = \mathbf{0.5}$. Repeating the trend, modes having an *odd* dominant y-direction beam mode have a considerable contribution to the dynamic deflection. Modes having an *even* dominant y-direction beam mode, have an negligible contribution, less than $O(10^{-6})$. Making the plate more rectangular, fig.4.17(b) shows the RMC for a plate at $\alpha = \mathbf{0.1}$. Once again, modeshapes with a dominant x-direction beam mode *odd*, have a large contribution; and those with a dominant x-direction beam mode *even*, have an insignificant contribution, less than $O(10^{-4})$.

If the longer edge is parallel to the forcing (x-direction), the beam modeshapes along the y-direction are excited at least 100 times less than the same when the shorter edge is parallel to the forcing. Thus hulls with *longitudinal* framing excite a larger number of modes, to a greater extent.

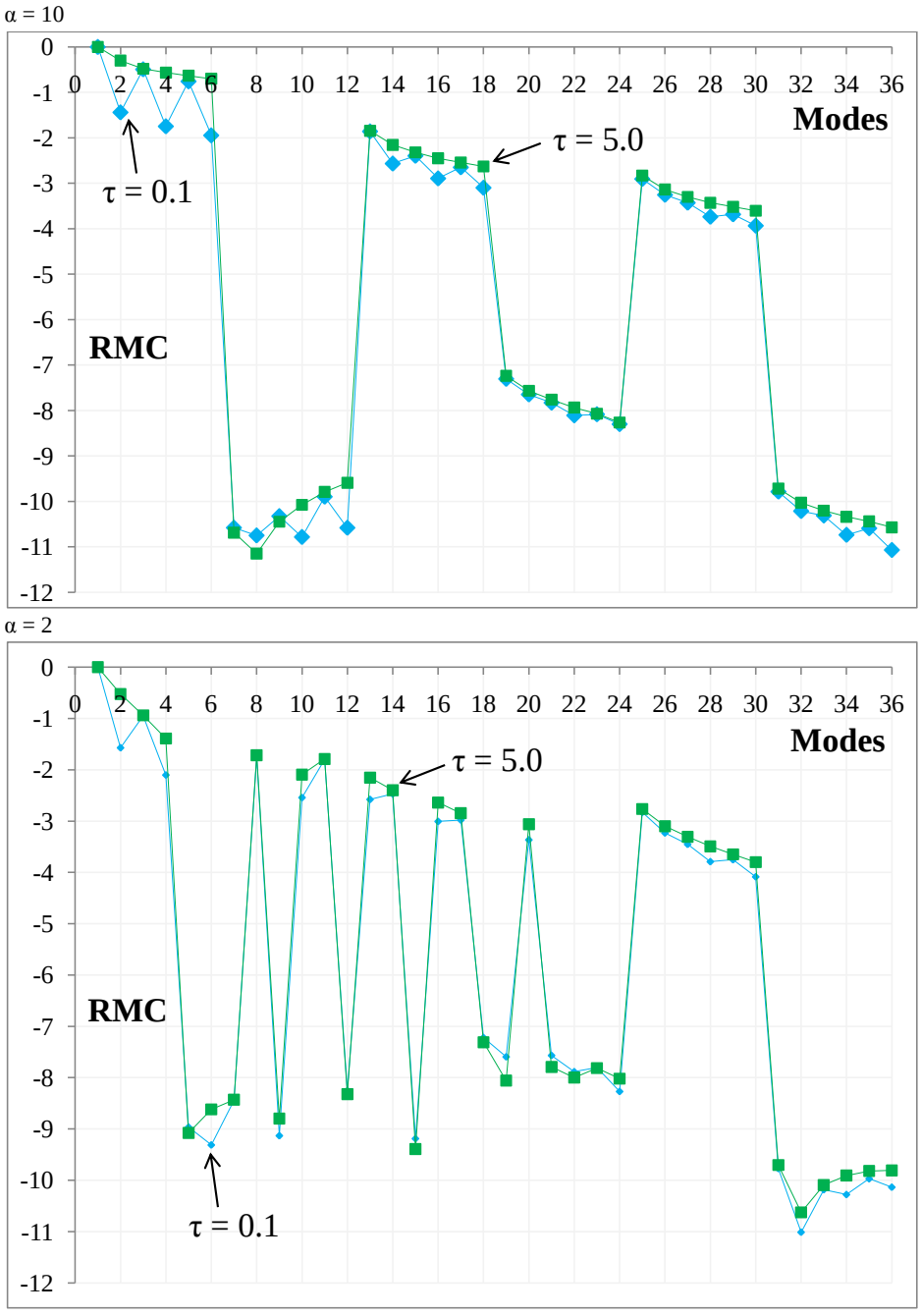

Figure 4.16: (RMC in response to uniform load at $\tau = 0.1$ and $\tau = 5.0$ for aspect ratios (a) 10, (b) 2.

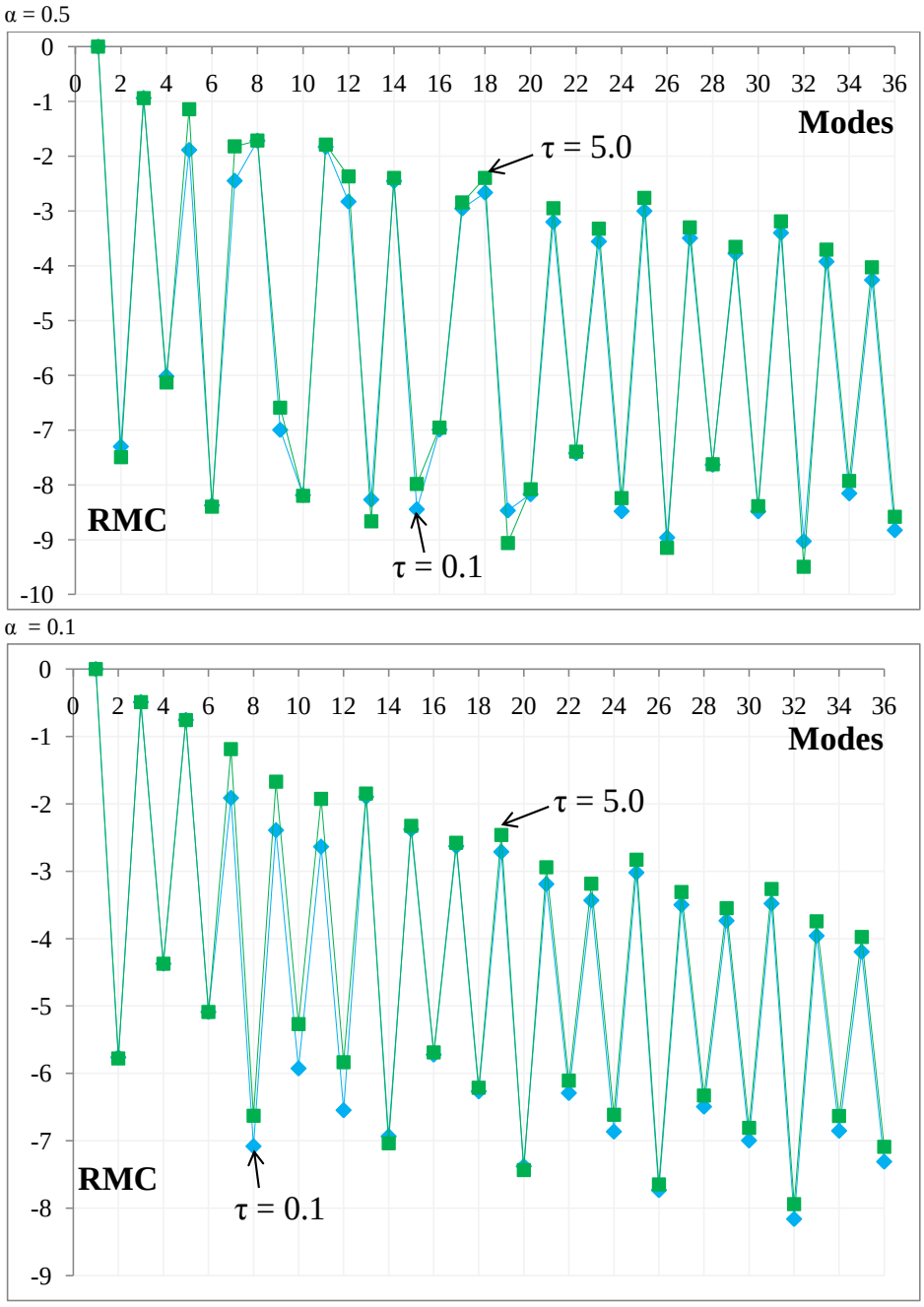

Figure 4.17: (RMC in response to uniform load at $\tau = 0.1$ and $\tau = 5.0$ for aspect ratios (a) 0.5, (b) 0.1.

4.4.2c Response at zero wetting time.

For $\tau = 0$, the uniform load acts over the whole of the plate from time t = 0 onwards (Table 4.10). below shows that the DLF at zero wetting time for 11 different aspect ratios.

α	**0.1**	**0.2**	**0.25**	**0.33**	**0.5**	**1**	**2**	**3**	**4**	**5**	**10**
CCCC	2.010	2.001	1.988	1.993	2.232	2.094	2.232	1.993	1.988	2.001	2.010
SSSS	1.996	1.997	2.143	2.220	2.044	1.999	2.044	2.220	2.143	1.997	1.996
CSCS	2.010	2.002	1.995	1.990	2.223	2.052	2.016	2.223	2.151	1.992	1.995
SCSC	1.995	1.992	2.151	2.223	2.016	2.052	2.223	1.990	1.995	2.002	2.010

Table 4.10 Undamped DLF of rectangular plates at $\tau = 0$ (zero wetting time) for Uniform load, for four Boundary conditions.

The DLF is same for $\alpha = \mathbf{a}$ and $\alpha = 1/\mathbf{a}$ for both CCCC and SSSS plates. The DLF for CSCS plate at $\alpha = \mathbf{a}$ equals the DLF for SCSC plate at $\alpha = 1/\mathbf{a}$. At small α, the CSCS and SCSC DLFs approach those of CCCC and SSSS respectively. At large α, the CSCS and SCSC DLFs approach that of SSSS and CCCC respectively.

4.4.3 Response to Impact loading.

An impact load sweeps across the plate of length L and width B, at two extreme deadrise angles, i.e. $\beta = 1$ and 30 degrees. The dynamic load factor (DLF) is plotted against the non-dimensionalized splash time τ for the two different boundary conditions of the Kirchhoff's plate, i.e. CCCC and SSSS.

Fig.4.18 shows the dry DLF of CCCC plates at $\alpha = \mathbf{0.1}$, $\mathbf{0.2}$, $\mathbf{0.5}$, $\mathbf{2}$, $\mathbf{5}$, and $\mathbf{10}$; in response to impact loads at $\beta = 1$ and 30 degrees. For $\alpha < 1$, the DLF is less than 2 for all deadrise angles. For $\alpha > 1$, the DLF rises higher , with $\alpha = \mathbf{5}$ showing the highest dynamic deflections at around $\tau \approx 1.1$.

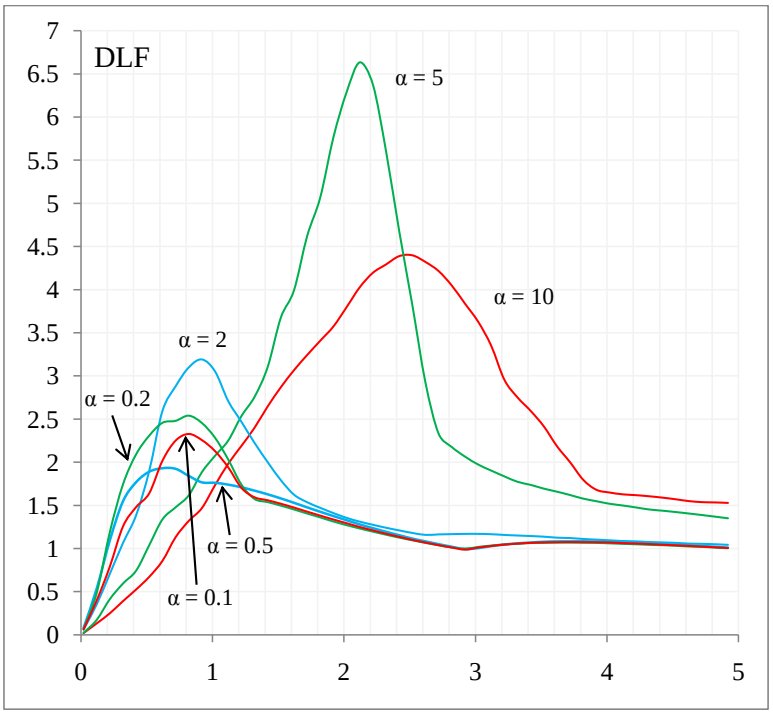

DLF of rectangular plates to impact load at beta = 1 degree.

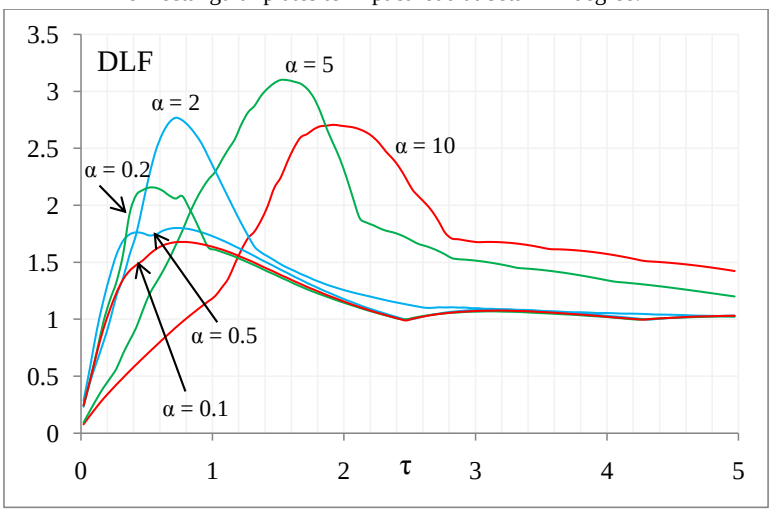

DLF of rectangular plates to impact load at beta = 30degree.

Figure 4.18: Dry DLF of rectangular CCCC plates for impact forcing, at six(6) aspect ratios, and two(2) deadrise angles $\beta = 1$, 30 degrees, and zero damping.

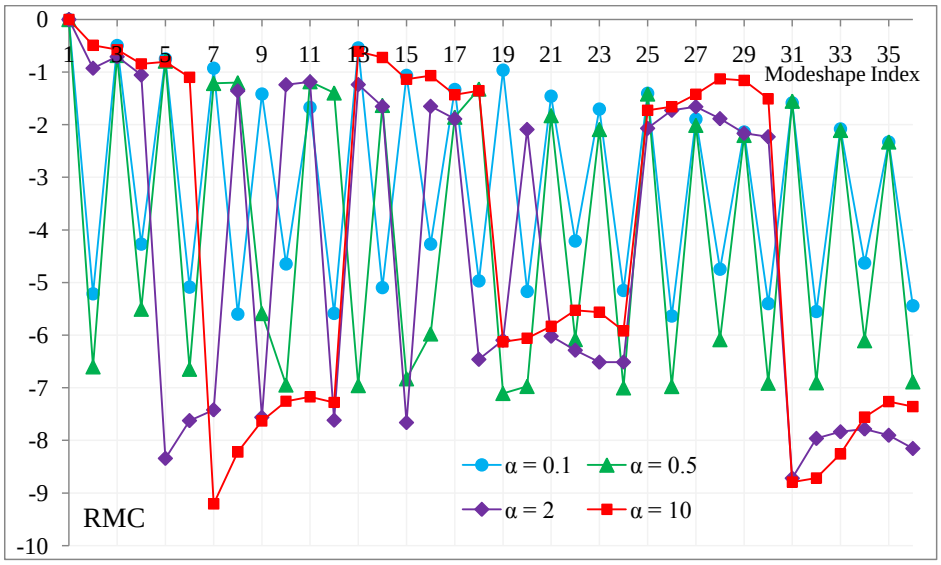

Figure 4.19: RMC of rectangular CCCC plates for impact forcing, at four(4) aspect ratios, and deadrise angle $\beta = 1$ degree, at $\tau = 0.05$.

Comparing Fig.4.18(a) and Fig.4.18(b), it is seen that a smaller deadrise angle produces a larger dynamic deflection, due to larger and more concentrated impulse pressure. For $\beta = 30$ degrees, the maximum DLF is less than 3.5 for $\alpha = \mathbf{5}$. The same rises close to 6.6 for $\beta = 1$ degree, at around the same non-D wetting time. Making the plate more squarish ($\alpha \rightarrow 1$) makes the DLF characteristic approach the square plate DLF characteristic as discussed earlier in section 3.3. Lengthening the edge parallel to the forcing, i.e. $\alpha >> 1$ decreases the DLF again, since the plate is unable to react due to its restricted motion along the width.

The Relative Modal Contribution (RMC) of CCCC plates subject to impact loading at $\beta = 1$ degree, is shown in Fig.4.19 for $\alpha = \mathbf{0.1}$, $\mathbf{0.5}$, $\mathbf{2}$, and $\mathbf{10}$; at a non-D wetting time of $\tau = 0.05$. The trends are similar as those in Fig.4.16 and Fig.4.17.

4.5 Discussion

A detailed, meticulous and intricate study of the elastic dynamics of a Kirchhoff's plate is presented. Here, four different boundary conditions have been used; and structural damping has been incorporated. The free vibration analysis has been done for the three boundary conditions of the plate with a very high numerical accuracy, using 15x15 = 225 plate modeshapes. The plate modeshapes, generated by the Eigen value analysis of the governing differential equation of free vibration, have been tabulated systematically for 7x7 = 49 modeshapes. The three types of natural frequencies have been distinguished with respect to the modeshapes, and also the dominant beam modeshape contributions A_{jl}^{k}. The frequencies, and their relative modal contributions to the DLF, have been studied in detail.

The independent variable of the analysis, the time-scale τ, has been generalized with respect to the damping ratio ζ, the deadrise angle β, and the beam modeshape wave number γ parallel to the direction of the forcing. All these generalizations consolidate the self-similarity of the various DLFs, aiding the structural designer in interpretation of the charts.

The dynamic load factor (DLF) of Kirchhoff's plates, subject to the benchmark uniform loading and the more realistic impact loading have been clearly established. The quasi-static and the dynamic behavior of the structure subject to such transient loadings have been clearly demarcated. Damping is shown to lower the peak DLF. The static deflection is analyzed as a function of time by the Galerkin's method, under exactly the same loading configuration, which when multiplied by the DLF at the appropriate $\Phi_k(x, y)$, generates the maximum dynamic deflection of the plate, and thus, the corresponding maximum pure bending strains and stresses.

The limiting case of the transient forcing, with $\tau = 0$, has also been studied separately for both the uniform and impact loading. Their dependence on the boundary conditions of the plate and the forcing configuration, and independence from the damping ratio, have all been established.

The free and forced vibration of rectangular plates have been studied, with the fundamental natural frequencies of plates Kirchhoff's plate with three different boundary conditions (CCCC, SSSS, and CSCS), and the first 36 natural frequencies of rectangular CCCC plates established for the first four significant figures. The consistent DLF and RMC trends of the rectangular plates to uniform loading have been established, and compared with the beam vibration results. The impact loading response has been evaluated for two extreme deadrise angles of $\beta = 1$ and 30 degrees, showing 6-7 times the static deflection z_{st} for $\alpha > 1$, as compared to DLF ≈ 2 for plates with $\alpha = 1$.

Kunow-Baumhauer [64] investigated the response of a plate to a transient pressure wave load. He calculated the static deflection by considering an area load representation of the pressure load, and concluded that the propagation direction is not important for the plate response. The sinusoidal wave load causes the principal coordinates to be formulated analytically. However here, the the static deflection has been calculated as a function of time, considering the exact transient loading configuration as used for the dynamic analysis. The propagation direction is important for the mixed boundary conditions used here, CSCS and SCSC. The principal coordinates have been numerically evaluated by time-integration, since the forcing is arbitrary and does not have an analytical formulation. Also, the dissertation has investigated the relative modal contribution, modal convergence for both free and force vibrations and clearly established the modal truncation limits.

CHAPTER V

WET VIBRATION OF KIRCHHOFF'S PLATE.

Following the detailed *dry* vibration analysis, we recall that the slam-induced response of marine and high-speed vessels involves the *wet* vibrations of the bow, keel, and the wetdeck. The natural frequency of vibration of elastic structures is considerably reduced in water as compared to in air. The marine structure is subjected to intense moving hydrodynamic pressures (Fig.5.1), which sets it into high frequency, weakly damped submerged vibrations. Vibration analysis becomes mandatory for efficient structural design of susceptible marine structures under vulnerable environmental conditions. Water inertia augments the inertia of the dynamic system, predisposing it to greater dynamic response.

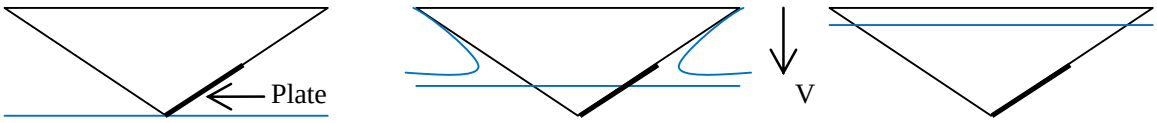

Figure 5.1: Wedge impacting against the water, with a section of the hull as an elastic plate at time t = 0, (b) time $t < \frac{L}{V}$, and (c) time $t >> \frac{L}{V}$.

This chapter investigates the elastic response of rectangular plates in contact with water on one side (Fig.5.2), subject to intense localized moving hydrodynamic impact loads. Dry vibration analysis is first done to generate the dry natural frequencies (*Eigen values*) and modeshapes (*Eigen vectors*) of the plate [35-38]. The dry modeshapes are utilized in the wet vibration modal analysis.

The boundary value problem has been framed with the *kinematic* body boundary condition, i.e. transverse velocity of the plate is equal to the normal velocity of the water in contact with the surface. Three-dimensional (3D) constant-strength source distribution panels have been used to model the water vibrating in contact with the plate, utilizing the relation between the dry plate modeshape and the fluid velocity potential. This is followed by evaluating the modal added masses. The wet natural frequency has been then calculated for rectangular plates, using *square* panels. The variation of the added mass with different plate aspect ratios and boundary conditions has been studied.

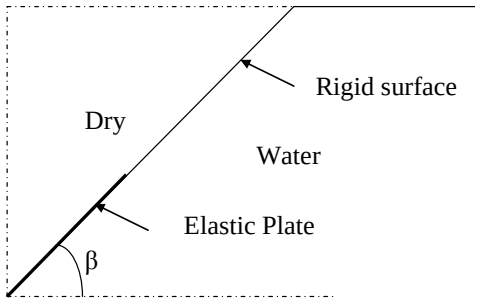

Figure 5.2: Submerged vibration.

The decrease in the natural frequency from dry to wet vibration has been studied for different solid-to-fluid density ratios and plate thicknesses. The **n**on-dimensional **a**dded **v**irtual **m**ass **i**ncrement (NAVMI) factor has been established for different aspect ratios and boundary conditions, for the first 6x6 = 36 modeshapes of each plate. This factor shows the influence of the plate modeshape on the added mass effect.

Free vibration leads to the forced vibration modal analysis, with two different forcing configurations, moving at different wetting speeds V, namely (a) Uniform stretching

load and (b) Impact load at five different deadrise angles β. The plate has been again modelled with four different boundary conditions, several aspect ratios α, and two different damping ratios ζ. The wet modal governing differential equations of motion are numerically time-integrated by the Euler's explicit-implicit method, to generate the dynamic deflection as a function of time. Galerkin's method has been used to generate the time series for the corresponding static deflection, under identical loading configuration.

The maximum dynamic deflection, in space and time, has been normalized by the maximum static deflection under the same loading configuration, to generate the dynamic loading factor (DLF). The quasi-static and the dynamic zones of the DLF, as a function of τ, have been clearly demarcated. The dry and the wet analysis results have been compared for all the parameters. For thin plates, the bending stresses are linearly proportional to the vibratory deflection of the plate. Thus the DLF plots, as a function of τ, set the stress criteria for structural design of marine crafts.

Modal truncation limits are studied for free and forced vibration, by investigating the modal contribution of the first 6x6 = 36 modeshapes. The accuracy of the wet natural frequencies of rectangular plates up to four significant figures has been established. The contribution of higher order modeshapes becomes prominent at high wetting speeds and for softer/massive structures.

The DLF at zero wetting time is evaluated to establish the time-scale limit of the dynamic behavior. For the uniform load, DLF at $\tau = 0$ is the maximum in the DLF plot, while for the impact load, it is the minimum.

5.1 Free wet vibration of square plates.

When the impact force acts for a duration long enough to immerse the whole plate,

and the maximum deflection occurs later in the impact sequence, the fluid inertia *cannot* be ignored. The *radiation forces* have to be included in the governing differential equation for this fluid-structure interaction. Here, the beam is considered to be *deeply* submerged, such that the free surface (*air-water interface*) effects can be ignored. The total excitation force is considered to be a linear superposition of the impact force and the radiation force.

5.1.1 Radiation pressure formulation

The radiation problem is framed as shown in Fig.5.3. The elastic plate is deeply submerged in water and vibrates at all its frequencies. The free surface of the water is not disturbed. The water is considered to be inviscid, incompressible and irrotational. The normal fluid velocity on the elastic plate equals the structural velocity. The normal fluid velocity on the rest of the rigid hull structure is zero.

Fig.5.3 shows the radiation boundary value problem, with AB as the elastic plate, and DA and BC the rigid parts of the hull section, surrounded by fluid on one side. The velocity of the fluid tends to zero at an infinite distance from the plate, which is the semi-circle DC.

The governing differential equation for free, damped, wet vibration of a Kirchhoff's plate is given by Eq.(5.1). The shear deformation and the rotary inertia are ignored, taking into account only the pure bending of the plate. Here m is the mass per unit area of the plate; D is the flexural rigidity and $\mathbf{c}$ the damping.

$$m\frac{\partial Z^2(x,y,t)}{\partial t^2} + \mathbf{c}\frac{\partial Z(x,y,t)}{\partial t} + D\nabla^4 Z(x,y,t) = P_{radiation}(x,y,0,t) \tag{5.1}$$

The radiation pressure is formulated as the *Bernoulli's* pressure, whose linear compo-

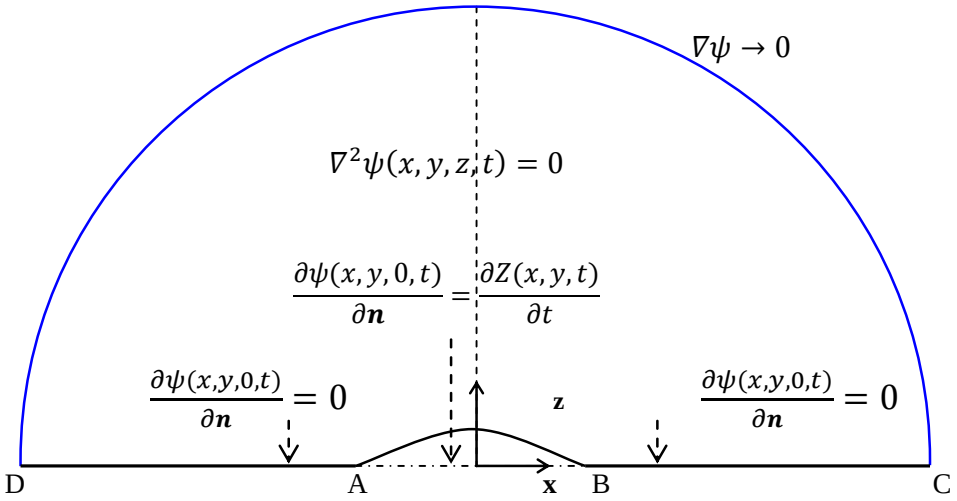

Figure 5.3: Radiation Boundary Value Problem.

nent is considered to act on the plate. (Non-linear terms are ignored).

$$m\frac{\partial Z^2(x,y,t)}{\partial t^2} + \mathbf{c}\frac{\partial Z(x,y,t)}{\partial t} + D\nabla^4 Z(x,y,t) = -\rho_{water}\frac{\partial \Psi(x,y,0,t)}{\partial t}.$$

Assuming modal superposition, the total dynamic deflection is given as a superposition of the modal deflections, given by Eq.(5.2).

$$Z(x,y,t) = \Sigma_{k=1}^{\infty} Z_k(x,y,t) = \Sigma_{k=1}^{\infty} \Phi_k(x,y) q_k(t). \tag{5.2}$$

5.1.1a Boundary Value Problem

The velocity potential is considered to be a linear superposition of an infinite number of modal velocity potentials, given by Eq.(5.3), each of which satisfies the corresponding modal structural equation of motion.

$$\Psi(x,y,z,t) = \Sigma_{k=1}^{\infty} \Psi_k(x,y,z,t) = \Sigma_{k=1}^{\infty} \Psi_k^*(x,y,z)\frac{dq_k(t)}{dt}, \tag{5.3}$$

where $\Psi_k^*(x,y,z)$ is the velocity potential per *unit* modal velocity of the structure.

For the k^{th} modal velocity potential, the governing differential equation in the fluid domain is $\nabla^2\Psi_k^*(x,y,z)=0$, subject to the following boundary conditions.

1) *Body boundary condition on the plate* (No fluid penetration)

$$\Sigma_{k=1}^{\infty}\frac{\partial\Psi_k^*(x,y,0)}{\partial\mathbf{n}}\frac{dq_k(t)}{dt}=\Sigma_{k=1}^{\infty}\Phi_k(x,y)\frac{dq_k(t)}{dt}. \tag{5.4}$$

2) *Boundary condition elsewhere on the structure* (No fluid penetration)

$$\Sigma_{k=1}^{\infty}\frac{\partial\Psi_k^*(x,y,0)}{\partial\mathbf{n}}\frac{dq_k(t)}{dt}=0.$$

3) *Boundary condition at infinity* $\nabla\Psi\rightarrow 0$.

Considering the velocity of the principal coordinates to be orthogonal (linearly independent), the corresponding coefficients of Eq.(5.4) are equated to establish the following time-independent relation:-

$$\frac{\partial\Psi_k^*(x,y,0)}{\partial z}=\Phi_k(x,y). \tag{5.5}$$

5.1.1b Boundary Element Method

Consider the fluid domain of volume V bounded by a surface S. Let $\varphi(x,y,z)$ and $\psi(x,y,z)$ be arbitrary harmonic functions, i.e. they satisfy the Laplace Equation, and have continuous second partial derivatives in the volume V, i.e $\nabla^2\varphi=0$ and $\nabla^2\psi=0$. By Green's second identity, we satisfy:

$$\int\int\int_V\left[\varphi\nabla^2\psi-\psi\nabla^2\varphi\right]d\nabla=\int\int_S\left[\varphi\frac{\partial\psi}{\partial\mathbf{n}}-\psi\frac{\partial\varphi}{\partial\mathbf{n}}\right]dS. \tag{5.6}$$

Putting $\varphi=\Psi$ (the fluid velocity potential), and $\psi=G$ (3-D Green's function), we get

$$\int\int\int_V\left[\Psi_P\nabla^2G_{PQ}-G_{PQ}\nabla^2\Psi_P\right]d\nabla=\int\int_S\left[\Psi_Q\frac{\partial G_{PQ}}{\partial\mathbf{n}_Q}-G_{PQ}\frac{\partial\Psi_Q}{\partial\mathbf{n}_Q}\right]dS_Q,$$

where P = Field point (x,y,z), Q = Source point (ξ,η,ς). The 3D Green's Function at P with respect to Q is given by

$$G(x,y,z;\xi,\eta,\varsigma) = \frac{-1}{4\pi\sqrt{(x-\xi)^2+(y-\eta)^2+(z-\varsigma)^2}}, \text{ such that}$$

$G(x-\xi,y-\eta,z-\varsigma) = 0$ if P $\neq$ Q , and $G(x-\xi,y-\eta,z-\varsigma) = \infty$ if P = Q;

and $\int\int\int_V \nabla^2 G d\nabla = 1.$

Substituting the above in Eq.(5.6), we get

$$\Psi_P = \int\int_S \left[\Psi_Q \frac{\partial G_{PQ}}{\partial \mathbf{n}_Q} - G_{PQ}\frac{\partial \Psi_Q}{\partial \mathbf{n}_Q}\right] dS_Q.$$

Thus the velocity potential at the field point is given as

$$\Psi_P(x,y,z) = \int\int_S \left[\Psi_Q(\xi,\eta,\varsigma)\frac{\partial G_{PQ}(x,y,z;\xi,\eta,\varsigma)}{\partial \mathbf{n}_Q} - G_{PQ}(x,y,z;\xi,\eta,\varsigma)\frac{\partial \Psi_Q(\xi,\eta,\varsigma)}{\partial \mathbf{n}_Q}\right] dS_Q.$$

By defining the appropriate interior problem, we may reduce the above equation to a surface distribution of sources with strength $\sigma_Q(\xi,\eta,\varsigma,t)$.

$$\Psi_P(x,y,z,t) = \int\int_S \sigma_Q(\xi,\eta,\varsigma,t) G_{PQ}(x,y,z;\xi,\eta,\varsigma) dS_Q.$$

The fluid velocity potential is evaluated separately for P $\neq$ Q and for P = Q, i.e.

$$\Psi_P = \int\int_{S-\epsilon} \sigma_Q G_{PQ} dS_Q + \int\int_\epsilon \sigma_Q G_{PQ} dS_Q,$$

where ϵ is defines as the infinitesimal area around the source Q, *located on the plate surface*. Differentiating it with respect to z, the vertical fluid velocity is given as

$$\frac{\partial \psi_P}{\partial z} = \int\int_S \sigma_Q \frac{\partial G_{PQ}}{\partial z} dS_Q = \int\int_{S-\epsilon} \sigma_Q \frac{\partial G_{PQ}}{\partial z} dS_Q + \int\int_\epsilon \sigma_Q \frac{\partial G_{PQ}}{\partial z} dS_Q. \qquad (5.7)$$

For a flat plate, a source located at Q does not induce any vertical velocity at P. Thus the first term in the RHS of Eq.(5.7) is zero. Thus

$$\frac{\partial \Psi_P}{\partial z} = \int\int_{\epsilon} \sigma_Q \frac{\partial G_{PQ}}{\partial z} dS_Q. \tag{5.8}$$

5.1.1c Body Boundary Condition

Now, applying the body boundary condition (BBC) in Eq.(5.4) into Eq.(5.8),

$$\frac{\partial \Psi_P}{\partial z} = \Sigma_{k=1}^{\infty} \frac{\partial \Psi_k^*(\xi,\eta,0)}{\partial z} \frac{dq_k(t)}{dt} = \Sigma_{k=1}^{\infty} \int\int_{\epsilon} \sigma_{Qk}(t) \frac{\partial G_{PQ}}{\partial z} dS_Q \equiv \Sigma_{k=1}^{\infty} \Phi_k(\xi,\eta) \frac{dq_k(t)}{dt} \tag{5.9}$$

The series summation in Eq.(5.9) can be separated into k distinct equations, utilizing the orthogonality of the principal coordinates $q_k(t)$. Thus, for the source Q located at (0,0,0), the k^{th} Body boundary condition in Eq.(5.5) becomes :

$$\frac{\partial \Psi_k^*}{\partial z}(\xi,\eta,0).\frac{dq_k(t)}{dt} = \int\int_{\epsilon} \sigma_{Qk}(t).\frac{\partial G_{PQ}}{\partial z} dS_Q \equiv \Phi_k(\xi,\eta).\frac{dq_k(t)}{dt}. \tag{5.10}$$

As the surface area around the singularity (source) $\rightarrow 0$, the source strength density σ_Q can be assumed to be constant over the area ϵ. Thus Eq.(5.9) becomes ,

$$\Phi_k(\xi,\eta).\frac{dq_k(t)}{dt} = \sigma_{Qk}(t) \int\int_{\epsilon} \frac{\partial G_{PQ}}{\partial z} dS_Q.$$

The 3-D Green's function and its vertical derivative are given as :

$$G(x,y,z;0,0,0) = \frac{-1}{4\pi\sqrt{x^2+y^2+z^2}} = \frac{-1}{4\pi r}, \quad \frac{\partial G(x,y,z;0,0,0)}{\partial z} = \frac{z}{4\pi[\sqrt{x^2+y^2+z^2}]^3}.$$

As $\epsilon \rightarrow 0$, and z$\rightarrow$0, the integral is over a circle of radius R. Substituting the above in Eq.(5.10),

$$\Phi_k(\xi,\eta)\frac{dq_k(t)}{dt} = Lim_{R\rightarrow 0, z\rightarrow 0}\sigma_k(t) \int_0^R \int_0^{2\pi} \frac{\partial G_{PQ}}{\partial z} r dr d\theta = Lim_{R\rightarrow 0, z\rightarrow 0} 2\pi\sigma_k(t) \int_0^R \frac{\partial G_{PQ}}{\partial z} r dr$$

$$= Lim_{R\rightarrow 0, z\rightarrow 0} 2\pi\sigma_k(t) \int_0^R \frac{z r dr}{4\pi[\sqrt{r^2+z^2}]^3} = Lim_{R\rightarrow 0, z\rightarrow 0} 2\pi\sigma_k(t) \frac{z}{4\pi\sqrt{(R^2+z^2)}} = \frac{\sigma_k(t)}{2}.$$

Thus, $$\Phi_k(\xi,\eta)\frac{dq_k(t)}{dt} = \frac{\sigma_k(t)}{2}. \tag{5.11}$$

Thus the source strength can be calculated from the plate modeshape, as given by Eq.(5.11). Substituting Eq.(5.10) and Eq.(5.11) in Eq.(5.3), the k^{th} velocity potential at the field point P(x,y,0), is given as

$$\Psi_k(x,y,0,t) = \Psi_k^*(x,y,0).\frac{dq_k(t)}{dt} = \int\int_S \sigma_{Qk}(t) G_{PQ} dS_Q$$

$$= \int\int_S \left[2\Phi_k(\xi,\eta)\frac{dq_k(t)}{dt}\right] G_{PQ}(x,y;\xi,\eta) dS_Q = \left[\int\int_S 2\Phi_k(\xi,\eta) G_{PQ} dS_Q\right]\frac{dq_k(t)}{dt}$$

$$\text{or} \qquad \Psi_k^*(x,y,0) = \int\int_S 2\Phi_k(\xi,\eta) G_{PQ}(x,y;\xi,\eta) dS_Q. \tag{5.12}$$

5.1.2 Wet vibration formulation : Modal Analysis

The governing differential equation for the free, wet, damped vibration of a Kirchhoff's plate is:

$$\Sigma_{k=1}^{\infty} m\Phi_k(x,y)\frac{d^2q_n(t)}{dt^2} + \Sigma_{k=1}^{\infty}\mathbf{c}\Phi_k(x,y)\frac{dq_n(t)}{dt} + \Sigma_{k=1}^{\infty} D\nabla^4\Phi_k(x,y)q_n(t)$$
$$= P_{radiation}(x,y,0,t) = -\rho_{water}\Sigma_{k=1}^{\infty}\Psi_k^*(x,y,0)\frac{d^2q_k(t)}{dt^2}. \tag{5.13}$$

Lumping the fluid pressure distribution in Eq.(5.13) with the plate inertia to establish a homogeneous second-order linear differential equation yields:

$$\Sigma_{k=1}^{\infty}\left[\rho_{solid} h\Phi_k(x,y) + \rho_{water}\Psi_k^*(x,y,0)\right]\frac{d^2q_n(t)}{dt^2}$$
$$+\Sigma_{k=1}^{\infty} c\Phi_k(x,y)\frac{dq_n(t)}{dt} + \Sigma_{k=1}^{\infty} D\nabla^4\Phi_k(x,y)q_n(t) = 0. \tag{5.14}$$

Substituting Eq.(5.12) into Eq.(5.14) gives

$$\Sigma_{k=1}^{\infty}\left[\rho_{solid} h + \rho_{water}\int\int_S 2\Phi_k(\xi,\eta) G_{PQ} dS_Q\right]\Phi_k(x,y)\frac{d^2q_n(t)}{dt^2}$$
$$+\Sigma_{k=1}^{\infty}\mathbf{c}\Phi_k(x,y)\frac{dq_n(t)}{dt} + \Sigma_{k=1}^{\infty} D\nabla^4\Phi_k(x,y)q_n(t) = 0.$$

Premultiplying Eq.(5.14) by the r^{th} plate modeshape $\Phi_r(x,y)$, and integrating over the surface area LxB of the plate, gives the generalized mass, generalized added mass, generalized damping and generalized stiffness.

$$\int_0^L \int_0^B \Phi_r \Sigma_{k=1}^{\infty} \rho_{solid} h \Phi_k \frac{d^2 q_k(t)}{dt^2} dxdy + \int_0^L \int_0^B \Phi_r \rho_{water} \Sigma_{k=1}^{\infty} \Psi_k^*(x,y,0) \frac{d^2 q_k(t)}{dt^2} dxdy$$
$$+ \int_0^L \int_0^B \Phi_r \Sigma_{k=1}^{\infty} \mathbf{c} \Phi_k \frac{dq_k(t)}{dt} dxdy + \int_0^L \int_0^B \Phi_r \Sigma_{k=1}^{\infty} D \nabla^4 \Phi_k q_k(t) dxdy = 0.$$

The integral of the sum is the sum of the integrals. Thus :

$$\Sigma_{k=1}^{\infty} \left[\int_0^L \int_0^B \Phi_r(x,y) \rho_{solid} h \Phi_k(x,y) dxdy \right] \frac{d^2 q_k(t)}{dt^2}$$
$$+ \Sigma_{k=1}^{\infty} \left[\int_0^L \int_0^B \Phi_r(x,y) \rho_{water} \Psi_k^*(x,y,0) dxdy \right] \frac{d^2 q_k(t)}{dt^2}$$
$$+ \Sigma_{k=1}^{\infty} \left[\int_0^L \int_0^B \Phi_r(x,y) \mathbf{c} \Phi_k(x,y) dxdy \right] \frac{dq_k(t)}{dt}$$
$$+ \Sigma_{k=1}^{\infty} \left[\int_0^L \int_0^B \Phi_r(x,y) D \nabla^4 \Phi_k(x,y) dxdy \right] q_k(t) = 0$$

$$\text{or} \quad \Sigma_{n=1}^{k} (M_{kn} + A_{kn}) \frac{d^2 q_n(t)}{dt^2} + \Sigma_{n=1}^{k} C_{kn} \frac{dq_n(t)}{dt} + \Sigma_{n=1}^{k} K_{kn} q_n(t) = 0; \tag{5.15}$$

where the generalized mass is $M_{kn} = \int_0^L \int_0^B \Phi_k(x,y) \rho_{solid} h \Phi_n(x,y) dxdy$; the generalized added mass is $A_{kn} = \int_0^L \int_0^B \Phi_k(x,y) \rho_{water} \Psi_n^*(x,y,0) dxdy$; the generalized stiffness is $K_{kn} = \int_0^L \int_0^B \Phi_k(x,y) D \nabla^4 \Phi_n(x,y) dxdy$; the generalized damping is $[C] = \zeta [C_{crit}]$; where the modal critical damping is defined as $[C_{crit}] = 2\sqrt{[M][K]}$. Eq.(5.15) is the k^{th} modal governing differential equation of free vibration.

5.1.3 Forced wet vibration

The structural governing differential equation of vibration of the thin plate, with the

impact and radiation forces, is given as :

$$\Sigma_{k=1}^{\infty}\rho_{solid}h\Phi_k(x,y)\frac{d^2q_k(t)}{dt^2}+\Sigma_{k=1}^{\infty}\mathbf{c}\Phi_k(x,y)\frac{dq_k(t)}{dt}+\Sigma_{k=1}^{\infty}D\nabla^4\Phi_k(x,y)q_k(t)$$
$$=P_{impact}(x,y,0,t)+P_{radiation}(x,y,0,t)=P_{total}(x,y,0,t). \tag{5.16}$$

Premultiplying Eq.(5.16) by the r^{th} plate modeshape $\Phi_r(x,y)$, and integrating over the surface area LxB of the plate, gives the set of modal differential equations of motion. The k^{th} modal governing equation is given as :

$$\Sigma_{n=1}^{k}(M_{kn}+A_{kn})\frac{d^2q_n(t)}{dt^2}+\Sigma_{n=1}^{k}C_{kn}\frac{dq_n(t)}{dt}+\Sigma_{n=1}^{k}K_{kn}q_n(t)=gf_k(t). \tag{5.17}$$

The generalized forcing is $gf_k(t)=\int_0^L\int_0^B\Phi_k(x,y)F(x,y,t)dxdy$. This set of equations (Eq.(5.17)) is integrated numerically by stable Euler's implicit-explicit scheme to evaluate the principal coordinates $q_k(t)$ as a function of time. The $q_k(t)$ is then multiplied by the corresponding plate modeshape $\Phi_k(x,y)$ to generate the modal dynamic deflection of the plate. All the modal deflections are superimposed to give the total vibratory displacement of the plate as a function of space and time.

5.2 Wet natural frequencies.

Rewriting Eq.(5.15) in matrix form yields:

$$[M_{kn}]\{\ddot{q}_n(t)\}+[A_{kn}]\{\ddot{q}_n(t)\}+[C_{kn}]\{\dot{q}_n(t)\}+[K_{kn}]\{q_n(t)\}=0. \tag{5.18}$$

The total inertia is given as $[I_{kn}]=[M_{kn}]+[A_{kn}]$. The Eigen values of $[I_{kn}]^{-1}[K_{kn}]$ give the wet natural frequencies $\lambda_{k,wet}$ of the plate, by solving the equation $[K_{kn}]-\lambda_{wet}[I_{kn}]=0$. The Eigen values of $[M_{kn}]^{-1}[K_{kn}]$ had earlier given the dry natural frequencies $\omega_{k,dry}$ of the plate, by solving $[K_{kn}]-\lambda_{dry}[M_{kn}]=0$. The decrease in frequency is accounted

by the increase in total inertia of the system. Combining the above equations, we get $\lambda_{dry}[M_{kn}] = \lambda_{wet}[I_{kn}]$. Fig.5.4 shows the generalized added mass of a CCCC plate for

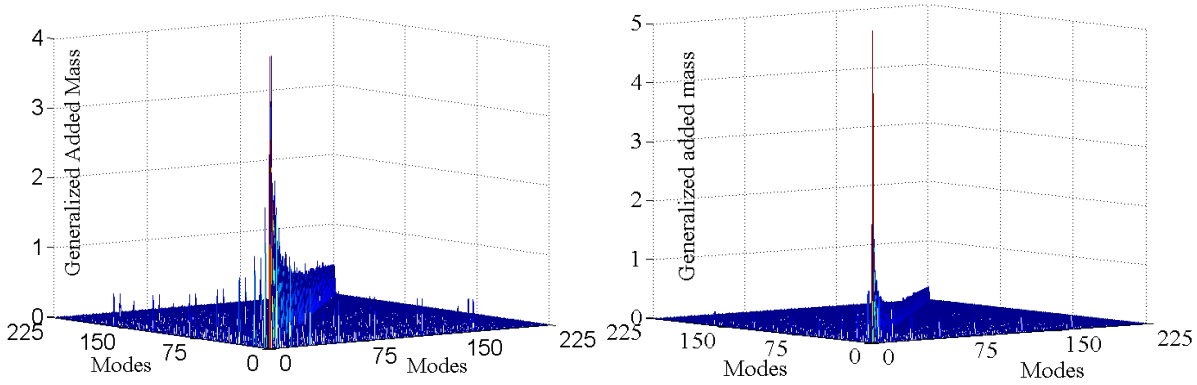

Figure 5.4: Generalized Added Mass for CCCC and SSSS plates with 15x15 = 225 plate modeshapes.

the first 15x15 = 225 modeshapes, with 20x20 = 400 panels. It is seen that the diagonal term A_{kk} is (much) larger than the non-diagonal terms A_{kn}.

Table 5.1 shows the fundamental wet natural frequency of a CCCC plate and the corresponding NAVMI factor, tabulating their convergence with respect to the number of panels and the number of mdoeshapes. The frequency is seen to converge to the first four significant figures, and the NAVMI factor for the first three significant figures. This analysis is used for 10x10 = 100 modes with a 20x20 = 400 panels. Since the mass matrix is diagonal and the added mass matrix shown is almost diagonal(Fig.5.4), we can approximately write,

$$\lambda_{k,wet} \cong \lambda_{k,dry}\frac{M_{kk}}{I_{kk}} \quad or \quad \omega_{k,wet} = \omega_{k,dry}\sqrt{\frac{M_{kk}}{I_{kk}}} \quad or \quad \omega_{k,wet} = \frac{\omega_{k,dry}}{\sqrt{1+\frac{A_{kk}}{M_{kk}}}}. \tag{5.19}$$

The wet natural frequencies (Eq.(5.19)) are non-dimensionalized by $\sqrt{D/(mL^4)}$,

Modes	6 x 6	= 36	10 x 10	= 100	15 x 15	= 225	20 x 20	= 400
Panels	**Wet freq**	**NAVMI**	**Wet freq**	**NAVMI**	**Wet freq**	**NAVMI**	**Wet freq**	**NAVMI**
2 x 2	1.3807E+01	0.4438	1.3620E+01	0.4581	1.3533E+01	0.4650	1.3518E+01	0.4662
3 x 3	1.5002E+01	0.3642	1.4979E+01	0.3655	1.4938E+01	0.3679	1.4925E+01	0.3687
4 x 4	1.5276E+01	0.3486	1.5149E+01	0.3556	1.5137E+01	0.3562	1.5135E+01	0.3564
5 x 5	1.5233E+01	0.3510	1.5187E+01	0.3534	1.5182E+01	0.3537	1.5177E+01	0.3539
10 x 10	1.5177E+01	0.3541	1.5174E+01	0.3542	1.5173E+01	0.3542	1.5171E+01	0.3543
15 x 15	1.5164E+01	0.3548	1.5160E+01	0.3549	1.5160E+01	0.3549	1.5160E+01	0.3549
20 x 20	1.5159E+01	0.3551	1.5155E+01	0.3552	1.5155E+01	0.3552	1.5155E+01	0.3552
25 x 25	1.5157E+01	0.3553	1.5153E+01	0.3554	1.5152E+01	0.3554	1.5152E+01	0.3554
30 x 30	1.5155E+01	0.3553	1.5151E+01	0.3554	1.5151E+01	0.3554	1.5151E+01	0.3554
40 x 40	1.5154E+01	0.3554	1.5150E+01	0.3555	1.5150E+01	0.3555	1.5150E+01	0.3555

Table 5.1 Convergence of the non-dimensional fundamental wet natural frequency and NAVMI factor of a square CCCC plate.

to generate the Non-D $\omega_{k,wet}$. Now $M_{kk} = \int_0^L \int_0^B \Phi_k(x,y) m \Phi_k(x,y) dxdy$, and $A_{kk} = \int_0^L \int_0^B \Phi_k(x,y) \rho_{water} \Psi_k^*(x,y,0) dxdy$, which gives the ratio of the fluid kinetic energy to the solid kinetic energy in Eq.(5.20) as follows :

$$\frac{A_{kk}}{M_{kk}} = \left[\frac{\rho_{water} L}{\rho_{solid} h}\right] \left[\frac{\frac{1}{L}\int_0^L \int_0^B \Phi_k(x,y)\Psi_k^*(x,y,0)dxdy}{\int_0^L \int_0 \Phi_k(x,y)\Phi_k(x,y)dxdy}\right] = \left[\frac{\rho_{water} L}{\rho_{solid} h}\right] * NAVMI. \quad (5.20)$$

This ratio is also *added mass coefficient* C_a of the k^{th} plate modeshape. This coefficient (Eq.(5.21)) varies with the densities of the solid and the fluid, and the thickness of the plate. The part of the ratio that depends on the plate modeshape is called the **N**on-dimensional **A**dded **V**irtual **M**ass **I**ncrement (NAVMI) factor; and it is defined as

$$\left[\frac{\frac{1}{L}\int_0^L \int_0^B \Phi_k(x,y)\Psi_k^*(x,y,0)dxdy}{\int_0^L \int_0^B \Phi_k(x,y)\Phi_k(x,y)dxdy}\right]. \quad (5.21)$$

It is a function of the plate modeshape, i.e. it depends on the boundary conditions and the aspect ratio α of the plate. It is a constant for a given plate modeshape, and hence if the NAVMI factor (Eq.(5.22)) is known, the C_a can be estimated from Eq.(5.20).

Table 5.2 shows that the CCCC plate is the stiffest while the SSSS plate is the softest, vibrating in contact with water. Table 5.3 shows that the NAVMI factors increase with increasing aspect ratio for all the boundary conditions. For CCCC and SSSS plates, aspect ratios $\alpha = \mathbf{a}$ and $\alpha = 1/\mathbf{a}$ would have the same set of NAVMI factors. For the mixed boundary conditions, the CSCS plate with $\alpha = \mathbf{a}$ and the SCSC plate with $\alpha = 1/\mathbf{a}$ would have the same set of NAVMI factors.

	CCCC		**SSSS**		**CSCS/SCSC**	
k	Non-D $\omega_{k,wet}$	NAVMI	Non-D $\omega_{k,wet}$	NAVMI	Non-D $\omega_{k,wet}$	NAVMI
1	15.15	0.355	7.824	0.410	11.84	0.381
2	41.49	0.163	26.82	0.182	30.06	0.177
3	41.49	0.163	26.82	0.182	38.85	0.167
4	67.61	0.119	47.81	0.132	58.22	0.125
5	80.33	0.129	59.64	0.133	63.20	0.123
6	85.01	0.108	62.08	0.116	80.65	0.119
7	110.9	0.093	84.40	0.100	93.11	0.097
8	110.9	0.093	84.40	0.100	103.1	0.096
9	144.5	0.086	113.8	0.089	115.9	0.088
10	144.5	0.086	113.8	0.089	139.8	0.079
11	155.5	0.077	123.0	0.082	142.6	0.084
12	171.8	0.075	137.8	0.080	145.8	0.079
13	174.0	0.073	139.2	0.077	166.3	0.075
14	218.8	0.064	179.0	0.068	186.3	0.071
15	218.8	0.064	179.0	0.068	194.1	0.066
16	221.5	0.072	183.3	0.073	204.8	0.066

Table 5.2 Non-Dimensional wet natural frequencies and NAVMI factors of Square plates.

α	**1**	**2**	**3**	**4**	**5**	**10**
CCCC	0.355	0.492	0.583	0.649	0.700	0.855
SSSS	0.410	0.564	0.646	0.732	0.796	0.996
CSCS	0.381	0.536	0.622	0.726	0.796	1.128
SCSC	0.381	0.515	0.598	0.664	0.714	0.920

Table 5.3 Fundamental NAVMI Factors (k = 1) for plates of 6 aspect ratios.

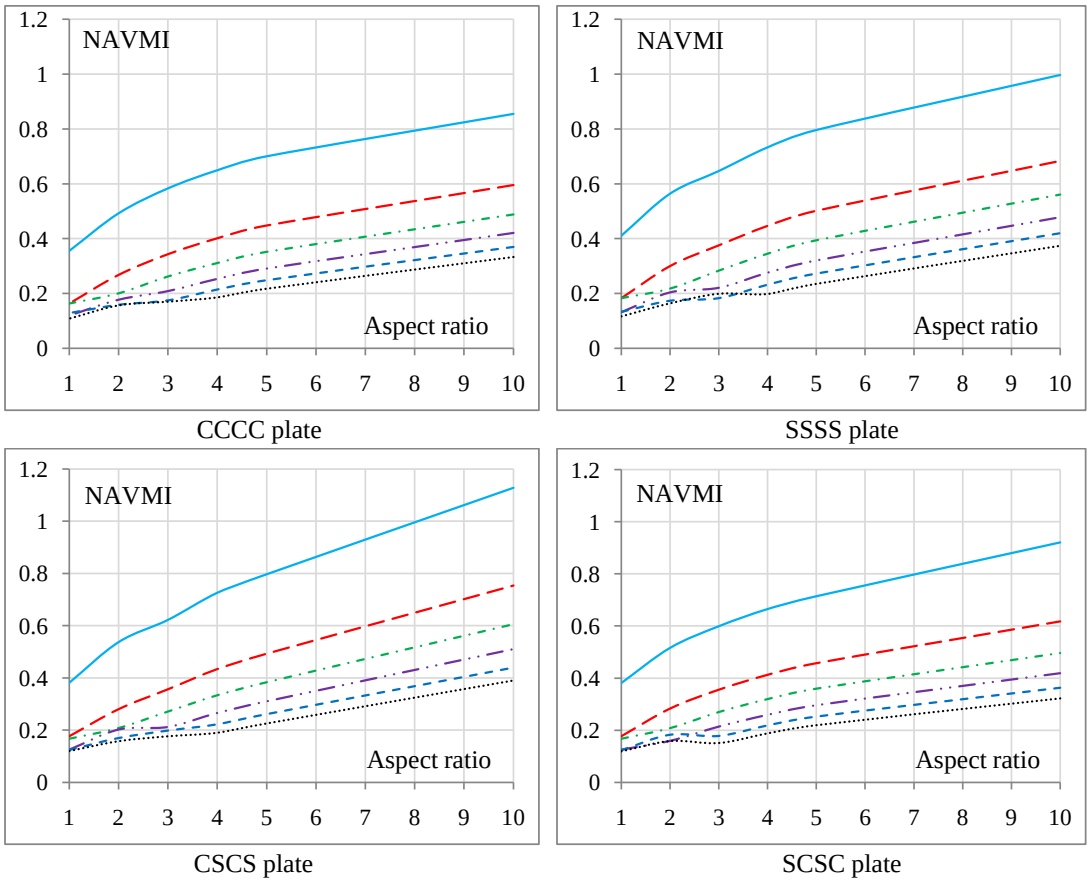

NAVMI factors for the first six modeshapes for *Rectangular* plates (a) CCCC plate, (b) SSSS plate, (c) CSCS plate, (d) SCSC plate. Modeshape bar code : (1), (2), (3), (4), (5), and (6).

Figure 5.5: NAVMI factors for the first six modeshapes for Rectangular plates.

The added mass associated with the fundamental modeshape is the highest, and it decreases with the higher-order modeshapes; e.g for a CCCC square plate, the 4th modeshape NAVMI factor is only ∼33.5% and the 9^{th} modeshape NAVMI factor is only ∼ 24% of the fundamental NAVMI factor. This is because the volume enclosed under the 3D plate modeshape decreases with higher modes. Also, the boundary conditions seem to have a less and less influence on the NAVMI magnitude with increasing modeshape index. Fig.5.5 shows the NAVMI factors for four boundary conditions, the first six modeshapes, and over a range of aspect ratios. The trends are seen to be similar for all boundary conditions and modes.

5.3 Dynamic response of plates to Uniform Stretching Load.

A uniform load of unit magnitude stretches across the plate at a speed of V. The plate is set into small-amplitude flexural vibrations, which are analyzed by the modal analysis methodology. The dynamic load factor (DLF) is plotted against the non-dimensionalized wetting time given as

$$\tau_{wet} = \left(\frac{L}{V}\right)\frac{\omega_{1,wet}}{2\pi}\sqrt{1-\zeta^2}, \quad \text{as opposed to} \quad \tau_{dry} = \left(\frac{L}{V}\right)\frac{\omega_{1,dry}}{2\pi}\sqrt{1-\zeta^2}, \qquad (5.22)$$

for the four different boundary conditions and two damping ratios. Comparing the dry and the wet vibration analysis:

(a) **Dry Vibration** uses the (i) dry natural frequencies and the (ii) impact pressure. The governing differential equation is non-dimensionalized by plate inertia $m\omega_{dry}^2$, and is numerically integrated with the time-step Δt_{dry} as the independent variable.

(b) **Wet Vibration** uses the (i) wet natural frequencies and the (ii) impact pressure augmented by the radiation pressure. The radiation pressure is lumped together with

the structural mass inertia term on the left hand side of the governing differential equation, which is non-dimensionalized by total (plate + fluid) inertia $(m + a)\omega_{wet}^2$, and is numerically integrated with the time-step Δt_{wet} at the independent variable.

5.3.1 Wet Dynamic Loading Factor.

Fig.5.6 and Fig.5.7 shows the dynamic loading factor (DLF) of the wet vibration square plates, under the uniform stretching load, for zero damping and 50% damping, respectively. The trends are similar to the *dry* plate vibration analysis results, detailed in Chapter 4.

The following interpretations are reiterated :

(a) Damping reduces the amplification factor, thereby decreasing the peak DLF. Damping also smooths the DLF characteristic in the quasi-static zone, and also at very small values of τ; where the DLF becomes a function of the record length due aperiodicity in the time-series of the deflection, owing to the increased presence of the higher-order modeshapes.

(b) The CCCC and the CSCS plate behave almost similarly, while the SSSS and the SCSC plates behave nearly identically. This shows that the beam modeshape parallel to the direction of the forcing is important in determining the dynamic response, and the modeshapes perpendicular to the direction of the forcing are not important.

(c) The CSCS response diverges from the CCCC response, and the SCSC diverges from the SSSS response, only at very low τ (Eq.5.24). In this dynamic response region, the CSCS and the SCSC responses approach each other, because the orientation of the plate becomes immaterial to the forcing direction at very high impact speeds.

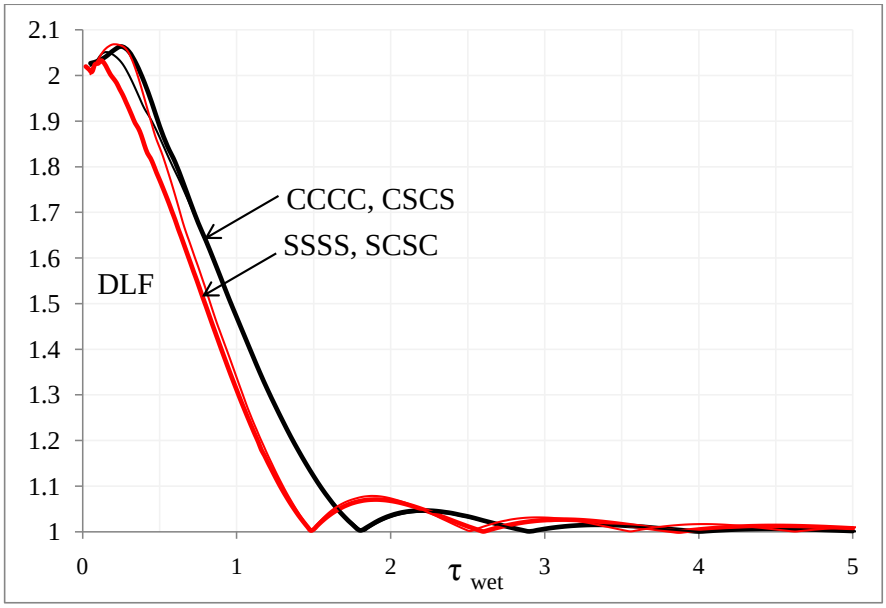

Figure 5.6: Wet DLF of square plates without damping.

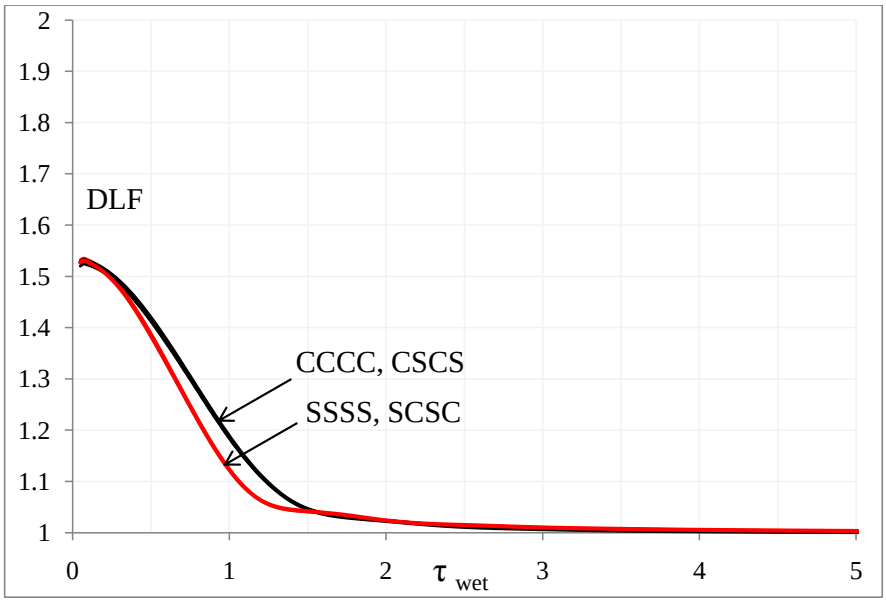

Figure 5.7: Wet DLF of square plates with 50% damping.

Fig.5.8 shows the dry and wet DLFs of square plates with all the four boundary conditions. There is hardly any difference between the DLF evaluated by the dry analysis and the wet analysis. The dry DLF is plotted against the dry non-dimensional wetting time $\tau_{dry} = T_{sp}\frac{\omega_{1,dry}\sqrt{1-\zeta^2}}{2\pi}$, and the wet DLF is plotted against the wet non-dimensional wetting time $\tau_{wet} = T_{sp}\frac{\omega_{1,wet}\sqrt{1-\zeta^2}}{2\pi}$. This demonstrates that dry and the wet analysis are almost identical, when different time-scales are used. The two analyses show approximately self-similar results.

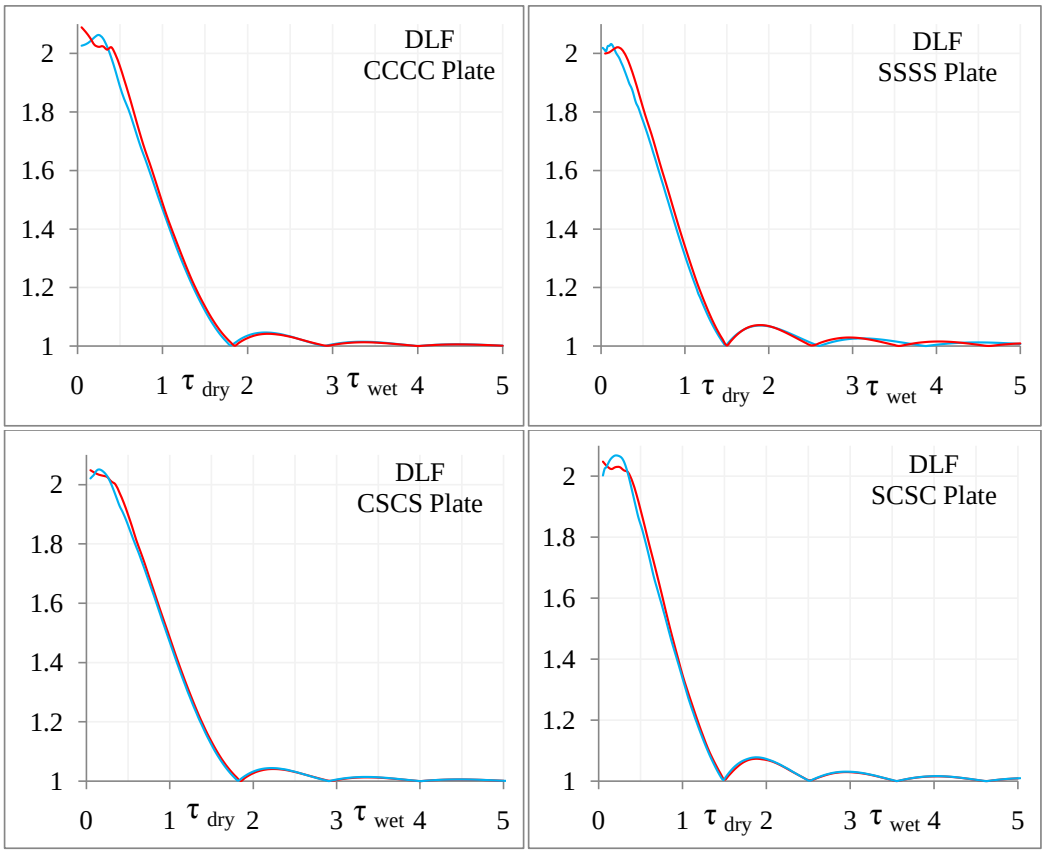

Figure 5.8: Dry DLF vs. Wet DLF of (a) CCCC plate, (b) SSSS plate, (c) CSCS plate, (d) SCSC plate, subject to Uniform stretching load.

5.3.2 Relative Modal Contribution.

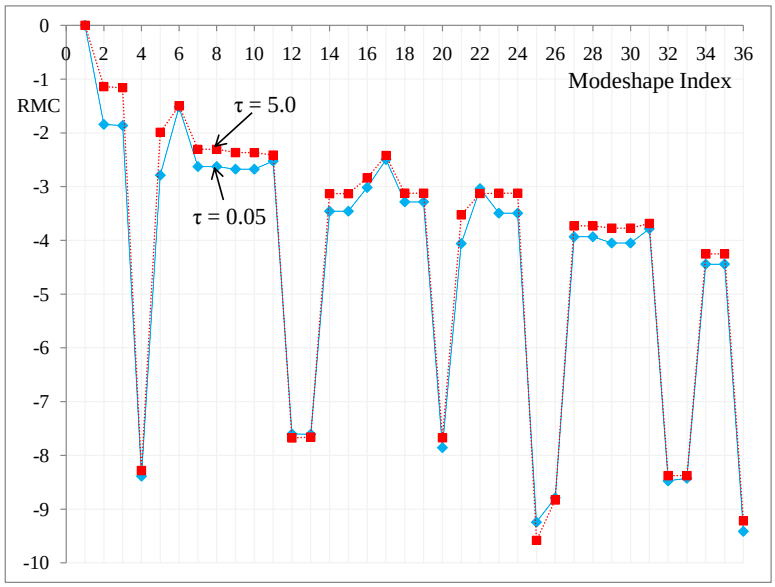

Figure 5.9: RMC for a CCCC square plate subject to uniform loading, at two different wetting times : $\tau = 0.05$ and $\tau = 5$.

Fig.5.9 shows the Relative Modal Contribution (RMC) of the 6x6 = 36 modeshapes of a square CCCC plate, subject to uniform loading at two different speeds, i.e. at $\tau = 0.05$ (*dynamic zone*) and $\tau = 5$ (*quasi-static zone*). Inclusion of the first 36 modeshapes ensures that all the contributing higher-order modeshapes (k > 36) are at least 4 orders of magnitude below the fundamental modeshape contribution, or even less. E.g., it is seen the k = 34, 35 have contribution less than 10^{-4} times the fundamental principal coordinate. Hence the modeshapes higher than k = 36 can be ignored within the limits of engineering accuracy. Repeated frequencies have identical modeshapes, and hence show equal contribution, e.g. k = 2 and k = 3. Those modeshapes which are primarily defined by the even beam modeshapes have the minimum contribution, e.g., k = 4, 12,

13, 20. This is because the forcing configuration predominantly excites the odd beam modeshapes in either direction.

5.4 Dynamic response of plates to Impact Load.

The hydroelastic analysis of the plate to the uniform stretching load helps establish the benchmarks of the results, i.e. the time-scales, the DLF, and the RMC. Now we advance to the more realistic model of the impact transient force distribution, defined by a moving jet head, stretching from the keel ($x' = 0$) upwards. The maximum pressure is a function of the vertical impact velocity V and the deadrise angle β.

5.4.1 Dynamic Loading Factor.

Fig.5.10 shows the wet vibration DLF of square CCCC and SSSS plates, at four different deadrise angles, i.e. β = 1, 5, 15 and 30 degrees. The wet and the dry DLFs are again, almost identical. The details of the plots have been explained in Section 4.3.1. The dry DLF is plotted with respect to the dry non-dimensionalized wetting time τ_{dry}, while the wet DLF has been plotted with respect to the wet non-dimensionalized wetting time τ_{wet} (Eq.(5.22)).

Fig.5.11 shows that the DLF characteristics of rectangular CCCC plates subject to impact loading at a deadrise angle of β = 1 degree, for three different aspect ratios α = 10, 2 and 0.2, under wet vibration analysis, are nearly the same as that under dry vibration analysis. The solid lines are the Dry DLF results, while the dashed ones are the Wet DLF results.

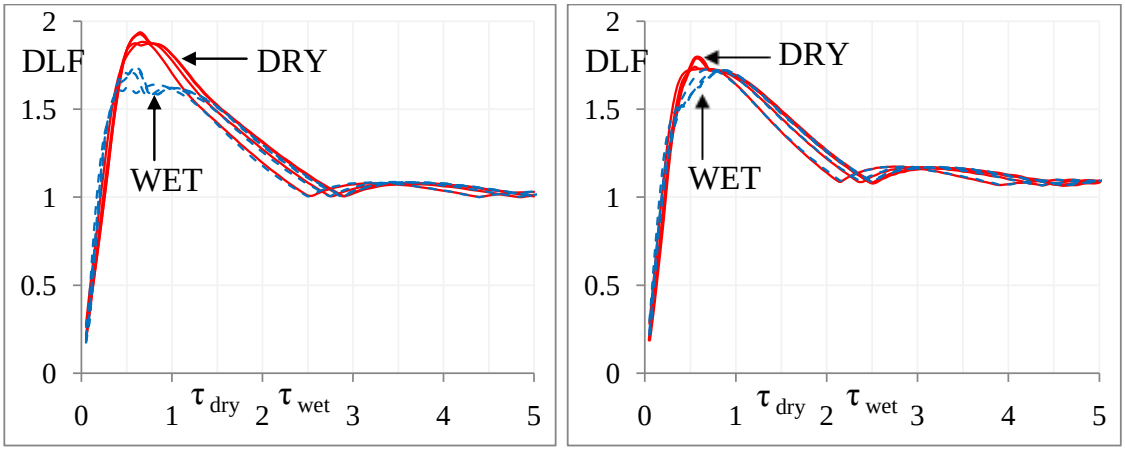

Figure 5.10: Dry and wet undamped DLF of square (a) CCCC and (b) SSSS plates at $\beta = 1$, 5, 15, 30 degrees.

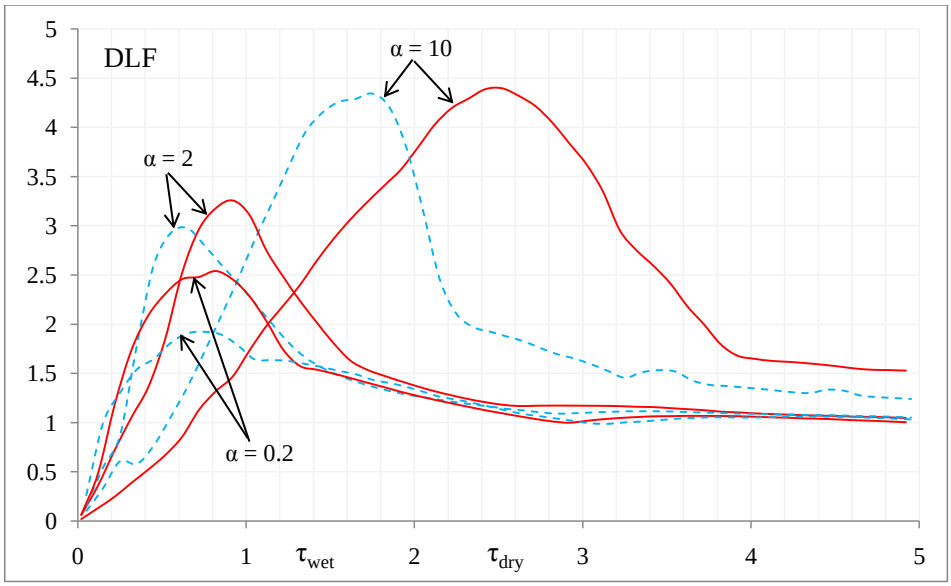

Figure 5.11: Dry and wet undamped DLF of rectangular CCCC plates at $\beta = 1$ degree, $\alpha = 10$, 5, and 0.2.

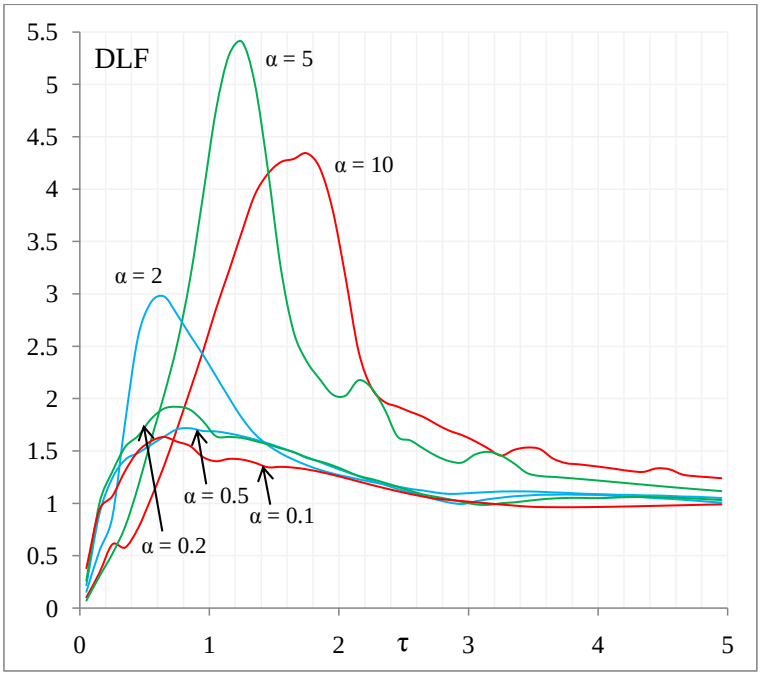

DLF of rectangular plates to impact load at β = 1 degree.

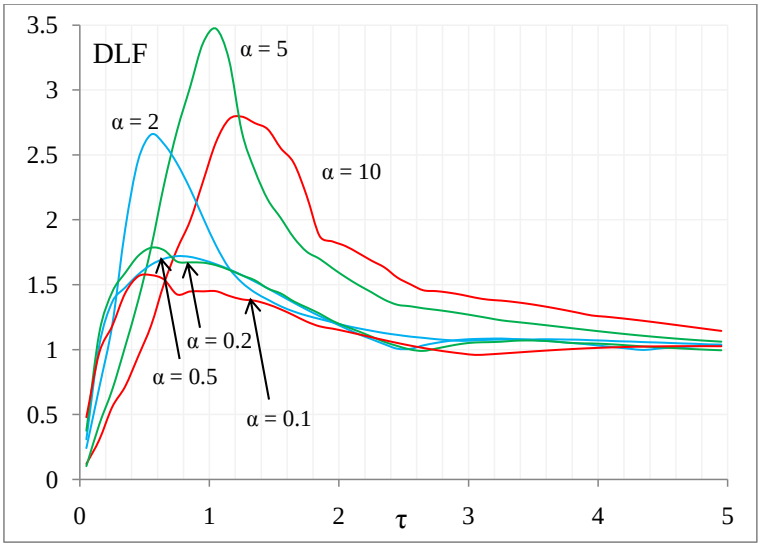

DLF of rectangular plates to impact load at β = 30 degree.

Figure 5.12: Wet DLF of rectangular CCCC plates for impact forcing, at six(6) aspect ratios, and two(2) deadrise angles $\beta = 1$, 30 degrees, and zero damping.

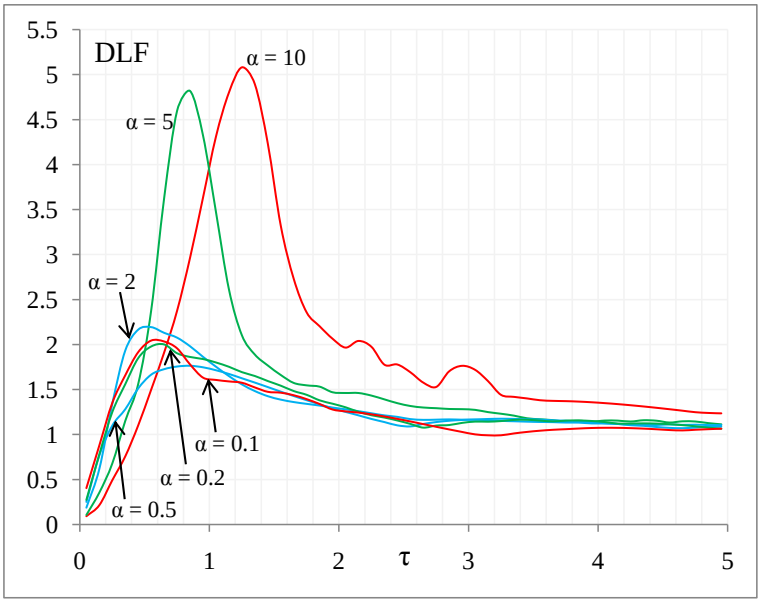

DLF of rectangular plates to impact load at β = 1 degree.

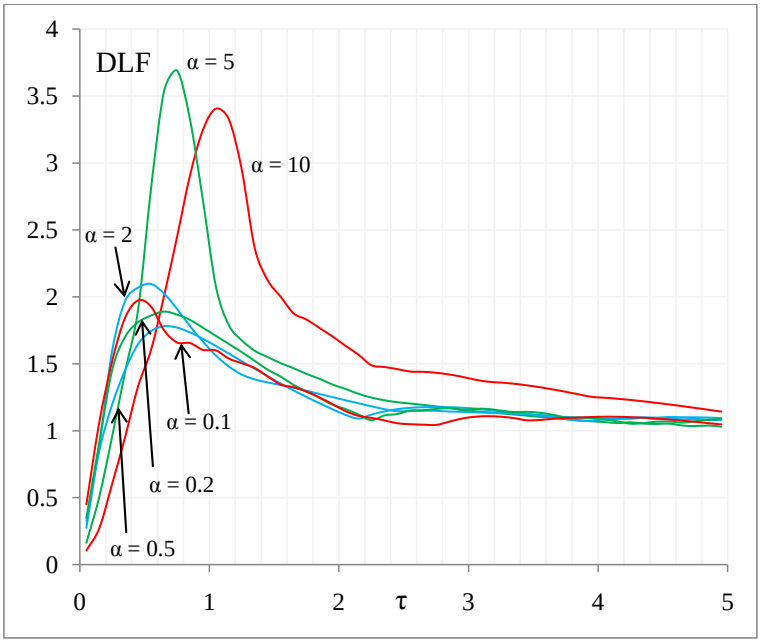

DLF of rectangular plates to impact load at β = 30 degree.

Figure 5.13: Wet DLF of rectangular SSSS plates for impact forcing, at six(6) aspect ratios, and two(2) deadrise angles $\beta = 1$, 30 degrees, and zero damping.

Fig.5.12 and Fig.5.13 shows the DLF of CCCC and SSSS plates at $\alpha = \mathbf{0.1}$, $\mathbf{0.2}$, $\mathbf{0.5}$, $\mathbf{2}$, $\mathbf{5}$, and $\mathbf{10}$; in response to impact loads at $\beta = 1$ and 30 degrees. They reacts almost similarly, in response to impact loads, with the $\alpha < 1$ plates having DLFs restricted to 2 and below. Plates with $\alpha > 1$ produce much larger DLFs, with a smaller deadrise angle β producing more severe dynamic deflections and bending stresses.

5.4.2 Relative Modal Contribution.

Fig.5.10. below shows the relative modal contribution of the first 6x6 = 36 modeshapes of a square CCCC plate, subject to impact loading at a deadrise angle of $\beta = 1$ degree, at two different wetting times, i.e. $\tau = 0.05$ and $\tau = 5$. The higher the wetting speed, the more is the likelihood of a higher-order modeshape being excited. We find RMC at $\tau = 0.05$ is higher than that at $\tau = 5$. So the truncation limit is enough to meet the accuracy criterion for the response at $\tau = 5$ (below 10^{-3}), but not for the response at $\tau = 0.05$ (above 10^{-3}).

5.5 Discussion

This chapter presents the wet vibration of elastic plates in contact with water on one side. The boundary value problem has been framed, with the elastic plate as a part of an infinite rigid plate, with air on one side and water on the other. The external pressure is augmented by the fluid radiation pressure, altering time-scales of the problem. The body boundary condition, i.e. *the fluid velocity at the fluid-structure interface is equal to the structural velocity*, is used to generate the relation between the plate modeshape and the source density, using flat constant-strength panels.

The free wet vibration analysis yields the wet natural frequencies, modal added

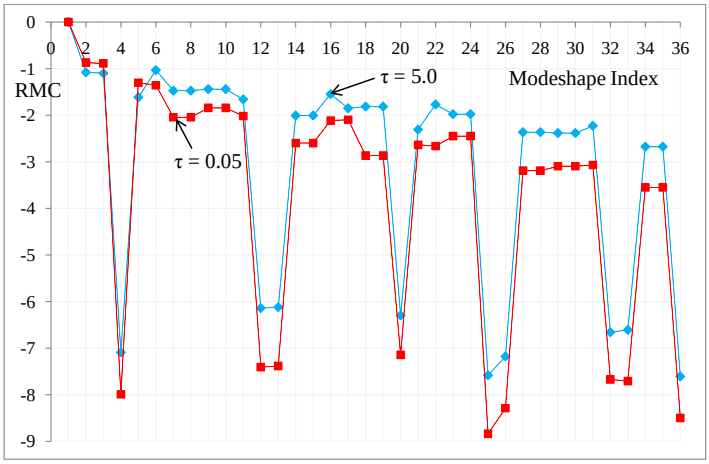

Figure 5.14: RMC for beta = 1 degree for a CCCC *square* plate, subject to impact loading, at two wetting times, i.e. $\tau = 0.05$ and $\tau = 5$.

masses, and the NAVMI factors for rectangular plates with three different boundary conditions. Their convergence with respect to both the number of modes and panels have been studied.

Proceeding to the forced vibration, the dry and the wet analyses of the uniform stretching load-induced vibration generate nearly identical DLF characteristics, provided the times-scale normalizations are done correspondingly, i.e. the wetting time is non-dimensionalized by the dry and wet fundamental period of the plate for the dry and wet analysis, respectively. The Relative Modal Contribution (RMC) and the modal truncation limits of the plates also remain the same.

The impact-induced response analyses produce similar results for dry and wet vibration, except for the peak DLF. Wet vibration in impact loading excites more modes. The response characteristics superpose over each other, reiterating the approximate self-similarity between the dry and the wet vibration analysis methodology.

CHAPTER VI

CONCLUSIONS AND FUTURE RESEARCH

6.1 Discussion and Conclusions.

To summarize, the numerically efficient Modal analysis has been used to study the dynamic elastic response of Kirchhoff's plates, subject to transient hydrodynamic impact loads. This is useful for marine structural designers, who typically conduct a static analysis, and thus, need the **Dynamic Loading Factor** (DLF) as a *safety factor* to accommodate for the dynamic stresses generated due to the severe hydrodynamic impacts. The severity of the slam may be misunderstood as the magnitude of the hydrodynamic load on a *rigid* structure; but it is far more relevant to express this severity with respect to the *flexural* stresses generated in the structure in response to the slam. A very high impact pressure of ∼8205 N, at a deadrise of $\beta = 1$ degree, may appear dangerous; *but* it produces an extremely small flexural deflection at $\tau \approx 0$.

The time-scales of the problem incorporate a wide range of magnitudes of deadrise angles, damping ratios, aspect ratios, and four boundary conditions (end fixities). Thus the designer is given a variety of parameters to choose from, may estimate the τ by coalescing all the time-scales, and subsequently determine the corresponding DLF.

For example, a square CCCC plate of side length 1 m, impacting against the water at 20 m/sec, has a wetting time of 0.05 sec under the assumption of uniform loading model. With a thickness of 3 mm, a density of 7850 kg/m^3, Young's modulus of 209 GPa, and a Poisson's ratio of 0.3, the plate has a fundamental natural period of 0.037 sec. Thus $\tau = 1.34$, and the corresponding undamped DLF ≈ 1.25, i.e. the dynamic deflection

and stresses are 25% above those calculated by the static analysis. A SSSS plate with the same parameters and properties has $\tau = 0.74$, and a corresponding undamped DLF ≈ 1.57, i.e. the dynamic deflection and stresses are 57% above those calculated by the static analysis.

The **details** of the summary are tabulated as follows:

1. This Normal Mode analysis study provides a comprehensive estimate of the DLF, bypassing the computationally intensive FEA.

2. A part of the above effort was concentrated in the study of the *free vibration* of the plate. The Governing Differential Equation (GDE) of free vibration cannot be factorized into two independent equations in x and y. The natural dry frequencies of rectangular plates have been determined to 5 significant figures (Table 4.2 and Table 4.3), and wet natural frequencies have been determined to 4 significant figures (Table 5.2). Modal truncation studies have been utilized to improve the accuracies of both free and forced vibrations (Table 4.1).

3. Galerkin′s method was used to estimate the *admissible functions* and their weights, i.e. the relative contributions of all the modeshapes at a particular natural frequency (Table 4.4). The corresponding static deflection was also calculated similarly, at each location and time step.

4. *Damping* compresses the time scale, stunts the DLF peak by reducing the dynamic amplification, and evens out the intermittent quasi-static responses. It also reduces (almost removes) the ambiguity of the DLF magnitude at low values of τ, when the DLF becomes a function of the record length of the time-series of the dynamic deflection (in the numerical analysis) (Fig.4.3).

5. $0.7 < \tau < 2.5$ is the usual *region of interest* for practical ship-designers, given the material properties of the vessel and the most probable impact speeds. The DLF characteristic in this region (and beyond) has been clearly established for the selected parameter space (Fig.4.6 and Fig.4.7).

6. The influence of the different parameters like aspect ratios, boundary conditions, damping ratios, and the deadrise angle into the *time scale* have been combined into a single parameter τ.

7. The SS and the CC end conditions represent the two extremes of *end fixities* (0% and 100%), and the mixed end conditions are found to respond within the band of responses bordered by the SSSS and CCCC boundary conditions. The bending moments generated by the flexural deflection depend on the end fixities of the plate, which lie in between the above two fixities.

8. *Asymptotic behavior* of the DLF at zero splash time has been studied, when the hydrodynamic load is assumed to act on the structure instantaneously. It gives the maximum possible DLF of the structure due to the uniform stretching load; and the minimum possible DLF due to the impact loading (Table 4.5 and Table 4.7).

9. The *wet vibration* analysis results have been compared to those of the dry vibration analysis, illustrating the fact that non-dimensionalization of time-scales almost self-similarizes the Dynamic Load Factor (DLF) over the range of wetting speeds and material properties.

6.2 Future Research.

1. *Stiffening of the plate.* The marine vessel is made of stiffened panels, which are subject to hydrodynamic impact loads. This study assumes the mass and stiff-

ness distribution to be independent of space. Stiffening changes the mass and stiffness distributions of the panel, both which influence its natural frequency of vibration.

2. *Two-way coupling between the fluid and the structure.* The structural deflection itself influences and alters the pressure field, modifying the excitation force. The two-way coupling studies the pressure-velocity interaction at the fluid-solid interface, satisfying the body-boundary-condition (BBC) at all times, and generates the structural deflection and the hydrodynamic pressure simultaneously as a function of time, given the changing wetted surface of the structure (partial wetting).

3. *Waves instead of calm water.* This analysis uses a constant vertical velocity V. In reality, the vertical impact velocity is a function of time, subject to the velocity of the free surface of water, and also the extent of immersion of the craft. In an irregular sea, if the most probable wave frequency equals the frequency of the structure, it leads to temporal resonance. If the most probable wavelength aligns with the modeshape of the structure, it leads to spatial resonance. The vertical impact velocity and the probability/frequency of slamming, is collectively determined by the most probable wave height, the wave frequency, the vessel speed and the heading direction.

4. *Dynamic response to repeated impulsive loadings in a stochastic seaway.* Slamming occurs repeatedly in a seaway. This analysis considered the impact load being applied just *once* on the structure. Repeated hydrodynamic loads produce cumulative impact pressures, cumulative deflections, and thus, cumulative bending stresses. If a subsequent slam occurs when the structure is already flexed due to the previous slam, the deflections might be large, whose analysis would be beyond the scope of the Kirchhoff's plate model.

APPENDIX 1

Beam Modeshape Formulation for Clamped-Clamped End Conditions

The free vibration equation of motion for the beam, ignoring gravity, is

$$m\frac{d^2Z(x,t)}{dt^2} + EI\frac{d^4Z(x,t)}{dx^4} = 0.$$

The modeshape are the Eigen vectors of the above equation.

$$\phi_j(x) = A1_j cos(\gamma_j x) + A2_j sin(\gamma_j x) + A3_j cosh(\gamma_j x) + A4_j sinh(\gamma_j x).$$

where $\gamma_j = \omega^2_{j,dry}(m/EI)$ are the corresponding Eigen values. The four constants A1, A2, A3 and A4 are calculated from the four boundary conditions of the beam, i.e.

$$Z(0,t) = Z(L,t) = 0; \frac{dZ(0,t)}{dx} = \frac{dZ(L,t)}{dx} = 0 \text{ for a Clamped} - \text{Clamped beam}$$

There are an infinite number of distinct values of γ_j, each of which corresponds to distinct natural frequencies ω_j and modeshapes $\phi_j(x)$. The CC modeshape is

$$\phi_j(x) = \cos(\gamma_j x) - \cosh(\gamma_j x) - \sigma_j \sin(\gamma_j x) + \sigma_j \sinh(\gamma_j x),$$
$$\text{where} \quad \sigma_j = \frac{\cos(\gamma_j L) - \cosh(\gamma_j L)}{\sin(\gamma_j L) - \sinh(\gamma_j L)}$$

Substitution of the BCs into the modeshape leads to $\cos(\beta_j L)\cosh(\beta_j L) = 1$. The different values of β_j calculated by the Newton-Raphson method, with the error less than 10^{-15}.

Index(j)	γ	σ
1	4.730040744862704	0.982502214576238
2	7.853204624095838	1.000777311907269
3	10.995607838001671	0.999966450125409
4	14.137165491257464	1.000001449897657
5	17.278759657399480	0.999999937344383
6	20.420352245626059	1.000000002707595
7	23.561944902040455	0.999999999882994
8	26.703537555508188	1.000000000005056
9	29.845130209103253	0.999999999999782
10	32.986722862692822	1.000000000000000

The higher order wave numbers are given as $\gamma_j = (2j+1)\pi/2$.

For j > 5, the exact modeshape is given by :

$$\phi_j(x) = e^{-\beta_j x} - \cos(\beta_j x) + [1+\nu]\sin(\beta_j x) - \nu\sinh(\beta_j x),$$
$$\text{where} \quad \nu = \frac{e^{-\beta_j L} - \cos(\beta_j L) + \nu\sin(\beta_j L)}{\sinh(\beta_j L) - \sin(\beta_j L)}$$

Calculation of γ_j determines ϕ_j and the dry natural frequencies of the beam ω_j.

APPENDIX 2

Impact Load Formulation

The numerical formulation of the impact forcing are done as follows :-

1) Select deadrise angle β and set τ.

2) Calculate Splash time by multiplying τ with the fundamental period of the plate, i.e.

$$T_{sp} = \tau \left[\frac{\omega_{1,dry}}{2\pi} \right].$$

3) Set Time-step : $\Delta t = \frac{T_{sp}}{N}$, where N is spatial discretization along the length L. (Δx = $\frac{L}{N}$). Also, set counters for both space and time steps, i.e. x = (i-1)Δx, for i = 1 through N+1, and t = (k-1)Δt, for k = 1 through T, where T is the number of time steps.

4) Non-dimensionalize the time-step : $\Delta t' = \omega_{1,dry}\ \Delta$t.

5) Calculate the speed of the wetting along the plate = $V_{along} = \frac{L}{T_{sp}}$.

6) Calculate $\dot{d}(t) = V_{along} \cos(\beta)$, which is the speed of the jet head translation. This also gives the vertical impact velocity

$$V = \dot{d}(t) \frac{2 \tan(\beta)}{\pi}.$$

7) Calculate the stagnation pressure of the vertical impact velocity

$$P_{stagnation} = \frac{\rho_{water}}{2} V^2.$$

8) Calculate the jet head translation $d(t) = \dot{d}(t) \Delta t$.

9) Calculate the jet thickness

$$\delta(t) = \frac{\pi V^2}{8 \dot{d}(t)^2}.$$

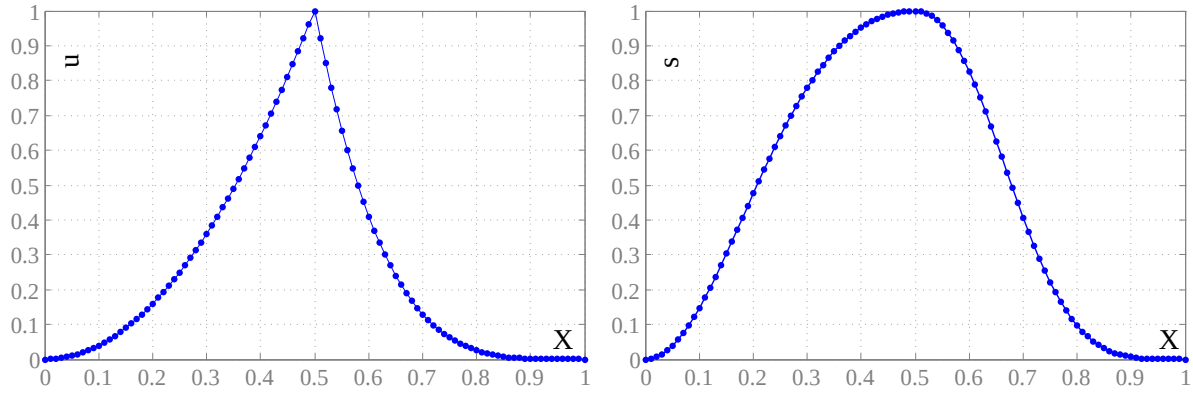

Fig.A2.1 (a) Stretching Parameter u, (b) non-dimensional stretching parameter s.

10) Define the parameter (Fig.A2.1)of the stretching transformation u as follows.

For i = 1 to N/2, u(i) = $\left[\frac{2(i-1)}{N}\right]^2$;

for i = N/2+1, u(N/2+1) = 1;

and for i = N/2+2 to N+1, u(N+2-i) = $\left[\frac{2(i-1)}{N}\right]^4$.

11) Set the non-dimensional parameter

$$s(i) = 1 - \left[\frac{1-u(i)}{1+u(i)}\right]^2.$$

12) Calculate the outer pressure, which is zero beyond the jet head $d(t)$.

$$P_{outer}(i) = \rho_{water}\frac{V\dot{d}(t)\tan^2\beta}{\sqrt{[1-s(i)^2]}}.$$

13) Calculate the common pressure, which is also zero beyond the jet head $d(t)$.

$$P_{common}(i) = \rho_{water}\frac{V\dot{d}(t)\tan^2\beta}{\sqrt{2[1-s(i)]}}.$$

14) Calculate the inner pressure

$$P_{inner}(i) = \rho_{water}\frac{\dot{d}(t)^2}{2}s(i).$$

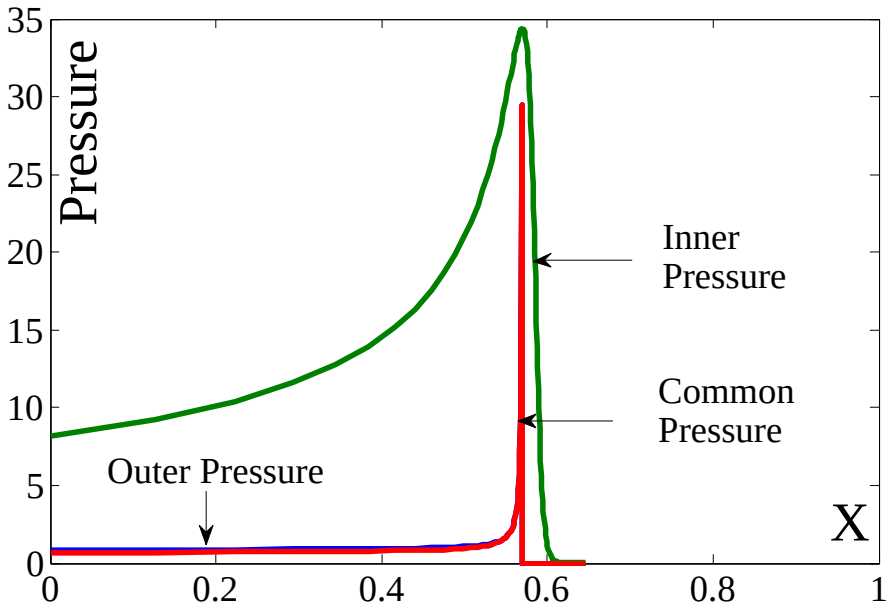

Fig.A2.2 Components of the Impact pressure.

15) Calculate the Total pressure as a superposition of the components (Fig.A2.2)

$$P_{impact} = \frac{P_{outer} + P_{inner} - P_{common}}{\frac{1}{2}\rho_{water} V^2}.$$

The pressure is non-dimensionalized by the stagnation pressure of the vertical impact velocity, i.e. $P_{stagnation}$.

16) Defining the independent variable of the stretching transformation as follows :

(a) For $X < d(t)$, i.e. within the jet head,

$$X(t,i) = d(t) + \frac{\delta(t)}{\pi}\left[2log[u(i)] - \frac{4}{u(i)} - \frac{1}{u^2(i)} + 5\right].$$

(b) At the jet head location, $X(t,i) = d(t) = \frac{Vt\pi}{2\tan\beta}$.

(c) For $X > d(t)$, i.e. beyond jet head

$$X(t,i) = d(t) + \frac{\delta(t)}{\pi}[-2log[u(i)] - 4u(1,i) - u^2(i) + 5].$$

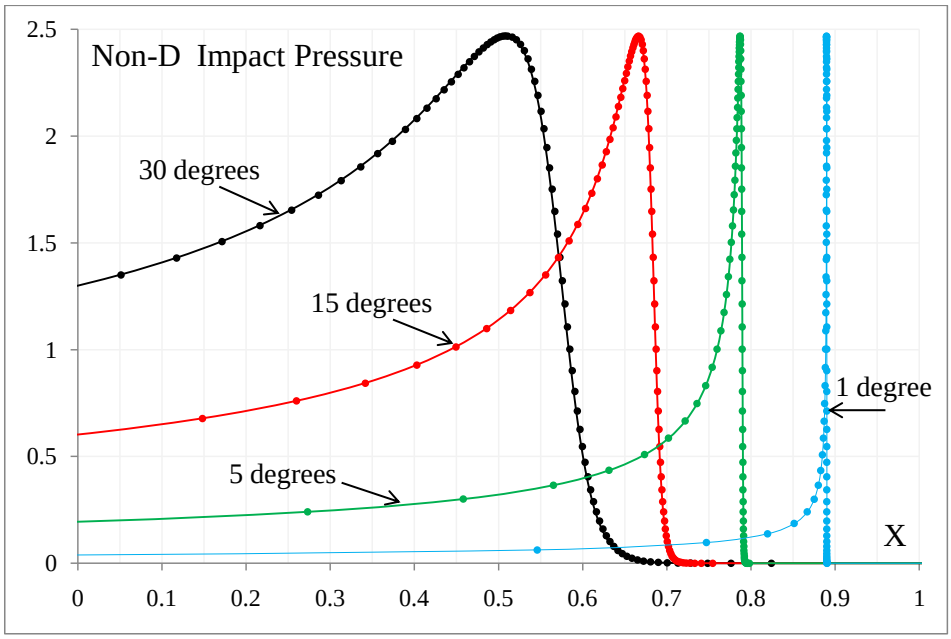

Fig.A2.3 Impact pressure : space discretization.

The Impact pressure $P_{impact}(i)$ is plotted against $\mathrm{X}(t, i)$ as shown in Fig.A2.3. The discretization is very fine near the jet head, which helps define the concentrated impulse configuration. It is affordable to have a coarser discretization away from the jet head, where the pressure configuration becomes more uniform.

APPENDIX 3

Modal Analysis of CCCC plate : Free vibration

Governing differential equation of free vibration of a square plate, with uniform mass and stiffness distributions is :

$$m\frac{\partial Z^2(x,y,t)}{\partial t^2} + \mathbf{c}\frac{\partial Z(x,y,t)}{\partial t} + D\nabla^4 Z(x,y,t) = 0.$$

The independent variables are space (x, y) and time (t). The dependent variable is the dynamic deflection $Z(x, y, t)$. Applying separation of variables : $Z(x, y, t) = G(x, y)F(t)$. Substituting this into the free vibration GDE :

$$mG(x,y)\frac{\partial^2 F}{\partial t^2} + \mathbf{c}G(x,y)\frac{\partial F}{\partial t} + D\nabla^4 G(x,y)F(t) = 0, \quad \text{which gives}$$

$$\frac{\ddot{F}(t)}{F(t)} = \frac{D}{m}\frac{\nabla^4 G(x,y)}{G(x,y)} = -\omega^2; \quad \text{where } -\omega^2 \text{ is the separation constant.}$$

Considering each of the equations separately,

$$\frac{\ddot{F}(t)}{F(t)} = -\omega^2 \text{ gives the principal coordinates, and}$$

$$\frac{D}{m}\frac{\nabla^4 G(x,y)}{G(x,y)} = -\omega^2 \text{ gives the plate modeshape.}$$

But, the fourth-order equation of $G(x, y)$ cannot be factorized into two quadratic equations of $\phi(x)$ and $\phi(y)$. Thus $G(x, y)$ is assumed to be a weighted average of the product of the C-C beam modeshapes along the two directions :

$$G(x,y) = \Sigma_{j=1}^{\infty}\Sigma_{l=1}^{\infty} A_{jl}\phi_j(x)\phi_l(y) = \Sigma_{j=1}^{\infty}\Sigma_{l=1}^{\infty} A_{jl}G_{jl}(x,y).$$

Substituting the above into the previous relation :-

$$\nabla^4[\Sigma_{j=1}^{\infty}\Sigma_{l=1}^{\infty} A_{jl}\phi_j(x)\phi_l(y)] = \frac{m\omega^2}{D}[\Sigma_{j=1}^{\infty}\Sigma_{l=1}^{\infty} A_{jl}\phi_j(x)\phi_l(y)].$$

Expanding the biharmonic operator :

$$\Sigma_{j=1}^{\infty}\Sigma_{l=1}^{\infty}A_{jl}\left[\frac{d^4\phi_j(x)}{dx^4}\phi_l(y)+2\frac{d^2\phi_j(x)}{dx^2}\frac{\phi_l(y)}{dy^2}+d^4\phi_j(x)\frac{\phi_l(y)}{dy^4}-\frac{m\omega^2}{D}\phi_j(x)\phi_l(y)\right]=0.$$

Premultiplying the above system by the Galerkin's premultiplier $H_{rs}=\phi_r(x)\phi_s(y)$ and integrating it over the plate surface area by utilizing the orthogonality of the beam modeshapes gives:-

$\int_0^L\int_0^B\phi_r(x)\phi_s(y)dxdy=1$ for $j=l$; and $\int_0^L\int_0^B\phi_r(x)\phi_s(y)dxdy=0$ for $j\neq l$.

1) *First Term.*

$$\int_0^L\int_0^B\phi_r(x)\phi_s(y)\Sigma_{j=1}^{\infty}\Sigma_{l=1}^{\infty}A_{jl}\left[\frac{d\phi_j(x)}{dx^4}\phi_l(y)\right]dxdy$$
$$=\int_0^L\int_0^B\phi_r(x)\phi_s(y)\Sigma_{j=1}^{\infty}\Sigma_{l=1}^{\infty}A_{jl}\left[\beta_j^4\phi_j(x)\phi_l(y)\right]dxdy$$
$$=\int_0^L\int_0^B\phi_r(x)\phi_s(y)A_{rs}\left[\beta_r^4\phi_r(x)\phi_s(y)\right]dxdy$$
$$=\int_0^L\phi_r(x)\beta_r^4\phi_r(x)dx\int_0^B\phi_s(y)\phi_s(y)dy=A_{rs}\beta_r^4.$$

2) *Second Term.*

$$\int_0^L\int_0^B\phi_r(x)\phi_s(y)\Sigma_{j=1}^{\infty}\Sigma_{l=1}^{\infty}A_{jl}\left[2\frac{d\phi_j(x)}{dx^2}\frac{d\phi_l(y)}{dy^2}\right]dxdy$$
$$=\Sigma_{j=1}^{\infty}\Sigma_{l=1}^{\infty}2A_{jl}\left[\int_0^L\phi_r(x)\frac{d^2\phi_j(x)}{dx^2}dx\right]\left[\int_0^B\phi_s(y)\frac{d^2\phi_l(y)}{dy^2}dy\right]=\Sigma_{j=1}^{\infty}\Sigma_{l=1}^{\infty}2A_{jl}P_{rj}Q_{sl}.$$

Here, $P_{rj}=\int_0^L\phi_r(x)\frac{d\phi_j(x)}{dx^2}dx$ and $Q_{sl}=\int_0^L\phi_s(y)\frac{d\phi_l(y)}{dy^2}dy$.

3) *Third Term.*

$$\int_0^L\int_0^B\phi_r(x)\phi_s(y)\Sigma_{j=1}^{\infty}\Sigma_{l=1}^{\infty}A_{jl}\left[\phi_j(x)\frac{d\phi_l(y)}{dy^4}\right]dxdy$$
$$=\int_0^L\int_0^B\phi_r(x)\phi_s(y)\Sigma_{j=1}^{\infty}\Sigma_{l=1}^{\infty}A_{jl}\left[\phi_j(x)\beta_l^4\phi_l(y)\right]dxdy$$
$$=\int_0^L\int_0^B\phi_r(x)\phi_s(y)A_{rs}\left[\phi_r(x)\beta_s^4\phi_s(y)\right]dxdy$$
$$=\int_0^L\phi_r(x)\phi_r(x)dx\int_0^B\phi_s(y)\beta_s^4\phi_s(y)dy=A_{rs}\beta_s^4.$$

4) *Fourth Term.*

$$\int_0^L \int_0^B \phi_r(x)\phi_s(y)\Sigma_{j=1}^{\infty}\Sigma_{l=1}^{\infty}A_{jl}\left[\phi_j(x)\phi_l(y)\right]dxdy = A_{rs}.$$

Writing in the matrix form

$$\begin{bmatrix} \beta_1^4+\beta_1^4+P_{11}Q_{11} & P_{11}Q_{12} & P_{12}Q_{11} & P_{12}Q_{12} \\ P_{11}Q_{21} & \beta_1^4+\beta_2^4+P_{11}Q_{22} & P_{12}Q_{21} & P_{12}Q_{22} \\ P_{21}Q_{11} & P_{21}Q_{12} & \beta_2^4+\beta_1^4+P_{22}Q_{11} & P_{22}Q_{12} \\ P_{21}Q_{21} & P_{21}Q_{22} & P_{22}Q_{21} & \beta_2^4+\beta_2^4+P_{22}Q_{22} \end{bmatrix} \begin{pmatrix} A_{11} \\ A_{12} \\ A_{21} \\ A_{22} \end{pmatrix} = \begin{pmatrix} 0 \\ 0 \\ 0 \\ 0 \end{pmatrix}$$

The Eigen values of the square matrix gives the square of the non-dimensional natural frequencies of the plate.

$$\begin{vmatrix} \beta_1^4+\beta_1^4+P_{11}Q_{11}-\lambda & P_{11}Q_{12} & P_{12}Q_{11} & P_{12}Q_{12} \\ P_{11}Q_{21} & \beta_1^4+\beta_2^4+P_{11}Q_{22}-\lambda & P_{12}Q_{21} & P_{12}Q_{22} \\ P_{21}Q_{11} & P_{21}Q_{12} & \beta_2^4+\beta_1^4+P_{22}Q_{11}-\lambda & P_{22}Q_{12} \\ P_{21}Q_{21} & P_{21}Q_{22} & P_{22}Q_{21} & \beta_2^4+\beta_2^4+P_{22}Q_{22}-\lambda \end{vmatrix} = 0.$$

Writing in the matrix form :

$$[P_{rj}Q_{sl} - \lambda\delta(r,j;s,l) + \delta(r,j;s,l)\beta_r^4 + \delta(r,j;s,l)\beta_s^4](A_{jl}) = (0),$$

where $\delta(r,j;s,l) = 1$ for $r = j$ and $s = l$; and $\delta(r,j;s,l) = 0$ for $r \neq j$ or $s \neq l$. This frames the Eigen value problem. The Eigen values give the natural frequencies of the CCCC plate, and the Eigenvectors give the plate modeshapes.

For the λ associated with $\beta_j^4 + \beta_l^4 + P_{jj}Q_{ll}$, the nature of the roots depend on the following:

(1) If $j = l$, λ is unique.

(2) If $j \neq l$, and j is odd(even) and l is even(odd), λ's are repeated.

(3) If $j \neq l$, and j and l are both even or both odd, λ's are close but unequal.

APPENDIX 4

Numerical Time Integration

1. Beam vibration.

The system of uncoupled, second-order, ordinary differential equations for the vibration of beams is given as :

$$\frac{d^2q_j(t)}{dt^2} + \left(\frac{2\zeta}{\omega_{1,dry}}\right)\frac{dq_j(t)}{dt} + \left(\frac{\omega_{k,dry}^2}{\omega_{1,dry}^2}\right)q_j(t) = \frac{gf_j(x,t)}{M_{jj}\omega_{1,dry}^2}.$$

Since the equations are uncoupled, the j^{th} modal equation can be solved independent of the other modes, by using numerical time integration schemes.

The *Standard Form* utilizes the following relations : $\dot{q}_j(t) = v_j(t)$; $q_j(t) = u_j(t)$;

Re-writing the equations in the Standard Form, we get two first-order ordinary differential equations.

$$\frac{dv_j(t)}{dt^2} + \left(\frac{2\zeta}{\omega_{1,dry}}\right)\frac{du_j(t)}{dt} + \left(\frac{\omega_{k,dry}^2}{\omega_{1,dry}^2}\right)u_j(t) = \frac{gf_j(x,t)}{M_{jj}\omega_{1,dry}^2}.$$

$$\dot{u}_j(t) = v_j(t);$$

The initial conditions are :

$u_j(t^1) = 0$; and $v_j(t^1) = 0$; i.e. the initial displacement and velocity are zero. Let the time-step be Δt, and let $M_{jj}\omega_{1,dry}^2 = \text{m}$, $\frac{2\zeta}{\omega_{1,dry}^2} = \text{c}$, $\frac{\omega_{k,dry}^2}{\omega_{1,dry}^2} = \text{k}$.

1.1 The Euler's explicit integration scheme is given as:

$$\begin{Bmatrix} \frac{v_j(t^{n+1}) - v_j(t^n)}{\Delta t} \\ \frac{u_j(t^{n+1}) - u_j(t^n)}{\Delta t} \end{Bmatrix} = \begin{bmatrix} -\frac{c}{m} & \frac{-k}{m} \\ 1 & 0 \end{bmatrix} \begin{Bmatrix} v_j(t^n) \\ u_j(t^n) \end{Bmatrix} + \begin{Bmatrix} \frac{gf_j(t^n)}{m} \\ 0 \end{Bmatrix}$$

$$\text{or} \begin{Bmatrix} v_j(t^{n+1}) \\ u_j(t^{n+1}) \end{Bmatrix} = \begin{bmatrix} 1 - \frac{c\Delta t}{m} & \frac{-k\Delta t}{m} \\ \Delta t & 1 \end{bmatrix} \begin{Bmatrix} v_j(t^n) \\ u_j(t^n) \end{Bmatrix} + \begin{Bmatrix} \frac{gf_j(t^n)}{m}\Delta t \\ 0 \end{Bmatrix}$$

This gives the modal displacement and velocity as a function of time.

1.2 The Euler's implicit scheme is given as :

$$\begin{pmatrix} \frac{v_j(t^{n+1})-v_j(t^n)}{\Delta t} \\ \frac{u_j(t^{n+1})-u_j(t^n)}{\Delta t} \end{pmatrix} = \begin{bmatrix} -\frac{c}{m} & \frac{-k}{m} \\ 1 & 0 \end{bmatrix} \begin{Bmatrix} v_j(t^{n+1}) \\ u_j(t^{n+1}) \end{Bmatrix} + \begin{Bmatrix} \frac{gf_j(t^n)}{m} \\ 0 \end{Bmatrix}$$

$$\text{or} \begin{bmatrix} 1+\frac{c\Delta t}{m} & \frac{k\Delta t}{m} \\ -\Delta t & 1 \end{bmatrix} \begin{Bmatrix} v_j(t^{n+1}) \\ u_j(t^{n+1}) \end{Bmatrix} = \begin{bmatrix} 1 & 0 \\ 0 & 1 \end{bmatrix} \begin{Bmatrix} v_j(t^n) \\ u_j(t^n) \end{Bmatrix} + \begin{Bmatrix} \frac{gf_j(t^n)}{m}\Delta t \\ 0 \end{Bmatrix}$$

$$\text{or} \begin{Bmatrix} v_j(t^{n+1}) \\ u_j(t^{n+1}) \end{Bmatrix} = \frac{1}{1+\frac{c\Delta t}{m}+\frac{k\Delta t^2}{m}} \begin{bmatrix} 1 & -\frac{k\Delta t}{m} \\ \Delta t & 1+\frac{c\Delta t}{m} \end{bmatrix} \begin{bmatrix} 1 & 0 \\ 0 & 1 \end{bmatrix} \begin{Bmatrix} v_j(t^n) \\ u_j(t^n) \end{Bmatrix}$$

$$+\frac{1}{1+\frac{c\Delta t}{m}+\frac{k\Delta t^2}{m}} \begin{bmatrix} 1 & -\frac{k\Delta t}{m} \\ \Delta t & 1+\frac{c\Delta t}{m} \end{bmatrix} \begin{Bmatrix} \frac{gf_j(t^n)}{m}\Delta t \\ 0 \end{Bmatrix}$$

This generates the time series of the modal displacement and velocity.

1.3 The Euler's explicit-implicit scheme is given as :

$$\begin{pmatrix} \frac{v_j(t^{n+1})-v_j(t^n)}{\Delta t} \\ \frac{u_j(t^{n+1})-u_j(t^n)}{\Delta t} \end{pmatrix} = \begin{bmatrix} -\frac{c}{m} & \frac{-k}{m} \\ 1 & 0 \end{bmatrix} \begin{Bmatrix} \frac{v_j(t^n)+v_j(t^{n+1})}{2} \\ \frac{u_j(t^n)+u_j(t^{n+1})}{2} \end{Bmatrix} + \begin{pmatrix} \frac{gf_j(t^n)+gf_j(t^{n+1})}{2m} \\ 0 \end{pmatrix}$$

$$\text{or} \begin{bmatrix} 1+\frac{c\Delta t}{2m} & \frac{k\Delta t}{2m} \\ -\Delta t & 2 \end{bmatrix} \begin{Bmatrix} v_j(t^{n+1}) \\ u_j(t^{n+1}) \end{Bmatrix} = \begin{bmatrix} 1-\frac{c\Delta t}{2m} & \frac{-k\Delta t}{2m} \\ \Delta t & 2 \end{bmatrix} \begin{Bmatrix} v_j(t^n) \\ u_j(t^n) \end{Bmatrix} + \begin{Bmatrix} \frac{gf_j(t^n)+gf_j(t^{n+1})}{2m}\Delta t \\ 0 \end{Bmatrix}$$

2. Plate vibration.

The system of second-order, ordinary differential equations for the vibration of plates is given as :

$$\Sigma_{n=1}^{modex*modey} M_{kn} \frac{d^2 q_n(t)}{dt^2} + \Sigma_{n=1}^{modex*modey} C_{kn} \frac{dq_n(t)}{dt} + \Sigma_{n=1}^{modex*modey} K_{kn} q_n(t) = gf_k(t).$$

The Standard Form utilizes the following relations : $\dot{q}_n(t) = v_n(t)$; $q_n(t) = u_n(t)$;

Re-writing the equations in the Standard Form, we get two first-order ordinary differential equations.

$$[M_{kn}]\{\dot{v}_n(t)\} + [C_{kn}]\{\dot{u}_n(t)\} + [K_{kn}]\{u_n(t)\} = \{gf_k(t)\}.$$
$$\dot{u}_n(t) = v_n(t);$$
$$\text{or } \{\dot{v}_n(t)\} + [M_{kn}]^{-1}[C_{kn}]\{\dot{u}_n(t)\} + [M_{kn}]^{-1}[K_{kn}]\{u_n(t)\} = [M_{kn}]^{-1}\{gf_k(t)\}.$$
$$\dot{u}_n(t) = v_n(t);$$
$$\text{or } \{\dot{v}_n(t)\} + [B_{kn}]\{\dot{u}_n(t)\} + [A_{kn}]\{u_n(t)\} = \{F_k(t)\}.$$
$$\dot{u}_n(t) = v_n(t);$$

where $[B_{kn}] = [M_{kn}]^{-1}[C_{kn}]$; $\quad [A_{kn}] = [M_{kn}]^{-1}[K_{kn}]$; $\quad [F_{kn}] = [M_{kn}]^{-1}\{gf_k(t)\}$.

The initial conditions are :
$u_j(t^1) = 0$; and $v_j(t^1) = 0$; i.e. the initial displacement and velocity are zero.

The plate vibration equations are statically coupled. Due to the incorporation of *proportional* damping, the damping matrix is also coupled. Considering the first two modal equations of motion, the Euler's explicit-implicit scheme is used to solve the above system of equations as follows:

$$\begin{bmatrix} 1+B_{11}\Delta t & A_{11}\Delta t & B_{12}\Delta t & A_{12}\Delta t \\ -\Delta t & 2 & 0 & 0 \\ B_{21}\Delta t & A_{21}\Delta t & 1+B_{22}\Delta t & A_{22}\Delta t \\ 0 & 0 & -\Delta t & 2 \end{bmatrix} \begin{Bmatrix} v_1(t^{n+1}) \\ u_1(t^{n+1}) \\ v_2(t^{n+1}) \\ u_2(t^{n+1}) \end{Bmatrix} =$$

$$\begin{bmatrix} 1-B_{11}\Delta t & -A_{11}\Delta t & -B_{12}\Delta t & -A_{12}\Delta t \\ \Delta t & 2 & 0 & 0 \\ -B_{21}\Delta t & -A_{21}\Delta t & 1-B_{22}\Delta t & -A_{22}\Delta t \\ 0 & 0 & \Delta t & 2 \end{bmatrix} \begin{Bmatrix} v_1(t^n) \\ u_1(t^n) \\ v_2(t^n) \\ u_2(t^n) \end{Bmatrix} + \begin{Bmatrix} \frac{F_1(t^n)+F_1(t^{n+1})}{2}\Delta t \\ 0 \\ \frac{F_2(t^n)+F_2(t^{n+1})}{2}\Delta t \\ 0 \end{Bmatrix}.$$

This time-integration gives the modal displacements and velocities.

APPENDIX 5

Code Outputs

The outputs from the MATLAB code are as follows :

1) Natural Frequencies of square plates ω_{dry}.

2) Beam Modeshapes $\phi(x)$.

3) Plate Modeshapes $\Phi(x, y)$.

4) Static Deflection as a function of space and time $Z_{st}(x, y, t)$.

5) Dynamic Deflection as a function of space and time $Z(x, y, t)$.

6) Dynamic Load Factor (DLF).

7) Relative Modal Contribution (RMC).

8) Added mass.

9) DLF at zero wetting time.

10) DLF as a function of space and time.

11) Modal truncation limits for free and forced vibrations.

12) Proportional damping and Modal damping $\mathbf{c}$.

13) Wet natural frequencies ω_{wet}.

APPENDIX 6

Modal Analysis of CCCC plate : Forced vibration

The governing differential equation for the forced, damped vibration of the Kirchhoff's plate is given

$$m\frac{\partial Z^2(x,y,t)}{\partial t^2} + \mathbf{c}\frac{\partial Z(x,y,t)}{\partial t} + D\nabla^4 Z(x,y,t) = F(x,y,t).$$

The total out-of-plane dynamic deflection of the plate is approximately a linear superposition of the modal deflections $Z_k(x,y,t)$, as given as:

$$Z(x,y,t) = \Sigma_{k=1}^{\infty} Z_k(x,y,t) = \Sigma_{k=1}^{\infty} \Phi_k(x,y) q_k(t),$$

with the 3-D plate modeshape (shape function) is defined as a series summation as follows :

$$\Phi_k(x,y) = \Sigma_{j=1}^{modex} \Sigma_{l=1}^{modey} A_{jl}^k \phi_j(x)\phi_l(y) = \Sigma_{j=1}^{modex} \Sigma_{l=1}^{modey} A_{jl}^k G_{jl}(x,y),$$

i.e. $G_{jl}(x,y) = \phi_j(x)\phi_l(y)$, *modex* is the number of modes considered in the x-direction, *modey* is the number of modes considered in the y-direction, and $\phi_j(x)$ and $\phi_l(y)$ are the respective 2-D beam modeshapes (forming an orthogonal set of functions). A_{jl}^k is the amplitude of each $G_{jl}(x,y)$ for the k^{th} natural frequency of vibration. Substituting for the plate modeshape in the GDE :

$$m\Sigma_{k=1}^{\infty}\Phi_k(x,y)\ddot{q}_k(t) + \mathbf{c}\Sigma_{k=1}^{\infty}\Phi_k(x,y)\dot{q}_k(t) + D\nabla^4\Sigma_{k=1}^{\infty}\nabla^4\Phi_k(x,y)q_k(t) = F(x,y,t).$$

Pre-multiplying by the plate modeshape and integrating over the plate surface area :

$$\int_0^L\int_0^B \Phi_p(x,y) m\Sigma_{k=1}^{\infty}\Phi_k(x,y)\ddot{q}_k(t)dxdy + \int_0^L\int_0^B \Phi_p(x,y)\mathbf{c}\Sigma_{k=1}^{\infty}\Phi_k(x,y)\dot{q}_k(t)dxdy$$
$$+ \int_0^L\int_0^B \Phi_p(x,y) D\nabla^4\Sigma_{k=1}^{\infty}\nabla^4\Phi_k(x,y)q_k(t)dxdy = \int_0^L\int_0^B \Phi_p(x,y)F(x,y,t)dxdy.$$

In the matrix form, the system of governing differential equation is:

$$\Sigma_{k=1}^{modex*modey} M_{pk} \frac{d^2 q_k(t)}{dt^2} + \Sigma_{k=1}^{modex*modey} C_{pk} \frac{dq_k(t)}{dt} + \Sigma_{k=1}^{modex*modey} K_{pk} q_k(t) = g f_p(t).$$

where the generalized mass, stiffness and forcing are the following respectively :

$$\begin{aligned} M_{pk} &= m \int_0^L \int_0^B \Phi_p(x,y)\Phi_k(x,y)dxdy \\ &= m \int_0^L \int_0^B [\Sigma_{r=1}^{modex}\Sigma_{s=1}^{modey} A_{rs}^p \phi_r(x)\phi_s(y)][\Sigma_{j=1}^{modex}\Sigma_{l=1}^{modey} A_{jl}^k \phi_j(x)\phi_l(y)]dxdy \\ &= m\Sigma_{r=1}^{modex}\Sigma_{s=1}^{modey}\Sigma_{j=1}^{modex}\Sigma_{l=1}^{modey} A_{jl}^k A_{rs}^p \int_0^L \int_0^B \phi_r(x)\phi_s(y) A_{jl}^k \phi_j(x)\phi_l(y)dxdy \\ &= m\Sigma_{r=1}^{modex}\Sigma_{s=1}^{modey}\Sigma_{j=1}^{modex}\Sigma_{l=1}^{modey} A_{jl}^k A_{rs}^p \int_0^L \phi_r(x)\phi_j(x)dx \int_0^B \phi_s(y)\phi_l(y)dy = m A_{jl}^k A_{rs}^p. \end{aligned}$$

$$\begin{aligned} F_p &= \int_0^L \int_0^B \Phi_p(x,y) f(x,y,t)dxdy = \int_0^L \int_0^B [\Sigma_{r=1}^{modex}\Sigma_{s=1}^{modey} A_{rs}^p \phi_r(x)\phi_s(y)] f(x,y,t)dxdy \\ &= \Sigma_{r=1}^{modex}\Sigma_{s=1}^{modey} A_{rs}^p \int_0^L \phi_r(x) f(x,t)dx \int_0^B \phi_s(y)dy. \end{aligned}$$

$$K_{pk} = D \int_0^L \int_0^B \Phi_p(x,y)\nabla^4\Phi_k(x,y)dxdy = D[K1_{pk} + 2K2_{pk} + K3_{pk}], \qquad \text{where}$$

$$\begin{aligned} K1_{pk} &= D \int_0^L \int_0^B [\Sigma_{r=1}^{modex}\Sigma_{s=1}^{modey} A_{rs}^p \phi_r(x)\phi_s(y)][\Sigma_{j=1}^{modex}\Sigma_{l=1}^{modey} A_{jl}^k \frac{d^4\phi_j(x)}{dx^4}\phi_l(y)]dxdy \\ &= \Sigma_{r=1}^{modex}\Sigma_{s=1}^{modey}\Sigma_{j=1}^{modex}\Sigma_{l=1}^{modey} A_{jl}^k A_{rs}^p \int_0^L \phi_r(x)\beta_j^4\phi_j(x)dx \int_0^B \phi_s(y)\phi_l(y)dy = D\beta_j^4 A_{jl}^k A_{rs}^p, \end{aligned}$$

$$\begin{aligned} K2_{pk} &= \int_0^L \int_0^B [\Sigma_{r=1}^{modex}\Sigma_{s=1}^{modey} A_{rs}^p \phi_r(x)\phi_s(y)][\Sigma_{j=1}^{modex}\Sigma_{l=1}^{modey} A_{jl}^k \frac{d^2\phi_j(x)}{dx^4}\frac{d^2\phi_l(y)}{dy^2}]dxdy. \\ &= \Sigma_{r=1}^{modex}\Sigma_{s=1}^{modey}\Sigma_{j=1}^{modex}\Sigma_{l=1}^{modey} A_{jl}^k A_{rs}^p \int_0^L \phi_r(x)\frac{d^2\phi_j(x)}{dx^2}dx \int_0^B \phi_s(y)\frac{d^2\phi_l(y)}{dy^2}dy, \end{aligned}$$

$$K3_{pk} = D \int_0^L \int_0^B [\Sigma_{r=1}^{modex} \Sigma_{s=1}^{modey} A_{rs}^p \phi_r(x) \phi_s(y)][\Sigma_{j=1}^{modex} \Sigma_{l=1}^{modey} A_{jl}^k \phi_j(x) \frac{d^4 \phi_l(y)}{dy^4}] dx dy$$

$$= \Sigma_{r=1}^{modex} \Sigma_{s=1}^{modey} \Sigma_{j=1}^{modex} \Sigma_{l=1}^{modey} A_{jl}^k A_{rs}^p \int_0^L \phi_r(x) \phi_j(x) dx \int_0^B \beta_l^4 \phi_s(y) \phi_l(y) dy = D A_{jl}^k \beta_l^4 A_{rs}^p.$$

Owing to the orthogonality of the beam modeshapes, the three matrices [M],[K1] and [K3] are diagonal.

APPENDIX 7

Velocity Potential Numerical formulation

Considering a flat surface panel with a constant-strength distribution σ per unit area, bounded by four straight lines, (Katz and Plotkin)[63] the velocity potential at an arbitrary point P*(x,y,0)* is given as follows:

$$\Phi(x,y,0) = \frac{\sigma}{4\pi}[-\frac{(y-y_1)dx}{d_{12}} log\left(\frac{r_1+r_2+d_{12}}{r_1+r_2-d_{12}}\right) + \frac{(x-x_2)dy}{d_{23}} log\left(\frac{r_2+r_3+d_{23}}{r_2+r_3-d_{23}}\right) - \frac{(y-y_3)dx}{d_{34}} log\left(\frac{r_3+r_4+d_{34}}{r_3+r_4-d_{34}}\right) + \frac{(x-x_4)dy}{d_{41}} log\left(\frac{r_4+r_1+d_{41}}{r_4+r_1-d_{41}}\right)]$$

where $r_k = \sqrt{(x-x_k)^2+(y-y_k)^2}$ and $d_{ij} = \sqrt{(x_i-x_j)^2+(y_i-y_j)^2}$.

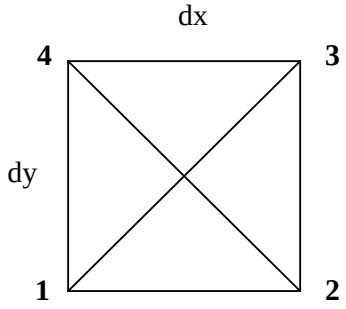

Square Source Panel.

The square source panel is modelled as shown in the figure above. Thus, $d_{12} = dx$, $d_{23} = dy$, $d_{34} = dx$, $d_{41} = dy$. Or,

$$\Phi(x,y,0) = \frac{\sigma}{4\pi}[-(y-y_1) log\left(\frac{r_1+r_2+d_{12}}{r_1+r_2-d_{12}}\right) + (x-x_2) log\left(\frac{r_2+r_3+d_{23}}{r_2+r_3-d_{23}}\right) - (y-y_3) log\left(\frac{r_3+r_4+d_{34}}{r_3+r_4-d_{34}}\right) + (x-x_4) log\left(\frac{r_4+r_1+d_{41}}{r_4+r_1-d_{41}}\right)]$$

Since it is a square panel,

$$dx = dy = a, \quad r_k = \frac{a_k}{\sqrt{2}}, \quad x - x_2 = -\frac{a}{2}, \quad y - y_1 = \frac{a}{2}, \quad x - x_4 = \frac{a}{2}, \quad y - y_3 = -\frac{a}{2}.$$

or

$$\Phi(x, y, 0) = \frac{\sigma}{4\pi}[-\frac{a}{2}log\left(\frac{r_1 + r_2 + d_{12}}{r_1 + r_2 - d_{12}}\right) - \frac{a}{2}log\left(\frac{r_2 + r_3 + d_{23}}{r_2 + r_3 - d_{23}}\right) - \frac{a}{2}log\left(\frac{r_3 + r_4 + d_{34}}{r_3 + r_4 - d_{34}}\right) - \frac{a}{2}log\left(\frac{r_4 + r_1 + d_{41}}{r_4 + r_1 - d_{41}}\right)].$$

Substituting,

$$\left(\frac{r_1 + r_2 + d_{12}}{r_1 + r_2 - d_{12}}\right) = \frac{\frac{a}{\sqrt{2}} + \frac{a}{\sqrt{2}} + a}{\frac{a}{\sqrt{2}} + \frac{a}{\sqrt{2}} - a} = 3 + 2\sqrt{2}.$$

Thus the potential at the collocation point is

$$\Phi(x, y, 0) = \frac{\sigma a}{2\pi} log[3 + 2\sqrt{2}].$$

BIBLIOGRAPHY

Hydroelasticity

[1] Bishop, R.E.D. and Price, W.G., *Hydroelasticity of Ships*, Cambridge University Press, 1979.

[2] Xia, J., Wang, Z., Jensen, J.J., *Non-linear wave loads and ship responses by a time-domain strip theory*, Marine Structures 11(1998) 101-123.

[3] Kyoung, J.H., Hong S.Y., Kim B.W. and Cho S.K., *Hydroelastic response of a very large floating structure over a variable bottom topography*, Ocean Engineering, 32(2005) 2040-2052.

[4] Senjanovic, I., Catipovic, I., Tomasevic, S., *Coupled flexural and torsional vibrations of ship-like traders*, Thin-Walled Structures 45(2007) 1002-1021.

[5] Senjanovic, I., Malenica, S., Tomasevic, S., *Investigation of ship hydroelasticity*, Ocean Engineering (2008) doi:10.1016/j.oceaneng.2007.11.2008.

Slamming and Impact

[6] Cointe, R., *Two-dimensional water-solid impact*, Journal of Offshore Mechanics and Arctic Engineering, May 1989, Vol. 111, Pg 109-114.

[7] Howison, S.D., Ockendon, J.R., and Wilson, S.K., *Incompressible water-entry problems at small deadrise angles*, Journal of Fluid Mechanics, 1991, vol. 222, pp. 215-230.

[8] Henke D. J., *Transient response of plates to travelling loads with application to slamming damage*, International journal of Impact Engineering,Vol.15, No.6, pp. 769-784, 1994.

[9] Faltinsen, O.M., *Water entry of a wedge by a hydroelastic orthotropic plate theory*, Journal of Ship Research, Vol. 43, No.3, 1999, pp. 180-193.

[10] Lu, C.H., He, Y.S., and Xu, G.X., *Coupled analysis of nonlinear interaction between fluid and structure during impact.*, Journal of Fluids and Structures (200) 14,

127-146.

[11] Khabakhpasheva, T.I. and Korobkin, A.A., *Approximate models of elastic wedge impact*, 18th International Workshop on Water Waves and Floating Bodies, Le Croisic, France, 2003.

[12] Peseux B., Gornet L. and Donguy B., *Hydrodynamic impact : numerical and experimental investigations*, Journal of Fluids and Structures, 21 (2005) 277-303.

[13] Korobkin, A., Gueret, R., Malenica, S., *Hydroelastic coupling of beam finite model with Wagner theory of water impact*, Journal of Fluids and Structures 22 (2006) 493-504.

[14] Stenius, I., Rosen, A., and Kuttenkeuler, J., *Explicit FE-modelling of fluid-structure interaction in hull-water impacts*, International Shipbuilding Progress 53 (2006) 103-121.

[15] Kim, D.J., Vorus, W., Troesch, A., and Golliwitzer, R., *Coupled hydrodynamic impact and elastic response*, 21^{st} Symposium on Naval Hydrodynamics, 2007.

[16] Constantinescu, A., Fuiorea, I., Neme, A., Bertram, V., and Salas, M., *Hydroelastic numeric analysis of a wedge-shaped shell structure impacting a water surface.*, Latin American Applied Research, 38:35-43(2008).

Moving Loads

[17] Thomson, W.T., *Theory of Vibration with applications*, 3^{rd} edition, Printice Hall, 1988.

[18] Law, S.S. and Chan, T.H.T., *Moving force identification : a time domain method*, Journal of Sound and Vibration, (1997) 201(1), 1-22.

[19] Lee, H.P., *Transverse vibration of a Timoshenko beam acted on by an accelerating mass*, Applied Acoustics, Vol.47, No.4, pp.319-330, 1996.

[20] Yau, J.D., Wu, Y.S. and Yang, Y.B., *Impact response of bridges with elastic bearings to moving loads*, Journal of Sound and Vibration, (2001), 248(1), 9-30.

[21] Savin, E., *Dynamic amplification factor and response spectrum for the evaluation of vibrations of beams under successive moving loads*, Journal of Sound and Vibration,

(2001) 248(2), 267-288.

[22] Dugush, Y.A. and Eisenberger, M., *Vibrations of non-uniform continuous beams under moving loads*, Journal of Sound and Vibration, (2002) 254(5), 911-926.

[23] Yu, L. and Chan, T.H.T., *Moving force identification based on the frequency-time domain method*, Journal of Sound and Vibration, 261 (2003) 329-349.

[24] Pesterev A.V. et al, *Revisiting the moving force problem*, Journal of sound and vibration, 261 (2003) 75-91.

[25] Yagiz, N. and Sakman, L.E., *Vibrations of a rectangular bridge as an isotropic plate under a travelling full vehicle model*, Journal of Vibration and Control, 12(1): 83-98, 2006.

Beam Vibration

[26] Yamaki, N. and Mori, A., *Non-linear vibrations of a clamped beam with initial deflection and initial axial displacement, Part 1 : theory*, Journal of Sound and Vibration, (1980), 71(3), 333-346.

[27] Ward, L.W., *Sailboat Bow Impact Stresses*, 7^{th} Chesapeake Sailing Yacht Symposium 1985, Annapolis, MD. pp. 13-20.

[28] Pan, X. and Hansen, C.H., *Effect of end conditions on the active control of beam vibration*, Journal of Sound and Vibration, (1993), 168(3), 429-448.

[29] Howard, C.Q., *Modal mass of clamped beams and clamped plates*, Journal of Sound and Vibration 301 (2007) 410-414.

[30] Wang, B.T., and Cheng, D.K., *Modal analysis of MDOF system by using free vibration response data only*, Journal of Sound and Vibration (2007), doi:10.1016/j.jsv.2007.09.030.

Structural Damping

[31] Wilson, J.M. and Man, L., *A simplified approach to calculate the damping ratio matrix for multiple degree of freedom vibration systems*, Communications in Applied Numerical Methods, Vol.6, 633-638 (1990).

[32] Man, L. and Wilson, J.M., *On the damping ratio of multi-degree-of-freedom systems*,Communications in Applied Numerical Methods,Vol.8, 265-271 (1992).

[33] Bulatovic, R.M., *On the critical damping in multi-degree-of-freedom systems*, Mechanics Research Communications 29 (2002) 315-319.

[34] Mahmoodi, S.N., Khadem, S.E. and Rezaee M., *Analysis of non-linear modeshapes and natural frequencies of continuous damped systems*, Journal of Sound and Vibration, 275 (2004) 283-298.

Plate Vibration

[35] Young, D., *Vibration of Rectangular plates by the Ritz method*, Annual conference of the Applied Mechanics Division, Purdue University, Lafayette, Indiana, June 22-24, 1950.

[36] Leissa, A.W., *Vibration of plates*, for the Acoustical Society of America through the American Institute of Physics, 1993.

[37] Saha, K.N., Misra, D., Pohit, G., and Ghosal, S., *Large Amplitude free vibration study of square plates under different boundary conditions through a static analysis*, Journal of Vibration and Control, 10: 1009-1028, 2004.

[38] Wang, G., Wereley, N.M., and Chang, D.C., *Analysis of Bending Vibration of rectangular plates using two-dimensional plate modes*, Journal of Aircraft, Vol.42, No.2, March-April 2005.

[39] Saha, K.N., Misra, D., Ghosal, S., and Pohit, G., *Nonlinear free vibration analysis of square plates with various boundary conditions*, Journal of Sound and Vibration 287 (2005) 1031-1044.

[40] Zhang, W., Wang, A., Vlahopoulos, N., and Wu, K., *A vibration analysis of stiffened plates under heavy fluid loading by an energy finite element analysis formulation*, Finite Elements in Analysis and Design 41 (2005) 1056-1078.

[41] Yeh, Y.L., Jang, M.J., and Wang, C.C., *Analyzing the free vibrations of a plate using finite difference and differential transformation method*, Applied mathematics and

computation, 178(2006)493-501.

[42] Korobkin, A.A., Khabakhpasheva, T.I. and Wu, G.X., *Coupled hydrodynamic and structural analysis of compressible jet impact onto elastic panels*, Journal of fluids and structures, 24 (2008) 1021-1041.

[43] Yu, S.N., Xiang, Y. and Wei, G.W., *Matched interface and boundary (MIB) method for the vibration analysis of plates*, Communications in Numerical Methods in Engineering (2008), DOI: 10.1002/cnm.1130.

[44] Chen, C.P., Huang, C.H. and Chen, Y.Y., *Vibration analysis and measurement for piezoceramic rectangular plates in resonance*, Journal of Sound and Vibration (2009), doi:10.1016/j.jsv.2009.04.025.

Fluid-Structure Interaction

[45] Lamb H., *On the vibrations of an elastic plate in contact with water*, Proceedings of the Royal Society of London, Series A, Vol.98, No.690, (1920), pp.205-216.

[46] Chertock, G., *The flexural response of a submerged solid to a pulsating gas bubble*, Journal of Applied Physics, Vol. 24, No.2, 192-197, 1953.

[47] Meyerhoff, W.K., *Added masses of thin rectangular plates calculated from potential theory*, Journal of Ship Research, 1970.

[48] Purcell, E.S, Allen, S.J. and Walker, R.T., *Structural analysis of the U.S. Coast Guard Island class patrol boat*, SNAME transactions, Vol.96, 1988, pp. 221-246.

[49] Joseph, P., Muthuveerappan, G., and Ganeshan, N., *Vibrations of generally orthotropic plates in fluids*, Composite Structures 15 (1990) 25-42.

[50] Wu, C., Watanabe, E., and Utsunomiya, T., *An Eigen function expansion-matching method for analyzing the wave-induced responses of an elastic floating plate*, Applied Ocean Research, 17 (1995) 301-310.

[51] Kwak, M.K., *Hydroelastic vibration of rectangular plates*, Transactions of the ASME, Vol.63, pp. 110-115, 1996.

[52] Faltinsen, O.M., *The effect of hydroelasticity on ship slamming*, Philosophical transactions of the Royal Society, London, (1997), 355, 575-591.

[53] Chang, T.P. and Liu, M.F., *On the frequency of a rectangular isotropic plate in contact with fluid*, Journal of Sound and Vibration, (2000), 236(3), 547-553.

[54] Cheung,Y.K. and Zhou, D., *Coupled Vibratory characteristics of a rectangular container bottom plate*, Journal of Fluids and Structures (2000) 14, 339-357.

[55] Yadykin, Y., Tenetov, V., and Levin, D., *The added mass of a flexible plate oscillating in a fluid*, Journal of Fluids and Structures, 17 (2000) 115-123.

[56] Hashemi, S.H., Karimi, M., Taher, H.R.D., *Vibration analysis of rectangular Mindlin plates on elastic foundations and vertically in contact with stationary fluid by the Ritz method*, Ocean Engineering 37 (2010) 174-185.

Aspect Ratio

[57] Liew, K.M., Lam, K.Y., and Chow, S.T., *Free vibration analysis of rectangular plates using orthogonal plate function*, Computers and Structures, Vol.34, No.1, pp. 79-85, 1990.

[58] Harik, I.E., Liu, X., and Balakrishnan, N., *Analytic solution to free vibration of rectangular plates*, Journal of Sound and Vibration (1992) 153(1), 51-62.

[59] Sakata, T., Takahashi, K., and Bhat, R.B., *Natural frequencies of orthotropic rectangular plates obtained by iterative plates obtained by iterative reduction of the partial differential equation*, Journal of Sound and Vibration (1996) 189(1), 89-101.

[60] Low, K.H., Chai, G.B., Lim, T.M., and Sue, S.C., *Comparisons of experimental and theoretical frequencies for rectangular plates with various boundary conditions and added mass*, International Journal of Mechanical Sciences, Vol.40, No.11, pp. 1119-1131, 1998.

[61] Zhu, X.Q. and Law, S.S., *Dynamic Behavior of orthotropic rectangular plates under moving loads*, Journal of Engineering Mechanics, Vol. 129, No.1, pp. 79-87, 2003.

[62] Huang, M., Ma, X.Q., Sakiyama, T., Matsuda, H., and Morita, C., *Free vibration*

analysis of continuous rectangular plates, Journal of Sound and Vibration, 329 (2010) 485-496.

Books

[63] Shames, I.H. and Dym, C.L., *Energy and finite element methods in structural mechanics*, SI units edition, Taylor and Francis, 1991.

[64] Katz, J. and Plotkin, A., *Low-Speed Aerodynamics*, Tata-McGraw Hill, Inc., 1991.

Self publications

[65] Datta, N., Kim D. and Troesch, A.W., *Hydrodynamic impact-induced vibration characteristics of a uniform Euler-Bernoulli beam*, International Symposium on Vibro-impact Dynamics of Ocean systems and related problems, Troy, Michigan, Oct 2008.

[66] Datta, N. and Troesch, A.W., *Slam-induced vibration characteristics of a Kirchhoff's plate*, Proceedings of the 10th International Conference on fast Sea transportation, Athena, Greece, Oct 2009.

[67] Datta, N. and Troesch, A.W.,*Dynamic response of Kirchhoff's plates to transient impact loads*, Submitted to the Ocean Engineering Journal, April 2010.

[68] Datta, N. and Troesch, A.W.,*Hydroelastic vibration of rectangular due to hydrodynamic impact loads*, Submitted to the Ocean Engineering, October 2010.

Reference

[69] Kunow-Baumhauer, *Response of a plate to a transient pressure wave load*, Journal of Sound and Vibration, (1984) 92(4), 507-515.

[70] Goncalves P.J.P., Brennan M.J. and Elliott S.J., *Numerical evaluation of high-order modes of vibration in uniform Euler-Bernoulli beams, Journal of Sound and Vibration*, 301(2007) 1035-1039.